UNIVERSITAT ROVIRA I VIRGILI

Electrical Properties and Surface Characterization of Thin Copper Films Subjected to Mechanical Vibrations

Sufyan Azam

UNIVERSITAT ROVIRA i VIRGILI

Electrical Properties and Surface Characterization of Thin Copper Films Subjected to Mechanical Vibrations

_____

SUFYAN AZAM

DOCTORAL THESIS
2020

Sufyan Azam

Electrical Properties and Surface Characterization of Thin Copper Films Subjected to Mechanical Vibrations

DOCTORAL THESIS

Supervised By: Dr. Alex FRAGOSO

Departament d'Enginyeria Química

UNIVERSITAT ROVIRA i VIRGILI

Tarragona

November 11, 2020

This page intentionally left blank

Departament d'Enginyeria Quimica
Universitat Rovira i Virgili
Campus Sescelades,
Avda. Països Catalans, 26
43007 Tarragona
Tel: 977 55 85 79
Fax: 977 55 96 67

Dr. Alex Fragoso

CERTIFIES:

That the present study, entitled "ELECTRICAL PROPERTIES AND SURFACE CHARACTERIZATION OF THIN COPPER FILMS SUBJECTED TO MECHANICAL VIBRATIONS" presented by **Sufyan Azam** for the award of the degree of Doctor, has been carried out under my supervision at the Department of Chemical Engineering of Universitat Rovira i Virgili and it fulfills the requirements to receive the International mention.

Tarragona, November 11th 2020.

Dr. Alex Fragoso

Acknowledgments

All Praise to ALLAH S.W.T the Almighty, for giving me the blessing, the strength, the chance and endurance to complete this study. It is difficult to overstate my gratitude to my supervisor Dr. Alex *Fragoso* whose help, stimulating suggestions and understanding helped me in all the time of my research and writing of this thesis. I could not have finished this study without his full support.

I would like to extend my deepest appreciation to all the staff in Department of Mechanical Engineering, Umm Al − Qura University, for providing me labs access to conduct my experiments, all my colleagues especially Dr. Korrany Hassan, Dr. Shadi Munshi, and Dr. Badr for their kind support and help on the technical and the administrative aspect of the study.

Nobody has been more important to me in the pursuit of this work than the members of my family. I would like to thank my parents, whose love and guidance are with me in whatever I pursue. They are the ultimate role models. Most importantly, I wish to thank my loving and supportive wife and my two wonderful children, Ali and Hassan, who provide unending motivation.

Contents

Abbreviations and Symbols

MEMS	Micro-Electro-Mechanical Systems
PCB	Printed Circuit Board
MPa	Mega-Pascal
μ**m**	Micro-meter
nm	Nano-meter
FR4	Flame Retardant Glass Fiber Epoxy Laminate
FRP	Fiber Reinforced Polymer
PMCs	Polymer Matrix Composites
OMCs	Organic Matrix Composites
MMCs	Metal Matrix Composites
CMCs	Ceramic Matrix Composites
PMCs	Polymer Matrix Composites
IMCs	Inter-metallic Matrix Composites
EMA	Experimental Modal Analysis
FRFs	Frequency Response Functions
SISO	Single-Input, Single-Output
SIMO	Single-Input, Multi-Output
MIMO	Multi-Input, Multi-Output
$\mathbf{f_t}$	Input Force
FFT	Fast Fourier Transform
SDOF	Single Degree of Freedom
$\zeta_\mathbf{r}$	Damping Ratio
$\omega_\mathbf{r}$	Resonance Frequency
$\mathbf{\Delta}\omega$	Frequency Bandwidth
$\mathbf{R_{sh}}$	Sheet Resistance
t	Film Thickness
σ	Electrical Conductivity

C	Correction Factor
ρ	Bulk Resistivity
LIGA	Lithographie, Galvanoformung, Abformung
f$_n$	Natural Frequency
K	Modal Constant
EI	Composite Beam Stiffness Factor
g	Acceleration of Gravity
w	Linear Mass Density
D	Plate Stiffness Factor
E	Young Modulus
GPa	Giga-Pascal
FEM	Finite Element Method
CMPs	Correlated Mode Pairs
SMU	Source Measure Unit
GUI	Graphical User Interface
NFD	Natural Frequency Difference

Abstract

Printed Circuit Boards (PCBs) and Micro-Electrical Mechanical Systems (MEMS) have a great interest in electrical, electronic and mechanical instruments. (PCBs) consist mainly of thin copper films embedded to composite or metallic substrates. During the function, many mechanical, vibration and thermal loadings arise due to electrical current fluctuations. There are many other important parameters which are crucial for the performance and reliability of these devices. These parameters e.g., stress amplitude, mean stress, downsizing film dimension and crack initiation and propagation still, need more study and investigations. The present research comprises of two phases. During the first phase of this study, the vibration characteristics of these materials were studied in details. The cantilever samples made of bare copper bounded to FR4 have been studied to analyze, for the first time, the vibration behavior of specimens with different aspect ratios, with and without central holes of different diameters. Natural frequencies and damping ratios were determined experimentally and analytically using a finite element method for four groups of samples with a very good correspondence between both methods. The fundamental resonance frequency of all the specimens was found to be less than 40 Hz and the influence of a central hole was not significant to affect the modal properties. In the second phase of this research, the development of cracks due to mechanical vibrations (mechanical property) and other size parameters in PCBs were studied to create a better link to the damage mechanisms of these materials and to identify the crucial parameters that control material's sensitivity to mechanical and thermal loads with respect to their effect on electrical performance. Experimentally, empirical schemes were used, where the electrical properties were mapped with respect to vibration damage and processing parameters. The thermal variations showed a very little effect on electrical parameters but on the other hand the values showed a considerable change due to mechanical loadings. Before cyclic loading at 25^0C, sheet resistance values for zones A, B and C were 1.34, 1.33 and

1.33 ($m\Omega/sq$) respectively. The same sample when subjected to 800k cycles, the sheet resistance values at 25^0C for the zones A, B and C were 1.34, 1.33 and 24.19 ($m\Omega/sq$) respectively. This behavior was not observed in case of thermal loadings where 20^0C rise in temperature gave only 1 % rise in sheet resistance values. The ESEM images after 200k and 800k vibration cycles, showed the developed cracks on the sample surfaces. These cracks were the result of the plastic deformation undergone by the samples after vibration stresses. The density of cracks was increased with the number of cycles from $\sim$3 cracks per mm at 200k cycles to $\sim$8 cracks per mm at 800k cycles, indicating a dependence of the overall damage with the number of cycles. The cracks were found to be $\sim$1 µm in width and several millimeters long. The surface composition analysis indicated that the vibration stress only produced physical damage and not chemical processes such as oxidation. The samples were also analyzed using water droplet contact angle. The observed angles for untreated samples ranged from 78 to 95 degrees and after mechanical vibration damage, the contact angle increased to 117−119 degrees.

This work focused on methods to characterize electrical and mechanical behavior to better understand the relation between damage accumulation and electrical performance of PCB boards to improve their reliability during function.

Introduction

Rapid advances in microelectronics and micro-electro-mechanical systems (MEMS) technologies, lead to the development of various MEMS devices so it has become important to ensure their performance and reliability. The mechanical properties of thin films are widely used in printed circuit boards (PCBs) and MEMS devices for the evaluation of performance and reliability of the MEMS devices because mechanical properties of thin films vary from those of bulk materials. During operation, the fatigue damage causes due to high cyclic mechanical vibrations; therefore, it is important to investigate vibration fatigue damage (mechanical property) and its effect on electrical resistance (functional property) of these films with and without thermal loading. Recent research concerns on studying this effect. A model specimen of copper thin film bonded on stainless steel base has been tested under cyclic loading. Stress amplitude of 140 MPa has been applied on films of small dimensions (Widths and thickness down to 15 mm and 50 μm respectively). Axial strain amplitude has been measured and shows a constant trend for all specimens. Electrical resistivity changes during fatigue have been measured by using four-point-probe method and correlated with fatigue damage. The caused cracks by fatigue were observed along both surface and thickness of the film. Results show the increase of electrical resistivity with increase of loading cycles. Less multiple fatigue cracks occurs for smaller films, furthermore some cracks were caused through film thickness, so that there was a significant increase of electric resistance. In case of smaller film thickness, the crack initiation and propagation decrease with decreasing film width although strain amplitude is constant. Moreover, this behavior was agreed with the electrical resistivity change.

There are many other important parameters which are crucial for the performance and reliability of printed circuit boards (PCBs) and MEMS devices. These parameters e.g., stress amplitude, mean stress, downsizing film dimension and crack

initiation and propagation still, need more study and investigations. The Proposed research will concern on the development of high cycle vibrations and other size parameters in PCBs and MEMS devices in applications. The purpose of this research is, to create a better link to the damage mechanisms of this material itself and to identify the crucial parameters that control material's sensitivity to high frequency vibrations with respect to their effect on electrical performance with and without thermal variations. Experimental schemes will be used, where the electrical properties will be mapped with respect to the damage behavior and processing parameters. This work will focus on methods to characterize the sheet resistivity behavior under cyclic vibrations. To this end, a better understanding of the relation between damage accumulation and electrical performance of printed circuit boards (PCBs) and MEMS devices is necessary and will lead to the improvement in fabrication of these devices.

Chapter 1

Literature review

Smart electronic devices used over the years mostly consist of printed circuit boards (PCBs) and micro-electromechanical systems (MEMS). These boards are mainly made of thin copper films bounded to fiber epoxy laminates, such as FR4. PCB board sizes can vary from about 2 cm to 50 cm and most commonly have a rectangular shape in the electronic industry [01]. When attached to a machine structure, circuit boards can undergo various vibrating forces. Statistics show that about 20 % of airborne electronic equipment failures occur due to vibration factors [02]. Damage, or even total failure, can occur when shock and vibration produce high stress on substrate, components, and joints. The type of damage is dependent on the frequency and amplitude of bending moments and inertial loads imposed on the PCB structure [03]. Since the dynamic loading is very critical for electronic equipment, studies to analyze and isolate vibrations in these systems are very important. However, market pressure and shortened development stages have rendered reliability analysis gradually unaffordable and, hence, simulations based on failure physics have been proposed to test the reliability of circuit boards [04].

Modal analysis is the study of the dynamic characteristics of a system by evaluating natural frequencies and damping factors, among other dynamic parameters. This analysis is used to formulate a mathematical model that explains the dynamic behavior of the studied system and is an important tool to optimize the dynamic characteristics of structures and materials [05]. In the case of PCB boards and integrated circuits, their reliability depends, among other factors, on the possibility to endure vibration loads and impacts that can affect their performance. Modal analysis can thus be a very useful tool for engineers to reveal vulnerable areas and

avoid premature failure [06–08].

Different studies have addressed the problem of determining the dynamic properties of PCB boards, using either experimental or analytical methods. In an early work, Cifuentes [09] determined the factors that play a critical role in the dynamic behavior of a PCB having three components of similar mass density. This author found that the first vibration mode should account for more than 90 % of the mass of the structure and minor rearrangements of the components on the board cause major re-distributions of the dynamic response towards higher modes. Aytekin and Ozguven [10] suggested an analytical model of a simply supported PCB with a component and studied the vibrating responses of the critical elements on a PCB for different design alternates. They found that a two-degree-of-freedom spring mass model can accurate predict the response to a random vibration profile and could be used in preliminary design stages. Ren et al. [11] performed modal analysis on a PCB, by the finite element method and successfully predicted the changes in natural frequencies associated to changing the board thicknesses. Nilesh et al. [12] determined the mechanical properties of a multi-layered PCB and validated their results using Ansys® and Sherlock® (Canonsburg, PA, USA; Gwynedd, PA, USA) computer software. They observed frequency changes by changing material properties such as the out-of-plane modulus (Ez), Poissonś ratio, and shear modulus.

On the other hand, Veilleux [13] described various methods for reducing the destructive resonant amplitude of PCBs in electronic systems. He compared the effectiveness of isolation, extensional damping, and shear damping techniques with a standard printed circuit board. Veprik [14] solved vibration isolation problems in electronic boxes, by using a two-degree-of-freedom mass, spring, and damper system in order to minimize the dynamic response of internal sensitive components of the electronic platform. Recently, Prashant [15] has introduced the presence of connector, tray, and ribs as a boundary condition in a finite element model of a PCB. It was found that the presence of these elements should not be neglected when studying the vibration modes and the developed analysis can help in identifying optimal connector location in the design of PCB platforms. Other studies have addressed the presence of holes in different positions of the board that can affect the dynamic properties of the PCB [16, 17]. Glass fiber reinforced epoxy resin (referred to commercially as

FR4) is the most common board material used in computers and communication equipment [18]. Studies on the mechanical properties of this composite material are thus of important, in order to estimate the reliability of FR4 based PCBs. We have recently studied the essential work of fracture on copper/FR4 specimens of different sizes using a double edge notched test with and without open holes of different diameters [19]. The tested composites behaved as quasi-brittle hybrid materials due to the anisotropy of the FR4 support that is in part compensated by the isotropic copper layer. Hence, a hole size effect was found to decrease the strength by up to 15 % for smaller size specimens. Recent study shows that thin films, having major rule in PCBs and MEMS devices for the evaluation of performance and stability of these devices, consist of different mechanical properties as compared to bulk materials (Hong and Weil 1996, Read 1998, Schwaiger and Kraft 1999, 2003, Kraft et al. 2001, 2002, Thiele et al. 2002) [20]. Because of the use of thin C_u films in advanced MEMS devices, a thorough Investigation of fatigue damage (mechanical property) and its effect on electrical resistance (functional property) needs more research.

The research on micro scaled metal films shows that an elastic substrate also contributes in fatigue damage of these films. The forming of cracks is related to an obvious stiffness decrease in composite made of film and base material [20]. Experimental studies show that the formation of dislocation structures and type of extrusions (fine or coarse) depends upon grain size of thin metal films. A geometric or micro-structural thickness of 3 μm is the minimum grain size required for the forming of bulk-like fatigue damage in C_u thin films [21]. Because of the use of thin C_u films in MEMS and other devices, the thermal fatigue also has importance in the proper investigation of their characteristics. [Moenig, Keller and Volkert, 2004] studied thin C_u films behavior as a result of thermal fatigue damage on these films. However, there are two major limitations in this work. First is the independent variation of the strain and the temperature and the second major limitation is the measurement of stresses during testing. This is a crucial issue because, under fatigue tests, most metals experience cyclic hardening or softening. Thus, during experiments performed in strain control conditions, the stresses may vary from the beginning to the end. It limits the utility of stress strain curves determined by wafer-curves [22]. [Zhang, 2005, 2006, 2007] did a comparison between the fatigue damage in 200 nm C_u films and the damage in 3 μm C_u films [21]. The 200 nm thin C_u films, after fatigue tests, demonstrate only a few but small extrusions and extended cracking along twin and grain boundaries. However, 3 μm C_u films show a different

behavior [23–25]. [Sun, 2008] analyzed the effect of fatigue damage behavior and fatigue life of 50 nm to 3 µm thin C_u films. The study of downsizing film thickness shows that the amount and size of extrusions increase with film thickness [26, 27]. [Lee, 2012] investigated the behavior of the fatigue of an electro-deposited thin copper film under a variable amplitude loading. Although this study provides worthy information on fatigue behavior under variable loading, yet it is not sufficient for making any rule or method applicable to more general variable loading. Comprehensive and methodical studies are still needed for this purpose [28]. [Kim, 2013] studied the fatigue damage behavior of pure C_u films having thicknesses between 200 nm and 3 µm. This study gives a good understanding of the voiding process relating to the elimination of dislocation dipoles, yet more extensive study for nano-sized films is needed. The 400 nm films give a more homogeneous dislocation distribution rather than forming heterogeneous dislocation structures [29]. [Kraft, 2013] investigated the bending fatigue of C_u electrodes on flexible substrates. During bending, there is a clear relationship between the degradation of the resistivity of C_u films and the fatigue damage growth in the area subjected to repeated bending and unbending. The results obtained from this study may be referenced to design stable metal electrodes [30]. [Walter, 2015] investigated the thin C_u film properties under High Cycle Fatigue on silicon base and free-standing C_u bars having the same micro-structure. The experimental results show that the damage response of the C_u film depends upon film thickness, the grain size, plane orientation, and the substrate [31–41]. [Zhao, 2016] studied the fatigue and failure mechanism of basalt FRP composites under long-term cyclic loads. It can be noticed that the different fatigue stress levels produced different damage patterns. A fiber fracture normally occurred at the high-stress level and static loading, while at the low and medium stress levels, matrix cracking and interface de-bonding are main damage patterns for BFRP respectively [42].

Progress in the field of materials science and technology especially composite material after meeting the challenges of aerospace industries have cascaded down for domestic and industrial applications, therefore this field is considered one of the most advanced and adaptable engineering materials. Composite materials, the wonder materials are replacing conventional materials like metals, wood etc., because of their superior properties, such as lightweight, high strength-to-weight ratio, stiffness properties and minimum thermal expansion. A numerous experimental and modeling efforts in the literature have been devoted to, understanding the effect of fatigue

damage on reducing the size of thin C_u films under fatigue loads. The proposed research studies the vibration characteristics of thin C_u films, 18 μm, bounded to FR4 epoxy laminate and the damage caused due to the mechanical vibrations, and its effect on electrical resistance (functional property), with and without temperature, of thin C_u films used in MEMS and other devices.

This chapter consists of the following sections: The first section aimed at reviewing of composite materials and their main classifications; the materials of choice for many bulk micro-machined Micro-Electro-Mechanical Systems (MEMS) and Printed Circuit Boards (PCBs). In order to introduce this work, a review of the most relevant composite structure materials and its application are presented in this section. The second section deals with the vibration characteristics of PCBs evaluated by modal analysis. This section talks in general about modal analysis technique to determine vibration properties of a structure under test. The next section provides an introduction to sheet resistance and measurement methods to determine sheet resistance of thin conductive and semiconducting films, the last section of this chapter gives a brief introduction to MEMS, fabrication methods, and their applications.

1.1   An overview of composite materials

Composite materials are multiphase materials obtained by a macroscopic combination of two or more distinct materials, having a recognizable interface between them, in order to attain properties better than those of the individual components used alone do. In contrast to metallic alloys, each material retains its separate chemical, physical and mechanical properties [43]. Basically a composite can be defined as a material obtained by the combination of two or more components that differ in form or composition on a macroscopic scale and are characterized by complementary properties. The main difference with a traditional alloy is that in case of composites each constituent does not dissolve or merge completely into another phase, retaining its identity and resulting in a material characterized by better properties than the ones of the single components considered separately.

Strictly speaking, the idea of composite materials is not a new or recent one. Nature is full of examples wherein the idea of composite materials is used. The coconut palm leaf, for example, is nothing but a cantilever using the concept of fiber reinforcement.

Wood is a fibrous composite; cellulose fibers in a lignin matrix. The cellulose fibers have high tensile strength but are very flexible (i.e. low stiffness), while the lignin matrix joins the fibers and furnishes the stiffness. Bone is yet another example of a natural composite that supports the weight of various members of the body. It consists of short and soft collagen fibers embedded in a mineral matrix called apatite. It would not be too much off the mark to say that a concerted research and development effort in composite materials began in 1965. Since the early 1960s, there has been an increasing demand for materials that are stiffer and stronger yet lighter in fields as diverse as aerospace, energy and civil constructions.

Modern composite materials are usually optimized to achieve a particular balance of properties for a given range of applications as in airplanes. Composites typically have a fiber or particle phase that is stiffer and stronger than the continuous matrix phase [44]. Many types of reinforcements also often have good thermal and electrical conductivity, a Coefficient of Thermal Expansion (CTE) that is less than the matrix, and/or good wear resistance [44]. There are, however, exceptions that may still be considered composites, such as rubber-modified polymers, where the discontinuous phase is more compliant and more ductile than the polymer, resulting in improved toughness. Similarly, steel wires have been used to reinforce gray cast iron in truck and trailer brake drums.

1.2   Classification of Composite Materials

Composite materials can be classified in two different ways. The first level of classification is usually made based on the type and the geometry of the reinforcement which is responsible for the mechanical properties and high performance of the composites. A typical classification is presented in three main types of composite materials: particle-reinforced, fiber-reinforced, and structural composites as shown in Figure 1.1. In particle-reinforced composites, particle dimensions are approximately the same in all directions and generally particulate phase is harder and stiffer than the matrix. In fiber-reinforced composites, the dispersed phase has the geometry of a fiber, the mechanical properties mostly depend on the properties of the fibers and applied load is transmitted to the fibers by the matrix phase through the fiber/matrix interface. Structural composites are the combinations of composites and homogeneous materials and the geometrical design of the structural elements

affect the mechanical properties of the structure. The most common structural composites are laminated composites and sandwich panels [45].

Figure 1.1: Types of the structural composites. [46]

1.2.1   Fiber Reinforced Polymers (FRP'S)

Fiber Reinforced Polymer (FRP) composites are the combination of polymeric resins, acting as matrices or binders, with strong and stiff fiber assemblies which act as the reinforcing phase. The fibers are usually glass, carbon, or aramid, although other fibers such as paper or wood or asbestos have been sometimes used. The polymer is usually an epoxy, vinyl ester or polyester thermosetting plastic, and phenol formaldehyde resins are still in use. FRPs are commonly used in the aerospace, automotive, marine, and construction industries.

The FRPs used in almost every type of advanced engineering structure, with their usage ranging from aircraft, helicopters and spacecraft through to boats, ships and offshore platforms and to automobiles, sports goods, chemical processing equipment and civil infrastructures such as bridges and buildings. The usage of FRP composites continues to grow at an impressive rate as these materials are used more in their existing markets and become established in relatively new markets such as biomedical devices and civil structures [47].

1.2.1.1   The Matrix

The matrix is the continuous phase, which can be polymer, metal, or ceramic. Polymers have low strength and stiffness, metals have intermediate strength and

stiffness but high ductility, and ceramics have high strength and stiffness but are brittle. The matrix (continuous phase) performs several critical functions, including maintaining the fibers in the proper orientation and spacing and protecting them from abrasion and the environment. In polymer and metal matrix composites that form a strong bond between the fiber and the matrix, the matrix transmits loads from the matrix to the fibers through shear loading at the interface [48].

The matrix also serves as a coating or protector for the fibers and must therefore be chosen not only for its ability to work with the fiber as the load transfer medium but also for its environmental performance. The most important functions for the matrix can be summarized as follows:

- Keep the fibers together and provide a good transfer of the loads

- Provide stiffness and defining the shape of the structure

- Isolate the reinforcement so that each fiber can act independently in the presence of de-lamination or a crack

- Define the superficial roughness of the part

- Protect the reinforcement from chemical attacks and mechanical damages

Polymer matrices can be divided into two general classifications: thermoset and thermoplastic [49]. Polymer matrix composites (PMCs) consisting of a polymer (e.g., epoxy, polyester, urethane) reinforced by thin diameter fibers (e.g., graphite, aramids, boron). For example, graphite/epoxy composites are approximately five times stronger than steel on a weight-for-weight basis. The reasons why they are the most common composites include their low cost, high strength, and simple manufacturing principles. Epoxy is the most popular PMC matrix. More than two-thirds of the polymer matrices used in aerospace applications is epoxy based. The most important reasons made epoxy the most used polymer matrix material are [50]:

- High strength

- Low viscosity and low flow rates, which allow good wetting of fibers and prevent misalignment of fibers during processing

- Low volatility during cure

- Low shrink rates, which reduce the tendency of gaining large shear stresses of the bond between epoxy and its reinforcement

- Available in more than 20 grades to meet specific property and processing requirements

1.2.1.2   The Fibers

Fibers are the most important class of reinforcements, as they satisfy the desired conditions and transfer strength to the matrix constituent. Influencing and enhancing their properties as desired. The orientation of the fiber in the matrix is an indication of the strength of the composite and the strength is greatest along the longitudinal directional of fiber. This doesn't mean the longitudinal fibers can take the same quantum of load irrespective of the direction in which it is applied. Optimum performance from longitudinal fibers can be obtained if the load is applied along its direction. Glass fibers are the earliest known fibers used to reinforce materials [51, 52]. A single fiber usually has a diameter of up to 15 μm [47]. Bigger diameters generally increase the probability of surface defects. The aspect ratio of length and diameter can be ranging from thousand to infinity in continuous fibers. Fibers function as load carrying components in the FRP composites and provide tensile strength, this function needs that the fiber has a high modulus of elasticity, high ultimate strength,a low variation of strength among fibers, high stability of their strength during handling and high uniformity of diameter and surface dimension among fibers [46]. Table 1.1 [47] shows the mechanical properties of different FRP's. Common types of commercially available glass fiber are E-glass and S-

Table 1.1: Mechanical properties of different FRP's. [47]

Material	Modulus of Elasticity (GPa)	Tensile Strength (MPa)
CFRP	$230 - 370$	$179 - 248$
GFRP	$72 - 87$	$172 - 253$
AFRP	$100 - 124$	227

glass, both of which are low alkali boro-alumina-silicate glasses. E-glass fiber, the

workhorse of glass fiber applications, is the lower-cost fiber and is used in both structural and electrical applications. S-glass provides higher tensile properties and increased temperature resistance needed for aerospace and aircraft applications with a price premium. Representative properties for the glass fibers are shown in Table 1.2 [52].

Table 1.2: Fibers used in polymer composites - mechanical properties.

			AS4	IM7	P120		
			PAN−Based	PAN−Based	Pitch−Based		
	E−Glass	S−Glass	Carbon	Carbon	Graphite	Kevlar 49	Boron
Tensile strength (Ksi)	510	670	578	710	325	530	525
Tensile modulus (MSI)	10.5	12.8	35.5	46	120	18	58
Elongation $(\%)$	4.9	5.5	1.6	1.7	0.27	2.5	1
Density (lb/in^3)	0.095	0.09	0.065	0.063	0.079	0.052	0.093

The main role of the reinforcement can be summarized as follows:

- Carry the loads. In a structural composite a percentage between 70 and 90 % of the loads are carried by the internal fibers.

- Provide strength, stiffness, thermal stability and all the other structural properties of the composite.

- Define the thermo-electrical behavior of the material according to the typology of fiber used thus acting as a conductor or an insulator.

1.2.2 Laminated Composites

Laminated composite materials consist of layers of at least two different materials that are bonded together. To analyze a laminated composite structure, the designer must know the properties of each layer and how the reinforcing fibers are oriented with respect to one another that is the stacking sequence as in Figure 1.2. Lamination is used to combine the best aspects of the constituent layers and bonding material in order to achieve a more useful material. The properties that can be emphasized by lamination are strength, stiffness, low weight, corrosion resistance, water resistance, beauty or attractiveness, thermal insulation, acoustical insulation, etc [53, 54].

Laminated composite materials are generally orthotropic and typically have exceptional properties in the direction of the reinforcing fibers, but poor properties perpendicular (transverse) to the fibers. The problem is how to obtain the maximum advantage from the exceptional fiber directional properties while minimizing the effects of the low transverse properties. The plies or lamina directions are oriented in several ways such that the effective properties of the laminate match the design requirements. For purposes of structural analysis, the stiffness of such a composite material configuration is obtained from the properties of the constituent laminate. The procedures enable the analysis of laminates that have individual lamina orientations at arbitrary angles to the chosen or natural axes of the laminate. As a consequence overall behavior of a multi-directional laminate is a function of the properties and stacking sequence of the individual layers [45].
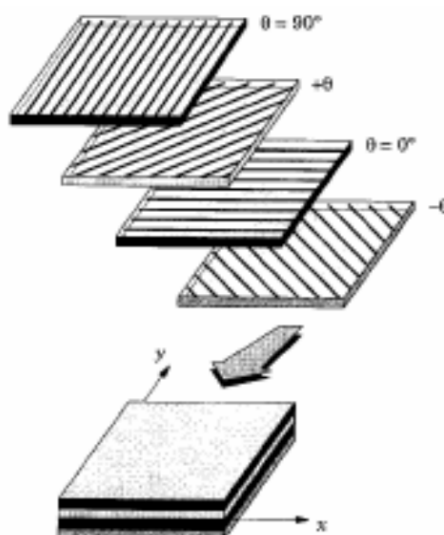

Figure 1.2: A laminate with different fiber orientations.

1.2.2.1   Laminate Code

A laminate is made of a group of single layers bonded to each other. Each layer can be identified by its location in the laminate, its material, and its angle of orientation with a reference axis. Each lamina is represented by the angle of ply and separated from other plies by a slash sign. The first ply is the top ply of the laminate. Special notations are used for symmetric laminates, laminates with the adjacent lamina of the same orientation or of opposite angles, and hybrid laminates. The following examples illustrate the laminate code [55].

$$
\begin{array}{|c|}
\hline
0 \\
\hline
-45 \\
\hline
90 \\
\hline
60 \\
\hline
30 \\
\hline
\end{array}
$$

Figure 1.3: Illustration of $[0/-45/90/60/30]$ laminate.

$[0/-45/90/60/30]$ denotes the code for the above laminate as shown in Figure 1.3. It consists of five plies, each of which has a different angle to the reference x-axis. A slash separates each lamina. The code also implies that each ply is made of the same material and is of the same thickness. $[0/-45/60]_s$ denotes the laminate consisting of six plies as shown in Figure 1.4. The plies above the mid-plane are of the same orientation, material, and thickness as the plies below the mid-plane, so this is a symmetric laminate. The top three plies are written in the code, and the subscript (s) outside the brackets represents that the three plies are repeated in the reverse order [56].

$$
\begin{array}{|c|}
\hline
0 \\
\hline
-45 \\
\hline
60 \\
\hline
60 \\
\hline
-45 \\
\hline
0 \\
\hline
\end{array}
$$

Figure 1.4: Illustration of $[0/-45/60]_s$ laminate.

1.2.3   Sandwich Panel

Sandwich panels offer great potential for the development of optimized structures with high stiffness and strength-to-weight ratio. These panels are a combination of outer skins bonded with structural adhesives to a solid core, a foam core, or honeycomb core material. This structure is a combination of thin, high strength face sheets on each side of a much thicker, light weight core material. Face sheets are rigid and core is relatively weak and flexible as shown in Figure 1.5. Sandwich technology is gradually making the advantages of composites available for an ever wider range of applications [45, 57].
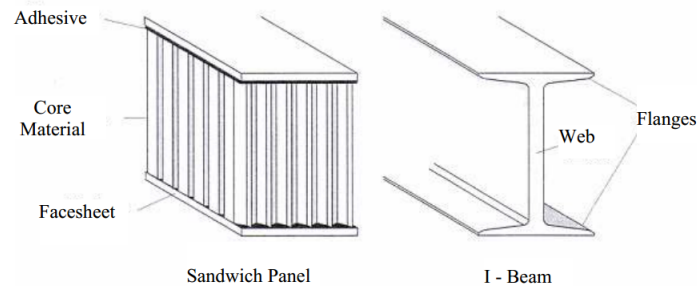
*Figure 1.5:* Sandwich structure in comparison with an I−Beam.

The basic concept of a sandwich structure is that the face sheets carry the bending loads while the core carries the shear loads. The face sheets are strong and stiff in tension and compression compared with the low density core material whose primary purpose is to keep the face sheets separated in order to maintain a high section modulus (a high "moment of inertia" or "second moment of the area"). The core material has a relatively low density (e.g., honeycomb or foam), which results in high specific mechanical properties, in particular, high flexural strength and stiffness properties relative to the overall panel density. Therefore, sandwich panels are efficient in carrying bending loads. Additionally they provide increased buckling resistance to shear panels and compression members. Sandwich construction results in lower lateral deformations, higher buckling resistance and higher natural frequencies than monocoque constructions [45].

Sandwich construction, as applied to polymer matrix composites, is a structural panel concept consisting in its simplest form of two relatively thin, parallel sheets of structural laminated materials bonded to and separated by a relatively thick, lightweight core. The following information is limited to non-metallic sandwich construction used for structural applications. Sandwich construction provides a method to obtain high bending stiffness at the minimal weight in comparison to monolithic laminate construction.

This advantage must be weighed against the risk of increased processing difficulty that can increase production costs over monolithic construction. Damage tolerance and ease of repair should also be considered when selecting a sandwich panel or monolithic laminate construction [58]. The second level of classification is usually made based on the matrix constituent. The major composite classes include **O**rganic−**M**atrix **C**omposites (OMCs), **M**etal−**M**atrix **C**omposites (MMCs), and **C**eramic−**M**atrix **C**omposites (CMCs). The term "organic-matrix compos-

ite" is generally assumed to include two classes of composites: **P**olymer−**M**atrix **C**omposites (PMCs) and **C**arbon−**M**atrix **C**omposites (commonly referred to as carbon-carbon composites). Carbon-matrix composites are typically formed from PMCs by including the extra steps of carbonizing and densifying the original polymer matrix. In the research and development community, **I**ntermetallic−**M**atrix **C**omposites (IMCs) are sometimes listed as a classification that is distinct from MMCs. However, significant commercial applications of IMCs do not yet exist, and in a practical sense, these materials do not provide a radically different set of properties relative to MMCs. In each of these systems, the matrix is typically a continuous phase throughout the component [58].

The second level of classification refers to the reinforcement is: form-particulate reinforcements, whisker reinforcements, continuous fiber laminated composites, and woven composites (braided and knitted fiber architectures are included in this category), as depicted in Figure 1.6 [59].
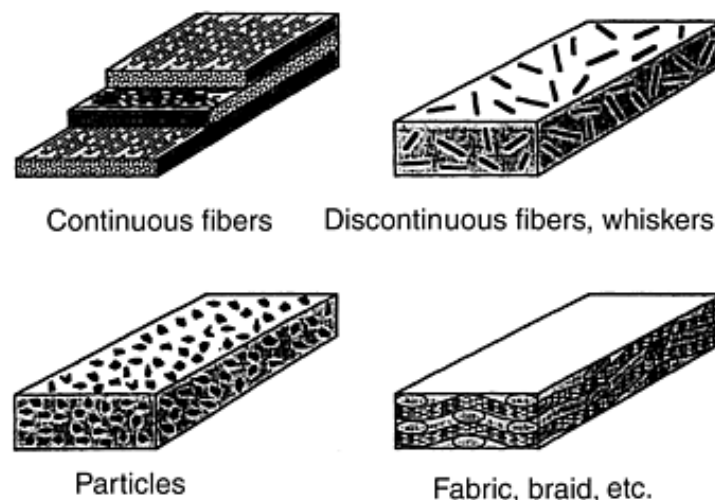
Figure 1.6: Common Types of reinforcements. [59]

For the present work point of view, continuous fiber reinforced polymer or laminated composites has a great intense.

1.3   Modal Analysis of Printed Circuit Boards: An Overview

Printed circuit boards (PCBs) constitute the basis of most electronic devices and are mainly fabricated of thin copper films bounded to fiber epoxy laminates, such

as FR4. Vibrational stress can induce device failure, and hence, studies addressing their modal properties have important applications. This section deals with the vibration characteristics of PCBs using Experimental Modal Analysis (EMA).

1.3.1 Modal Analysis

Modal analysis is the study of the dynamic characteristics of a system by evaluating natural frequencies and damping factors, among other dynamic parameters. This analysis is used to formulate a mathematical model that explains the dynamic behavior of the studied system and is an important tool to optimize the dynamic characteristics of structures and materials [60]. In the case of PCB boards and integrated circuits, their reliability depends, among other factors, on the possibility to endure vibration loads and impacts that can affect their performance. Modal analysis can thus be a very useful tool for engineers to reveal vulnerable areas and avoid premature failure [61–63].

In Experimental Modal Analysis, a structure under test is usually excited by an impact hammer or shaker and measure the response of the structure by Frequency Response Functions (FRFs) between excitation and many points on the structure. An FRF, computed from two signals, describes the level of output signal relative to the input signal sometimes refer to as a **transfer function**. An accelerometer measures the vibration levels at different points on the structure. They convert vibration motion into electrical signals. Analysis of these signals with computer based software gives the nature of vibrations induced in the structure.

1.3.1.1 Types of Modal Analysis

According to Ewins [60], modal analysis methods are classified into Frequency domain of FRFs and Time domain of response histories. In the frequency domain, modal analysis can be divided into three different methods based on number of FRFs which are to be included in the analysis. These three methods are:

- SISO (Single-input, Single-output)

- SIMO (Single-input, Multi-output)

- MIMO (Multi-input, Multi-output)

From the above methods, SISO is the simplest measurement method that describes a single FRF curve for a single input. A SISO data set consists of a set of FRFs measured individuality but sequentially. This method is very useful for PCBs because of their light weight structure, mounting several accelerometers as in SIMO and MIMO will result in erroneous data. Figure 1.7 [64] shows an experimental layout used for modal analysis during this research.
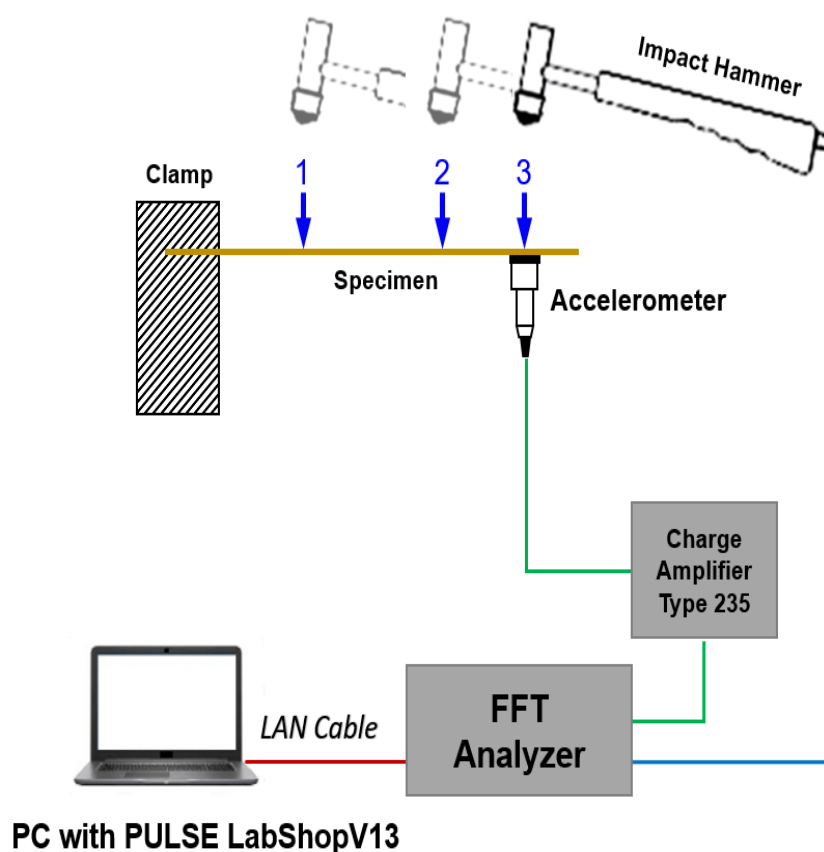

Figure 1.7: Experimental layout for Modal Analysis. [64]

1.3.2   Vibration Testing Hardware

Vibration testing for Modal Analysis involves availability of several hardware components as shown in Figure 1.7 above. Basically, there are three main measurement mechanisms [65]:

- Excitation Mechanism

- Sensing Mechanism

- Data Acquisition and Processing Mechanism

1.3.2.1   Excitation Mechanism

The excitation mechanism provides the input driving force f_t to the structure under test at a specific point. Two of the most commonly used excitation devices are: the exciter, also known as the shaker, driven by power amplifier and the impulse or impact hammer. An Impact hammer, as shown in Figure 1.8, is designed for small to medium structures. It produces short duration vibration level signal, an impulse, by hitting the structure at a specific point. The hammer is instrumented with a force sensor that produces a signal proportional to the force of impact. This device excites a broad range of frequencies depending on the hammer head mass and impact tip material. Usually, for low range frequencies a soft rubber tip is used while for high range a metallic tip is convenient.
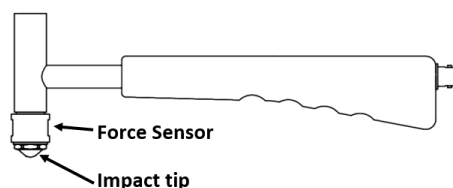
Figure 1.8: Impact Hammer with a force sensor.

Figure 1.9 shows a typical hammer response.
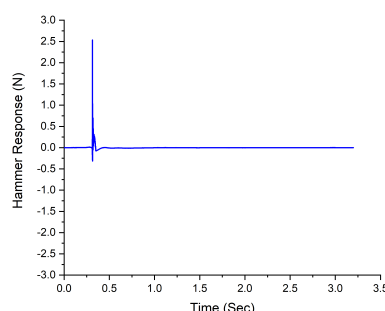
Figure 1.9: Impact Hammer response in time domain.

1.3.2.2   Sensing Mechanism

The sensing mechanism consists of the sensing devices such as transducers (accelerometers). The piezoelectric accelerometers, for measuring acceleration response, are the most common type used in experimental modal analysis [65]. Accelerometers generate electrical signals that are proportional to the measured acceleration. Most of the time, these signals are weak in strength; to overcome this issue, the conditioning amplifiers are frequently. The accelerometers used now a days consist of internal circuitry to eliminate signal strength and noise issues.The conditioning amplifiers are not needed with these type of accelerometers.

Figure 1.10 shows a section view of the piezoelectric accelerometer. It consists of a metallic case, a seismic mass, a piezoelectric material, and a base. When the structure vibrates, the base of the accelerometer moves. This motion is transmitted to seismic mass that generates a proportional force on the piezoelectric crystal that deforms a bit as a result. This deformation or external stress produces a high-impedance, electrical charge proportional to the force and hence, ultimately, to the acceleration of the seismic mass and the structure. Although theses devices operate well over a wide frequency range, still they are not well suited for low frequency applications [65].
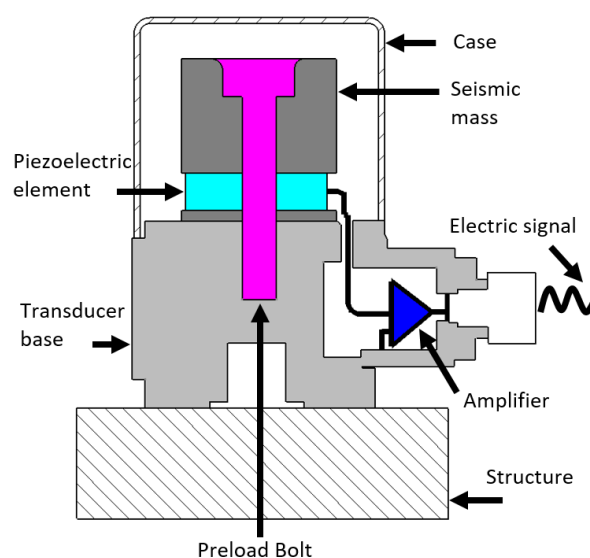
Figure 1.10: Cross section view of a piezoelectric accelerometer.

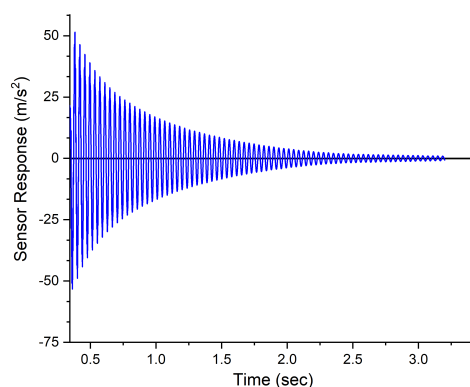Figure 1.11 shows a typical time response of an accelerometer after and impact on the structure.

Figure 1.11: Plot of the accelerometer response after an impact.

1.3.2.3   Data Acquisition and Processing Mechanism

The final measurement mechanism in EMA, is the data acquisition and processing mechanism. The main objective of this mechanism is to measure signals developed by the sensing mechanism and to find out the magnitudes and phases of the input and output signals. The equipment used for analyzing vibration signals, is commonly known as Fast Fourier Transform (FFT) signal analyzer. These analyzers provide direct measurement of the FRFs and are based on FFT algorithm as shown in Figure 1.7.

Figure 1.12 shows an FFT signal analyzer architecture. It takes analog time domain signals from multiple input channels and convert them into digital frequency domain information that can then be processed through digital computer.
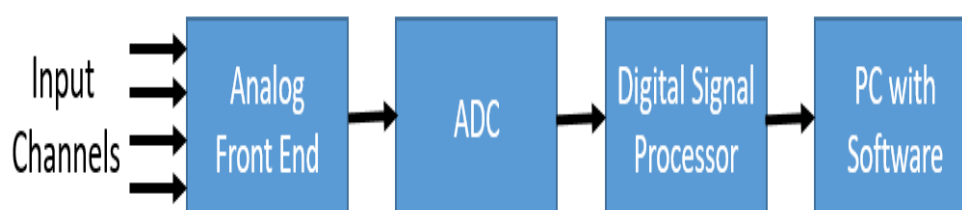
Figure 1.12: Signal analyzer architecture.

1.3.3   Modal Parameter Extraction

The next stage, after obtaining FRFs data in EMA, is to extract modal parameters such as modal frequencies, modal damping and mode shapes. The "Global Parameters" i.e., modal frequencies and damping can be obtained from all frequency response measurements on the test structure except where the displacement is zero. However, to accurately modal the associated mode shape, the structure should be covered by sufficiently measurement points or degrees of freedom.

1.3.3.1   Determination of the Modal Frequencies

The modal frequencies for SDOF system are usually obtained by the so-called peak−picking or peak amplitude method [65]. In this method, the individual resonance peaks, the highest peaks in the magnitude of FRF curve, are detected on the FRF plot as shown in Figure 1.13. The frequency at which highest peak occurs is the natural frequency of that mode.
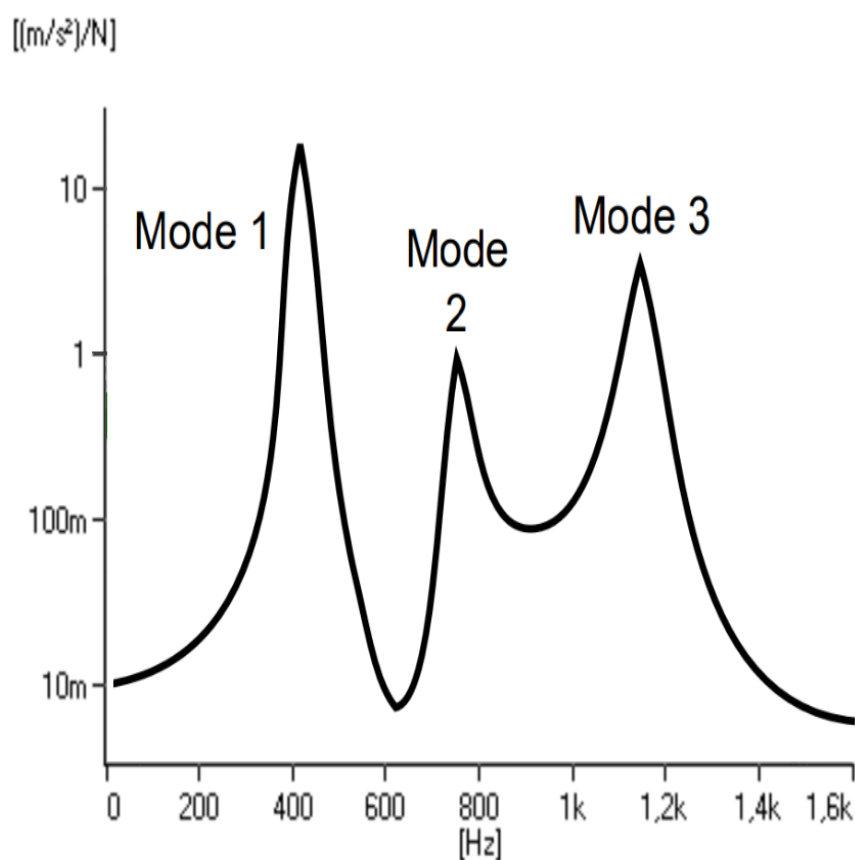
Figure 1.13: Plot of the frequency response function.

1.3.3.2   Determination of the Modal Damping

The modal damping can be found by identifying the half power (-3dB) points of the magnitude of the frequency response function as shown in Figure 1.14.
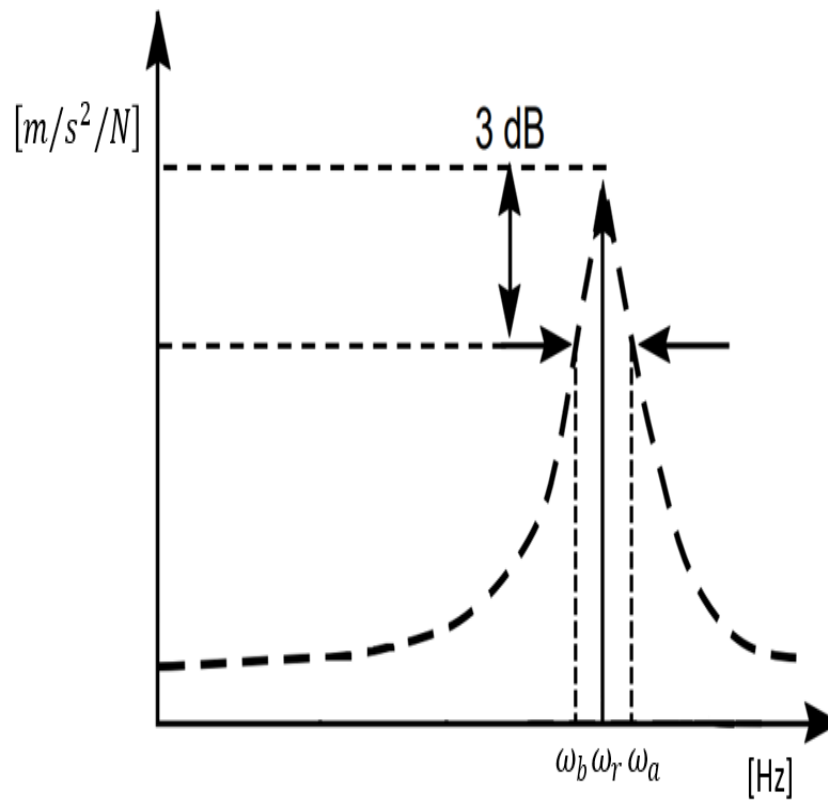
Figure 1.14: Plot of the frequency response function.

This method of finding the modal damping is known as half power band width method. According to this method, the damping ratio ζ_r can be found from the following equation:

$$\eta_r = \frac{\omega_a^2 - \omega_b^2}{2\omega_r^2} \cong \frac{\Delta\omega}{\omega_r}$$
$$\zeta_r = \frac{\eta_r}{2}$$

(1.1)

Where $\Delta\omega$ is the frequency bandwidth between the two half power points and ω_r is the resonance frequency.

1.4   Introduction to Sheet Resistance and Measurement Methods

Sheet resistance or surface resistivity is a measure of the resistance between the opposite sides of a thin square material. It is a common electrical property used to characterize thin metal films. Surface resistivity is independent of physical dimensions of the material. In practice, the unit of sheet resistance is Ω/sq[1].

This section will describe the methods to determine sheet resistance using two common techniques such as Four-Point Probe method and Van der Pauw method. Although both the measurement methods are similar in measuring sheet resistivity while minimizing the effect of parasitic resistance. However, their assumptions and mathematical derivations are different. Also, in case of four-point probe, the probes are placed ideally at the center of the sample, as shown in Figure 1.15; whereas in case of Van der Pauw method, the probes are placed in arbitrary locations on the periphery of the sample, as shown in Figure 1.16. In addition, Van der Pauw measurements don't require samples to have an infinite lateral dimension as in the ideal four-point probe geometry.

1.4.1   Four-Point Probe Method

Four-point probe is the most commonly used method for measuring sheet resistivity of thin wafers [66]. Wenner [65] in 1916 proposed this method for the first time to measure earth's resistivity. In 1954, Valdes [68] adopted this method for semiconductor wafer resistivity. Usually probes are co-linear, i.e., arranged in-line with equal probe spacing, however other configurations are also in practice [67].

A four-point probe setup as shown in Figure 1.15 consists of four equally spaced co-linear probes. A small amount of DC current, from a constant current source, is applied through the outer two probes (1 and 4) and the voltage drop is measured between the inner two probes (2 and 3). The sheet resistance R_{sh} for a thin film with thickness t, where $t \ll a$ or d, is given by [66]:

$$R_{sh} = \frac{V}{I} \cdot C \quad [\Omega/sq] \tag{1.2}$$
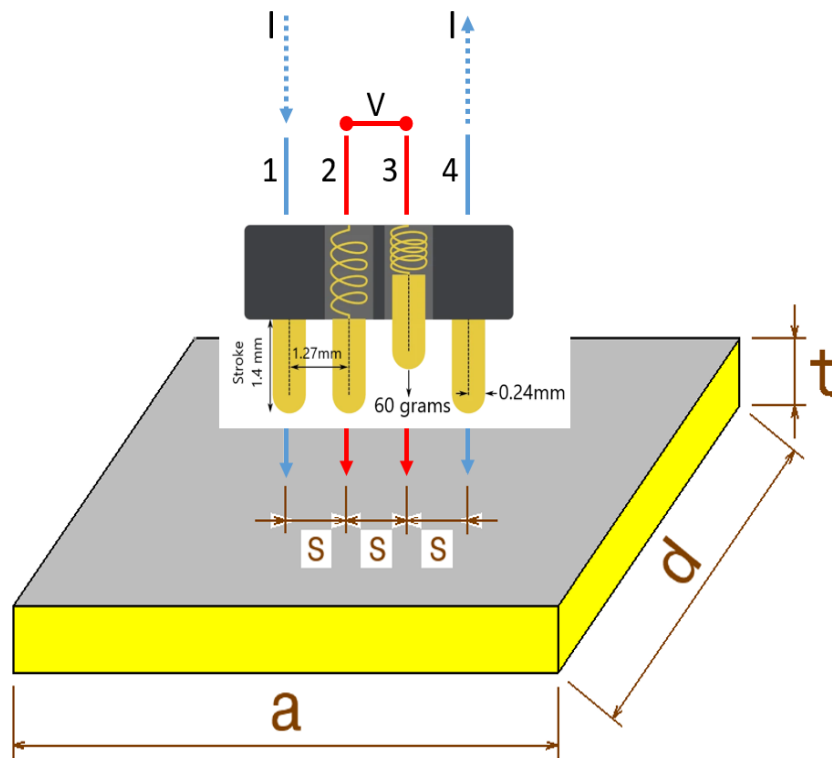
---

[1]Ohms per square

Figure 1.15: Four-point probe setup. [66]

Where C is the correction factor account for sample thickness, geometry, prob spacing and location of the probe on the sample. A large number of research articles have been published on correction factors, with results outlining the necessary adjustments.If $d \gg S$, where S is the probe spacing, the equation 1.2 becomes:

$$R_{sh} = \frac{\pi}{\ln 2} \cdot \left(\frac{V}{I}\right) \approx 4.53 \left(\frac{V}{I}\right) \cdot CF \quad [\Omega/sq] \tag{1.3}$$

Here CF is the lateral correction factor for the probe.
and if t is the thin film thickness, then the resistivity (ρ) is:

$$\rho = R_{sh} \cdot t \qquad [\Omega \cdot m]^1 \tag{1.4}$$

Similarly, Electrical conductivity (σ), an intrinsic property of a material, is the measure of the amount of electrical current a material can carry or able to carry. Electrical conductivity, also known as specific conductance, is the reciprocal of resistivity.

$$\sigma = \frac{1}{\rho} \qquad [S/m]^2 \tag{1.5}$$

---

[1] Ohms meter

[2] Siemens per meter

1.4.2   Van der Pauw Method

The Van der Pauw technique is another widely used technique to determine the resistivity of uniform arbitrary shaped samples. First introduced in 1958 by Van der Pauw [70, 71], the specific resistivity of a flat arbitrary shaped sample can be measured without even knowing the current pattern. The method is based on the following assumptions [69]:

- Contacts should be sufficiently small

- Contacts should be at the circumference of the samples

- Sample should be of uniform thickness

- There should not be any holes on the surface of the sample

Figure 1.16 shows a flat sample of arbitrary shape with four (1,2,3 and 4) very small ohmic contacts along the periphery. The current I_{12} passes the sample through contact 1 and leaves through contact 2 and the measured voltage difference between the contact 3 and 4 is $V_{34} = V_3$ - V_4.
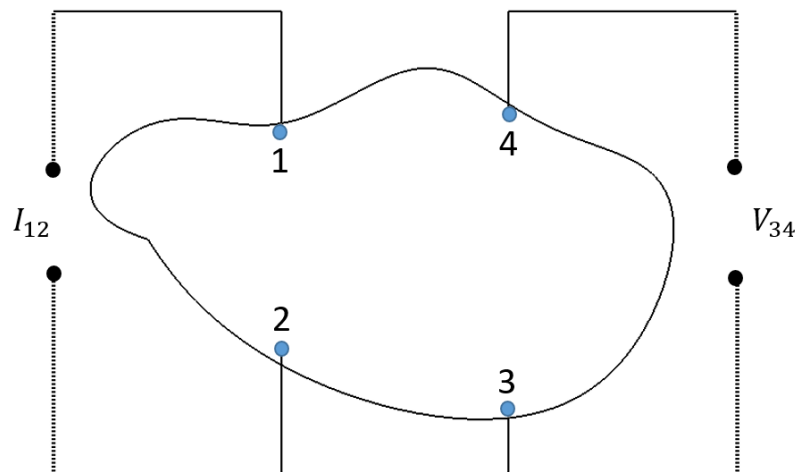
Figure 1.16: Arbitrarily shaped sample with four contacts for resistivity measurements. [69]

The resistance $R_{12,34}$ is then:

$$R_{12,34} = \frac{V_{34}}{I_{12}} \tag{1.6}$$

Similarly, resistance between contacts 23 and 41 is $R_{23,41}$ and the resistivity ρ is given by [70]:

$$\rho = \frac{\pi}{\ln 2} \cdot t \frac{(R_{12,34} + R_{23,41})}{2} \cdot F \tag{1.7}$$

Where F depends on the ratio $R_r = \frac{R_{12,34}}{R_{23,41}}$ [67].

For symmetrical samples, as shown in Figure 1.17,
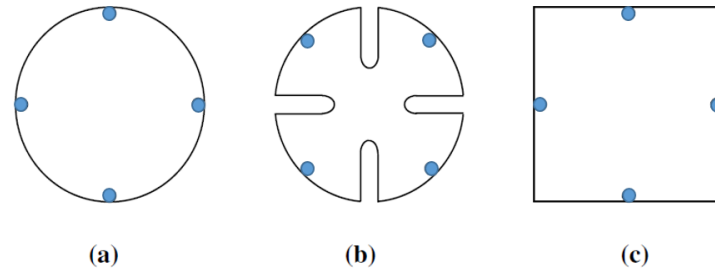
Figure 1.17: Typical symmetrical geometries. [69]

where $R_r = 1$ and $F = 1$. Then

$$\rho = \frac{\pi}{\ln 2} \cdot t \cdot R_{12,34} \approx 4.54 \cdot t \cdot R_{12,34} \qquad [\Omega \cdot m] \tag{1.8}$$

and the sheet resistance becomes:

$$R_{sh} = \frac{\pi}{\ln 2} \cdot R_{12,34} \approx 4.54 \cdot R_{12,34} \qquad [\Omega/sq] \tag{1.9}$$

The above expression for sheet resistance is similar to the one obtained by four-point probe method in 1.3. The Van der Pauw equations are based on the assumptions as described above, therefore different correction factors are normally used [72, 73].

1.5   An Overview of Micro Electro Mechanical Systems (MEMS)

The growth in the semiconductor industry makes possible, for the researchers, to design and fabricate miniature sensors, and micro-systems.The integration of micro-sensors, micro-actuators, and micro-electronics using silicon-based micro-fabrication technology refers to what is known as micro-electromechanical systems or in short MEMS. Being one of the growing technologies of the current era, MEMS has the

potential to take both industrial and consumer products up to a remarkable level. Due to the new and rapidly evolving MEMS technologies and applications every day, our lives and the way we live are changing dramatically.

The multidisciplinary nature of MEMS has several advantages as a manufacturing technology and has avast range of applications including household electronics, automobiles, biomedical, etc. Batch fabrication and micro-machining technologies make MEMS to be reduced in size and cost and high in performance and reliability [75]. A lot of research has been done in the field of MEMS still there are many issues that need to be addressed to make complete micro-systems [74].

1.5.1   MEMS Fabrication Methods

MEMS devices are fabricated using batch fabrication method; it is an economical way of producing a large number of devices from a single wafer. The fabrication methods for MEMS are generally categorized into three categories:

- Surface micromachining

- Bulk micromachining

- LIGA (**L**ithographie, **G**alvanoformung, **A**bformung)

Based on CMOS technology, Surface micro-machining, also known as sacrificial surface micro-machining, involves thin films of a structural material and a sacrificial material to realize thin mechanical structures by using deposition, patterning, and etching. This technique is suitable for thin structures with an overall thickness of less than 15 μm [76].

Since its emergence in the 1960s, bulk micro-machining has been used in the fabrication of many commercial devices [77]. It uses different etching processes to produce a micro-mechanical structure within the bulk of silicon wafer by removing the selective wafer material. Bulk micro-machined structures can range from tens of microns to a millimeter thick [76].

LIGA process mainly consists of lithography, electroplating and molding, involves high energy X-ray synchrotron radiation to expose a thick layer of resist to develop

a resist structure. Metal deposition fills the resist mold with a metal and a free-standing metal structures results after removing resist [78]. This process results in high aspect ratio structures.Figure 1.18 shows three MEMS fabrication methods.
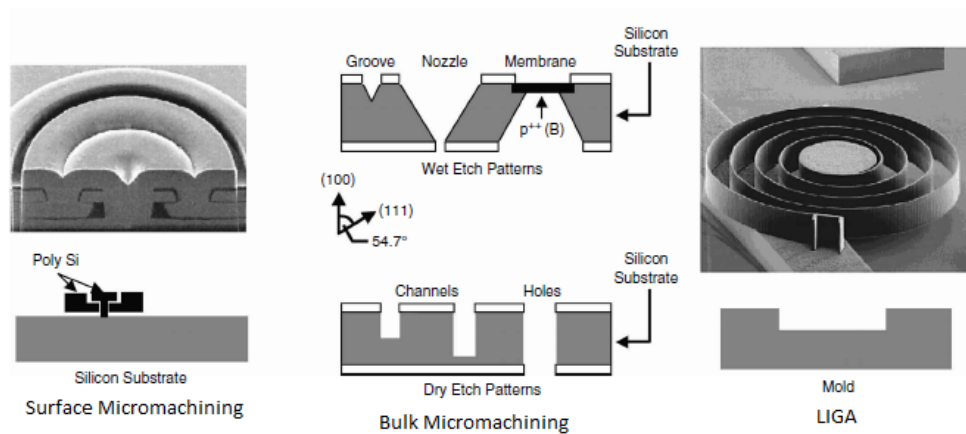

Figure 1.18: Types of MEMS fabrication technologies. [79]

1.5.2 MEMS Applications

MEMS are now becoming an integral part of the most of technical fields. Some of the MEMS application areas are:

- Consumer products

- Aerospace

- Automotive

- Biomedical

- Chemical

- Optical displays

Chapter 2

Thesis Objectives

The literature, reviewed in the preceding sections, shows a large amount of research has been conducted to study vibration characteristics of thin films and their behavior under mechanical loadings but there are many other important parameters which are crucial for the performance and reliability of printed circuit boards and MEMS devices. These parameters e.g., stress amplitude, mean stress, downsizing film dimension and crack initiation and propagation still need more study and investigations.

2.1 Objectives

The overall objective of this thesis is to study the electrical properties and surface characterization of thin copper films bounded to fire retardant (FR4) epoxy laminates.

To achieve this general objective, the following aspects have been focused on:

- Experimental and Numerical Simulation Study of the Vibration Properties of Thin Copper Films Bonded to FR4 Composite.

    - Studying the modal parameters such as modal frequencies and damping ratios using Experimental Modal Analysis EMA

    - Correlating experimental and numerical results using FEM approach

- – Determination of Young Modulus E

- Variation of Electrical Properties under Different Loading Cycles and Temperatures of Thin Copper Films Bonded to FR4 Composite

    - – Studying the effect of mechanical vibrations on sheet resistance, resistivity and conductivity of PCBs under different temperatures and mechanical cycles.

    - – Development of a dual axes four point probe (DA4PP) with thermal loading

    - – Development of a high frequency vibration design system

- Interfacial Characterization of Thin Copper Films Bonded to FR4 Composite under High Cycle Vibration Stress

    - – Studying the surface damage behavior of PBCs using environmental scanning electron microscopeESEM before and after mechanical loadings

    - – Surface composition analysis of the samples

    - – Analysis of the samples using water droplet contact angle technique

This thesis is a contribution to a better understanding of the relationship between damage accumulation and electrical performance of PCB boards and MEMS and may lead to improve their performance. This will make the results of great practical importance and to develop assay methodology that can be extended to other thin films.

Chapter 3

Experimental Setup

This chapter gives details of experimental setup and methodologies used for vibration characteristics of thin copper films bounded to FR-4 epoxy laminate using modal analysis and measurements of sheet resistance of the same material, subjected to high frequency vibrations, using four probe method. Experimental setup for surface analysis using Environmental Scanning Electron Microscopy (ESEM) and contact angle measurements also described in this chapter.

3.1   Modal Analysis

This section briefly describes the material and tools used to determine dynamic properties of PCBs and compared with finite element method (FEM) analytical results, in order to gain basic knowledge of the vibration characteristics of copper/FR4 PCBs.

3.1.1   Materials and Methods

3.1.1.1   Materials

The specimens used for vibration analysis were made of single-layer C_u film (thickness 35 μm) bonded to FR4 epoxy laminate sheet (thickness 1.6 mm). The specimens were categorized into four groups, as shown in Figure 3.1 and Tables 3.1—

3.4. The specimens were cut from a 305 mm long and 210 mm wide panel to equal lengths of 150 mm, using a Protomat S103 (LPKF GmbH, Garbsen, Germany).
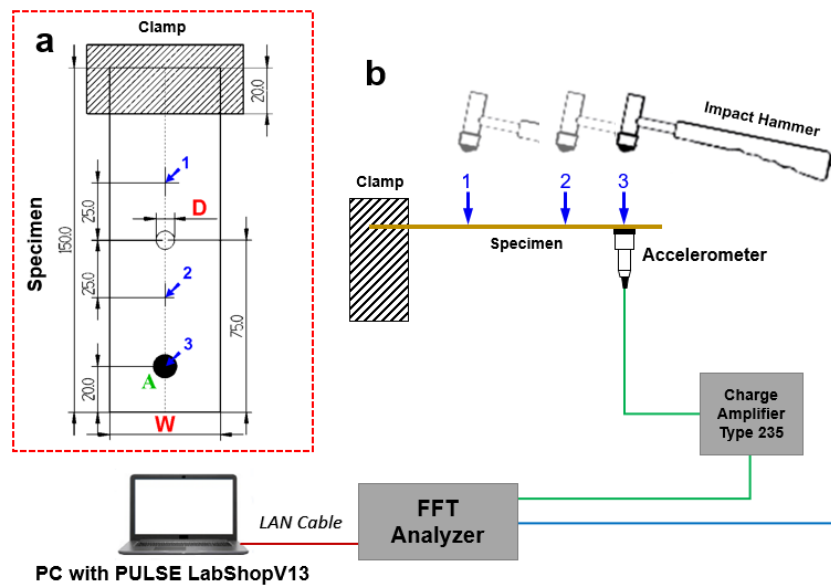
Figure 3.1: (*a*) Specimen dimensions (in *mm*): width (*W*) and diameter (*D*) are variable, as indicated in Tables. (*b*) Schematic layout of the experimental setup. The numbered positions (1–3) in blue in both figures indicate the hammer impact positions.

Table 3.1: Group 1: Constant width/diameter ratio with center hole.

$W^{\dagger}$ (mm)	$D^{\ddagger}$ (mm)	D/W *
12	2	6
18	3	6
24	4	6
30	5	6
36	6	6
42	7	6
48	8	6

$\dagger$ W:width; $\ddagger$ D:diameter; * D/W: aspect ratio.

Table 3.2: Group 2: Constant aspect ratio without center hole. ($D = 0$).

W (mm)	D/W
12	6
18	6
24	6
30	6
36	6
42	6
48	6

Table 3.3: Group 3: Constant width (24 mm) with variable center holes.

W (mm)	D (mm)
24	2
24	3
24	4
24	5
24	6
24	7
24	8

Table 3.4: Group 4: Constant width (30 mm) with variable center holes.

W (mm)	D (mm)
30	2
30	3
30	4
30	5
30	6
30	7
30	8

3.1.1.2   Experimental Vibration Analysis

Figure 3.2 shows a photograph of the experimental setup and specimen of group 1. An accelerometer type 4393 (Brüel & Kjær,Wien, Austria) with a charge amplifier type 2635 (Brüel & Kjær) was mounted below the specimen by using bees wax to measure vibrations excited by an Impact Hammer type 8206 (Brüel & Kjær) with a plastic tip at locations 1, 2, and 3 as in Figure 3.1. Five hammer impacts were given at each location and the results were averaged to scale back the effect of noise within the acquired signal. A strong clamping structure was used to fix one end of the test specimen, while the other side was kept free to be considered as a cantilever.
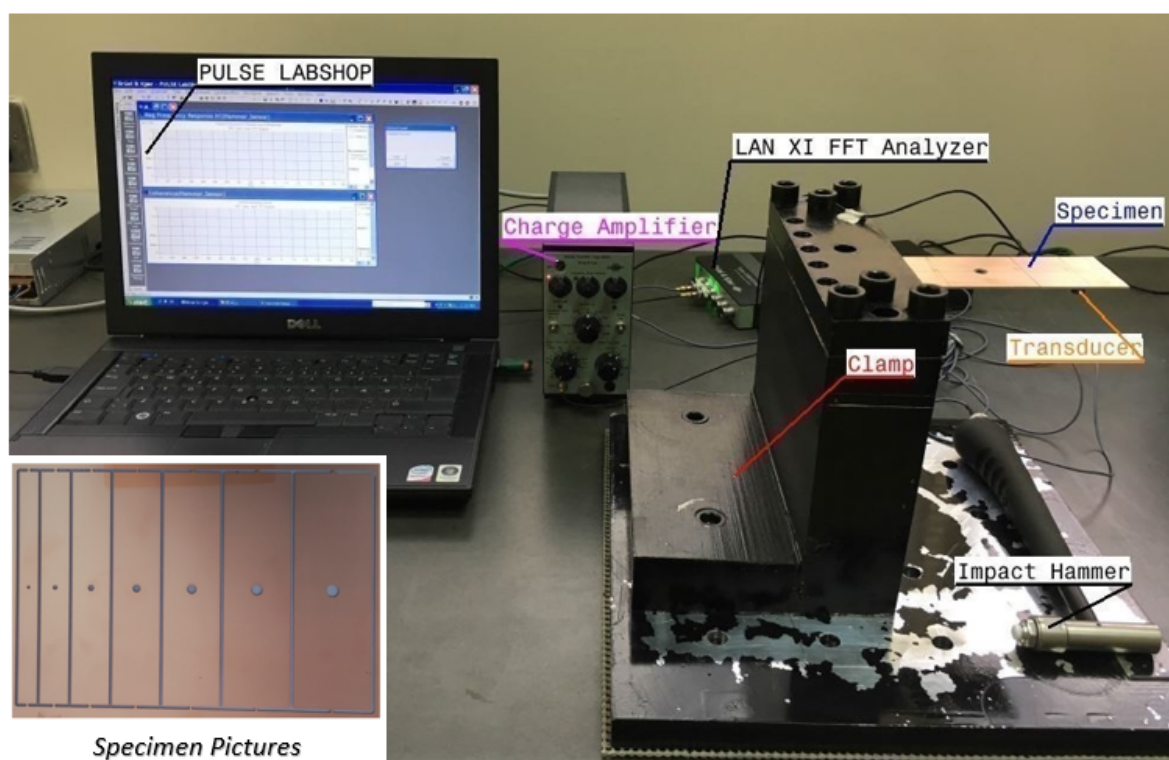
Figure 3.2: Photograph of the experimental setup and specimen of Group 1.

The averaged vibration data was captured using a LAN XI type 3050-A-060 (Brüel & Kjær) hardware module. The data was then analyzed by PULSE LabShop V13.5.0 (Brüel & Kjær) to determine the dynamic properties such as natural frequencies, mode shapes, and damping ratios by extracting information from frequency response function (FRF) curves. The damping ratios were calculated by the PULSE LabShop using the Half Power Band Width method [80].

3.1.1.3   Theoretical Model

To validate the experimental data, the natural frequencies of a rectangular beam of 150 mm x 24 mm x 1.6 mm and a plate of 150 mm x 48 mm x 1.6 mm were calculated using the Rayleigh method [01]. According to this method, the natural frequency (f_n), as per Equation 3.1, of a uniform composite rectangular cantilever beam is:

$$f_n = \frac{K}{2\pi} \cdot \sqrt{\frac{EIg}{\omega L^4}} \tag{3.1}$$

where K is the modal constant (0.56 [79]), EI is the composite beam stiffness factor for FR4 ($1.45\text{x}10^{-2}$kg·m^2), g is the acceleration of gravity (9.81m/s^2), w is the linear mass density for FR4 ($0.1169\ kg/m$), and L is the length of the composite beam (130 mm). The natural frequency of a uniform rectangular cantilever plate, as per Equation 3.2, is:

$$f_n = \frac{K}{a^2} \cdot \sqrt{\frac{D}{\rho}} \tag{3.2}$$

where K is the modal constant (0.56 [79]), a is the length of the plate (130 mm), D is the plate stiffness factor for FR4 (5110 kg/m), and ρ is the mass per unit area ($5.64\text{x}10^{-5}$kg·s^2·m^{-3}). Since the Young Modulus (E) is the key element in the vibration response of any structure, the estimation of E was done both theoretically and experimentally. The estimated Young modulus of a rectangular PCB (E_{PCB}) was calculated to be 20.6 GPa from the stiffness of the two composing materials [81] and their material fraction according to Equation 3.3.

$$E_{PCB} = E_{FR4}\left(\frac{V_{PCB} - VCu}{V_{PCB}}\right) + E_{Cu}\left(\frac{V_{Cu}}{V_{PCB}}\right) \tag{3.3}$$

where E_{FR4} is the Young modulus of FR4 (18.60GPa), V_{PCB} is the volume of the PCB ($5.6\text{x}10^{-6}$m^3), V_{Cu} is the volume of the copper layer ($1.26\text{x}10^{-3}$m^3), and E_{Cu} is the Young modulus of copper (108 GPa). Figure 3.3 shows the stress−strain curve and the broken specimen corresponding to specimen 3 of Group 2. The experimental value of E_{PCB} was found to be 21.59 GPa. The parameters for the tension test were taken from the previous work [82]. The measured first four modes of vibration, obtained from experimental modal analysis of all the specimens, were then compared by analytical modal analysis using FEM with ANSYS 13.0 with Mechanical APDL solver using a fixed end (cantilever) as boundary condition.
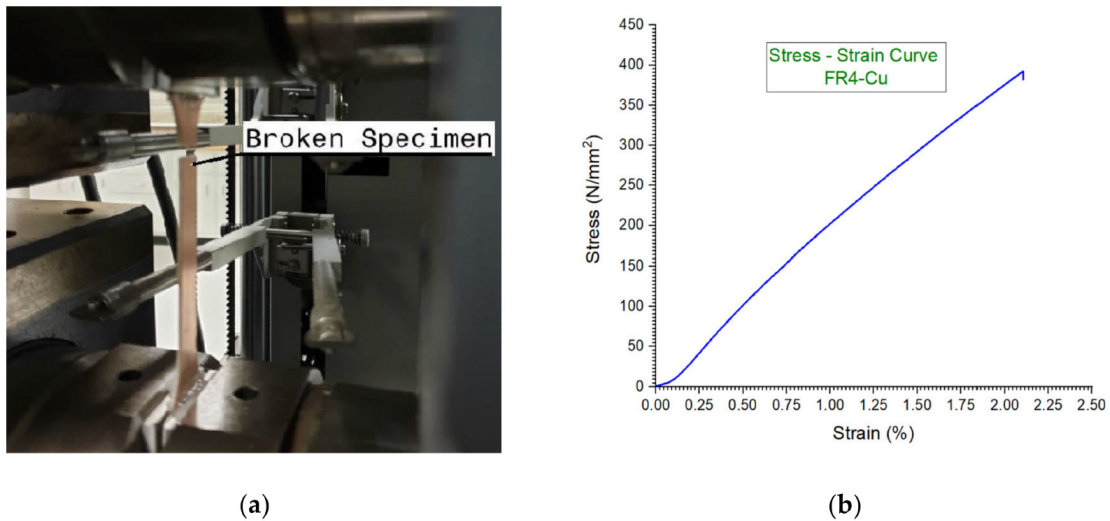
Figure 3.3: Experimental estimation of E_{PCB}. (a) Specimen under test (sample 3 of Group 2), (b) stress – strain curve of the specimen depicted in (a).

Figure 3.4 shows typical mesh models used for samples with (a) and without (b) holes. The shell element SOLSH190 (size 2 mm) was used and element numbers
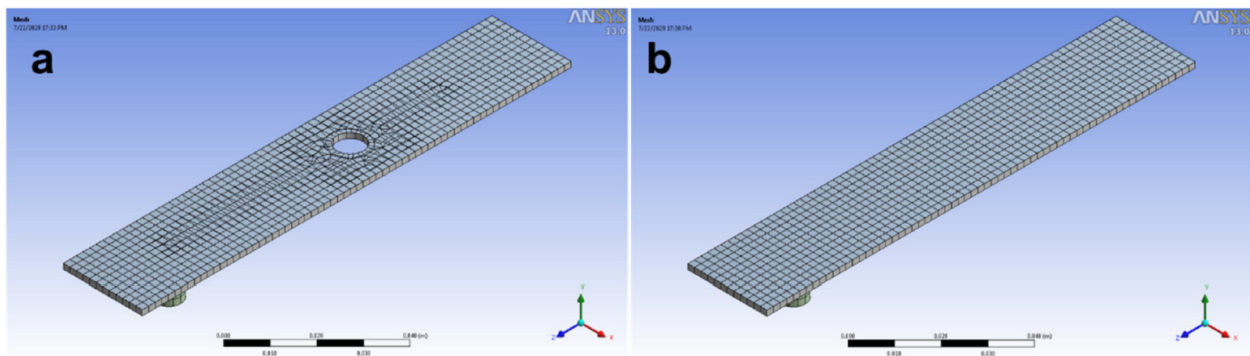

Figure 3.4: Examples of mesh models used for finite element method (FEM) analysis: (a) Group 3 sample (W = 24, D = 8); (b) Group 2 sample (W = 24).

varied from 1698 to 3721, depending on sample dimensions. To analyze the measured and predicted natural frequencies, an experimental value was plotted against the predicted one for each of the modes included in the comparison. This plot provides a set of correlated mode pairs (CMPs) [05] used to check the degree of correlation between the two sets of results.

The predicted and measured natural frequencies were also used to calculate the Natural Frequency Difference (NFD) value [83]. This method helps to assess the difference of the natural frequencies among all possible combinations of experimental

and analytical model modes. NFD was calculated using Equation 3.4:

$$NFD_{A,X} = \frac{|f_A - f_X|}{min(f_A, f_X)} \tag{3.4}$$

where f_A and f_X are the natural frequencies obtained from analytical (FEM) and experimental modal analysis, respectively.

3.2   Electrical Properties

The specimens used for measuring electrical properties, such as sheet resistance, resistivity and conductivity, were made of single-layer C_u film (thickness 18 μm) bonded to FR4 epoxy laminate sheet (thickness 1.5 mm). The specimens were cut from a 310 mm long and 210 mm wide panel to equal dimensions of 50x25 mm, using Protomat S103 (LPKF GmbH, Garbsen, Germany) circuit board plotter. Three isolated rectangles, (zone A, zone B, zone C) of 10x5 mm dimensions, were cut using 0.1 mm micro cutter. The electrical properties of each rectangle were then measured separately using custom made dual axes four−point probe (DA4PP). Figure 3.5 shows the photograph of the specimen with actual dimensions and isolated rectangles.The shaded area represents the clamping side of the specimen to the rigid structure, while the blue area, the other side of the specimen, is linked to the shaker by means of a rod on which load cell is mounted. The specimens were categorized
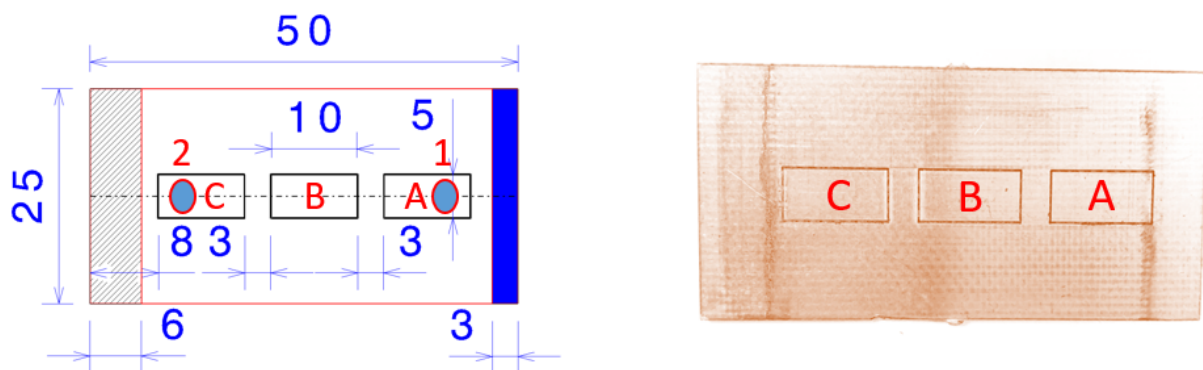
Figure 3.5: Photograph of the specimen with dimensions.

into three sets and each set further consists of three samples with three isolated rectangles on each sample, as shown in Tables 3.5 and 3.6. This experimental work is conducted in two stages. At the first stage samples are subjected to high frequency vibrations for different number of cycles at constant load $\sim$30 N and at

Table 3.5: Experimental scheme for high frequency vibrations.

Set 1			Set 2			Set 3		
A	B	C	A	B	C	A	B	C
	$S11$			$S21$			$S31$	
	$S12$			$S22$			$S32$	
	$S13$			$S23$			$S33$	

Table 3.6: Number of cycles for different specimens.

Specimen	Number of cycles
$S11$	$200,000$
$S12$	$200,000$
$S13$	$200,000$
$S21$	$500,000$
$S22$	$500,000$
$S23$	$500,000$
$S31$	$800,000$
$S32$	$800,000$
$S33$	$800,000$

a sinusoidal frequency of 50 Hz. After achieving the required number of cycles, through digital frequency counter, the samples are tested for sheet resistance at the **surface** temperatures of 25^0C, 35^0C and 45^0C. The resistivity measurement setup consists of two separate experimental setups. These are:

- Four Point Probe Design

- High Frequency Vibration Design

The four point probe design setup is used to measure sheet resistance before and after applying vibrations to the samples and the high frequency vibration design setup is used for external forced vibrations.

3.2.1   Four Point Probe Design

Figure 3.6 the dual axes four point sheet resistance measurement device.
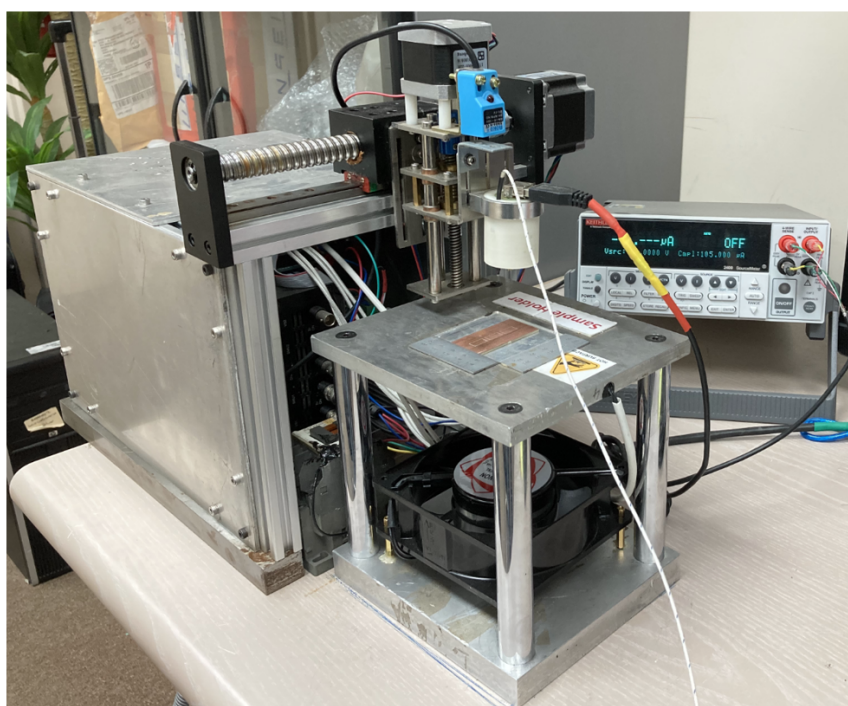
Figure 3.6: Photograph of the dual axes four point sheet resistance measurement device.

The experimental setup consists of:

- a probe head,

- a sample holding stage with thermal input,

- an auto-mechanical stage,

- a source measure unit (SMU),

- and Graphical User Interfaces (GUIs) for probe head movement and resistance measurement.

3.2.1.1   Probe Head

Figure 3.7 shows the custom made probe head with inline probes. It consists of four gold plated tungsten metal probes having 0.24 mm radius and equal spacing.
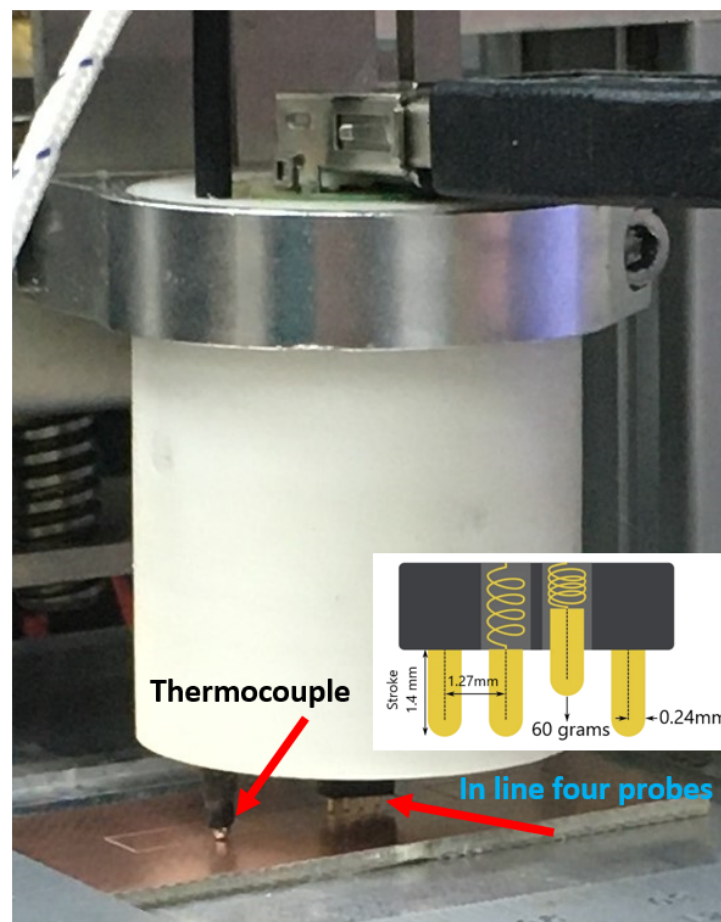
Figure 3.7: Photograph of the Probe head.

Each probe pin is supported by springs on the other end to minimize sample damage during probing. The probe head is part of an auto-mechanical stage which travels in two axes up-down and left-right for taking measurements. A keithly 2400 high impedance current source is used to supply current through the outer two probes and measure the voltage across the inner two probes. These values of sourced current and measured voltage are used to determine the sample resistivity. The probe spacing S is 1.27 mm. The probes exert 60 grams of force on the sample when fully pressed and have stroke length of 1.4 mm. A J type thermocouple is also part of the probe head to record surface temperature of the specimen under test. The surface temperature of the sample is recoded by 8-channel thermocouple data logger type TC-08 (Pico Technology Ltd.) as shown in Figure 3.8.

Figure 3.8: Photograph of the 8-channel thermocouple data logger.

Figure 3.9 shows typical temperature plot taken at different surface temperatures using thermocouple mounted on the probe head.

3.2.1.2 Sample Holding Stage

The sample holding stage consists of the silver plate that can be heated using two 100 W, 220 V silicon heaters, from Keenovo International, installed at the bottom of the plate. The temperature of the inner plate surface is controlled by PID temperature controller. The sample to be tested is placed at the top of the plate as shown in Figure 3.10.
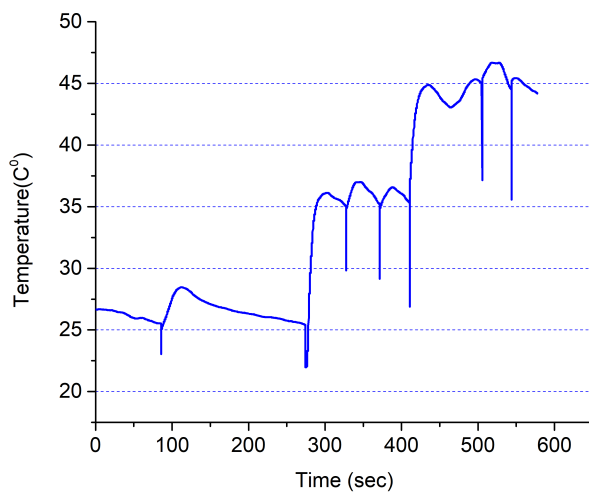
Figure 3.9: Surface temperature plot from the 8-channel thermocouple data logger.
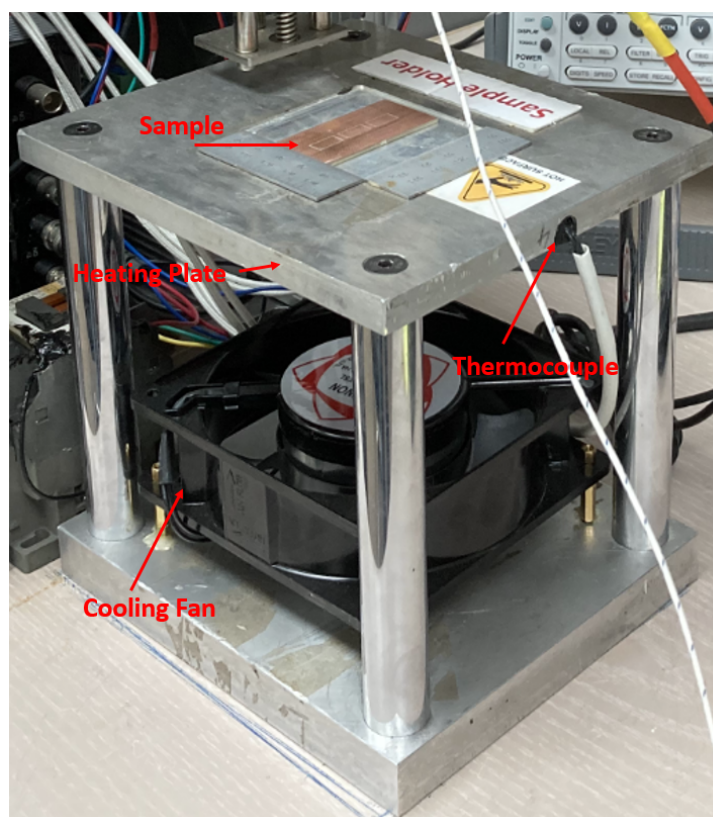
Figure 3.10: Photograph of the sample holding stage.

3.2.1.3   Auto-Mechanical Stage

The auto-mechanical stage consists of two NEMA17 stepper motors for up-down and left-right movements of the probe head. The two motors are coupled with lead screws having 4 mm and 5 mm lead, 12 mm and 16 mm shaft diameters, 1.8^0 step angle and 0.1 mm resolution respectively. There are two inductive limit switches to know the start position of the probe head. The probe head is installed on the vertical axis using aluminum clamp with 32 mm internal diameter as shown in Figure 3.11. A PID temperature controller is also part of the mechanical stage. It is used to control the temperature of the top plate of the sample holding stage.
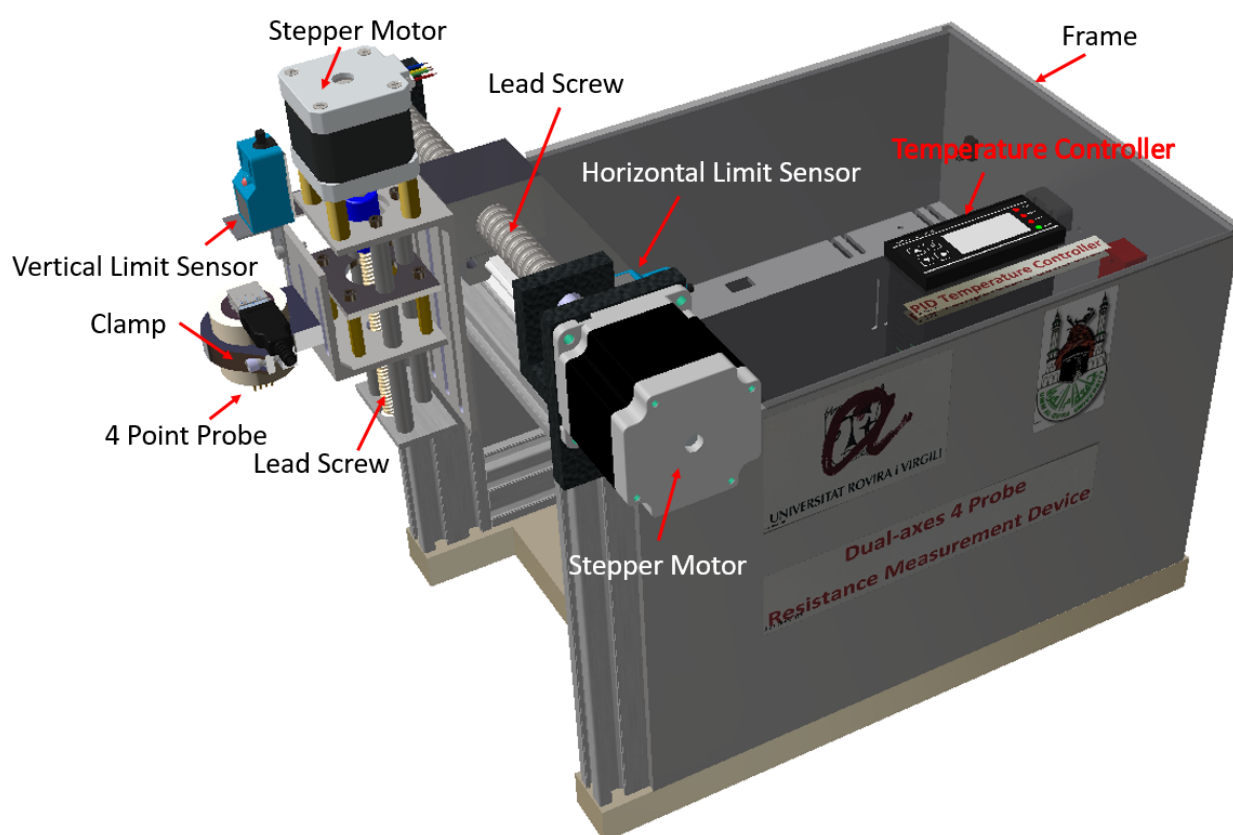
Figure 3.11: 3D model of the auto-mechanical stage.

3.2.1.4   Source Measure Unit (SMU)

For the measurement of sheet resistance of the conductive materials, a tightly coupled sourcing and measurement instrument is needed. Keithley's Source Meter 2400 is used for this purpose as shown in Figure 3.12. It provides precision voltage and current sourcing as well as measurement capabilities. In operation, it acts as a cur-

rent source to provide current to the outer probes and a voltage meter to measure voltage between the inner two probes. There are two modes of operations: manual and remote. In remote mode the instrument communicates with the LabView based software [84] through IEEE−488.2 GPIB communication protocol.
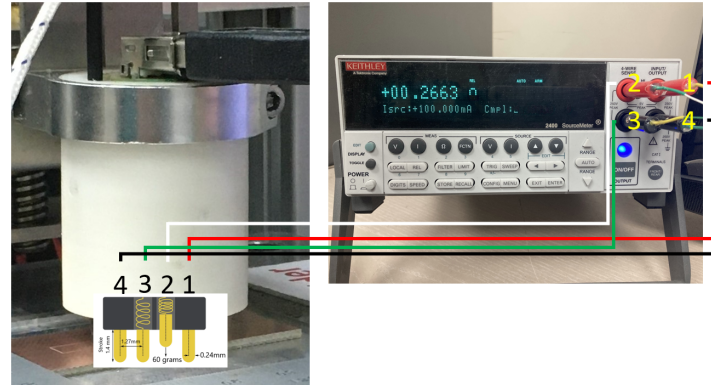
Figure 3.12: Photograph of the Keithley 2400 SMU with connection to 4−probe head.

3.2.1.5 Graphical User Interfaces (GUIs)

A labview based graphical user interface (GUI), as shown in Figure 3.13, is designed to control the four probe head movement.
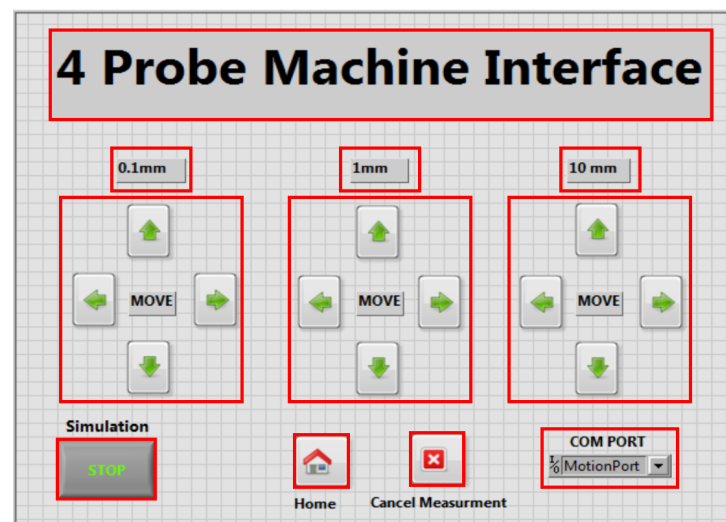
Figure 3.13: Screenshot of the GUI for probe head movement.

This GUI communicates with the motion controller, based on Arduino Mega micro-controller hardware, through a serial communication. Three levels of linear motion resolution can be achieved with this interface that is 10 mm, 1 mm and 0.1 mm. The home button brings the head at the reference position.

For the sheet resistance measurement, an open source GUI, as shown in Figure 3.14, is used [84]. This GUI works with Keithley 2400 source meter unit (SMU) to perform current voltage characterization of four point probe. The GUI communicates with
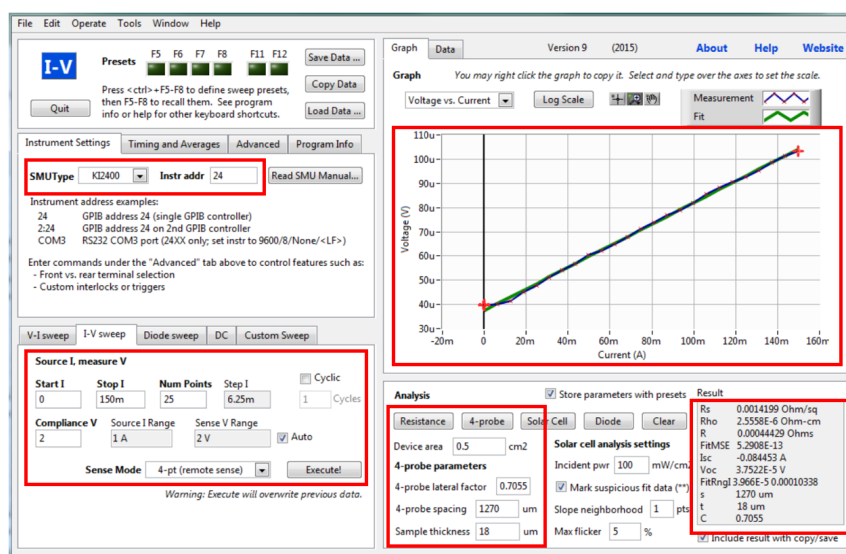
Figure 3.14: Screenshot of the GUI for sheet resistance measurement.

SMU through a GPIB adapter. An I-V sweep, sourcing current and measuring voltage, is selected for the measurement of sheet resistance. The parameters are set as follows:

1. Enter values for the sweep start and sweep stop.

2. Enter the number of points for the sweep.

3. Enter the compliance setting, which is a limit value to prevent excessive current (or voltage from being applied to the device under test.

4. Select the sense mode 4-pt (remote sense).

5. Select Auto-range to automatically switch to the lowest available measurement range at each point of the sweep.

After executing the measurement, the software plots the data points as Voltage vs. Current plot (I-V) curve. The software also provides data analysis tools for example

resistance and four probe. The resistance can be calculated after double clicking the resistance tab. It apples linear regression fit to the data and calculates resistance. Similarly 4 probe tab provides analysis for sheet resistance.

Figure 3.15 shows an I-V curve obtained after applying current to the out two pins and measure voltage between inner two pins of the dual axes four-point probe DA4PP. The slop of the curve gives resistance R (Ω) of the sample under test. The other properties such as sheet resistance R_{sh} (Ω/sq), resistivity ρ ($\Omega \cdot m$) and conductivity (σ) (S/m) are then derived from the resistance data. Table 3.7 shows electrical properties obtained from the I-V curve.
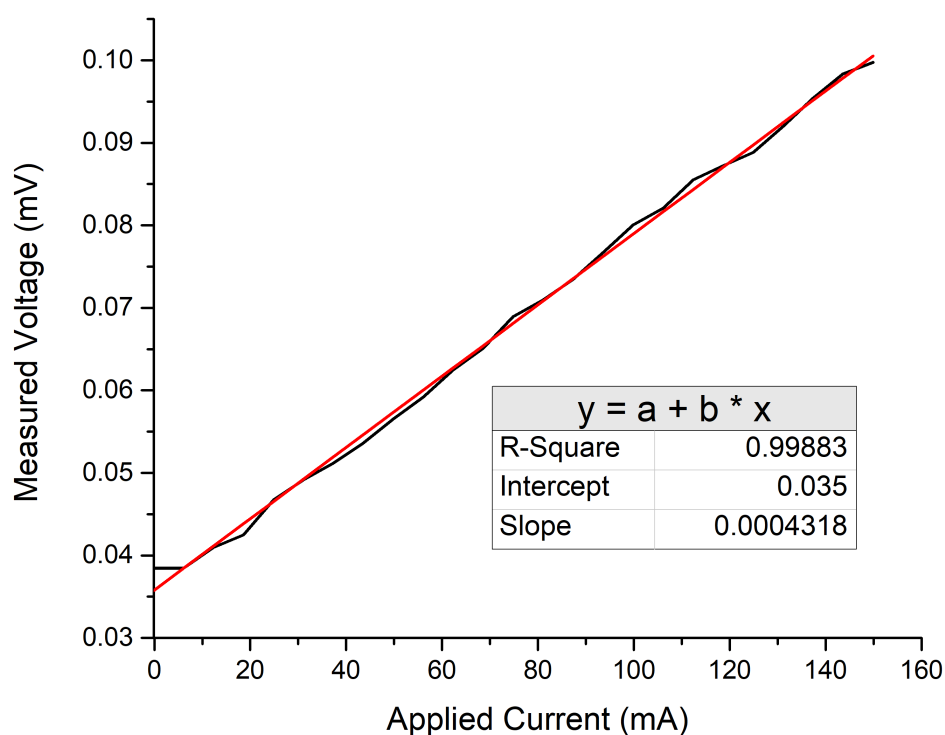
Figure 3.15: Plot of the I-V curve.

Table 3.7: Electrical properties obtained from the I−V curve.

Resistance	Sheet Resistance	Resistivity	Conductivity
(Ω)	(Ω/sq)	($\Omega \cdot m$)	(S/m)
4.318×10^{-4}	1.38×10^{-3}	2.486×10^{-08}	4.023×10^{07}

3.2.2   High Frequency Vibration Design

The developed high frequency vibration design system consists of:

- A signal generator

- An amplifier

- A digital frequency Counter

- A high frequency vibration test rig

- An FFT analyzer

- A PC with PULSE Labshop

Figure 3.16 shows a schematic layout of the experimental setup for high frequency vibrations. A signal generator module type 3107 (Brüel & Kjær) is used to generate
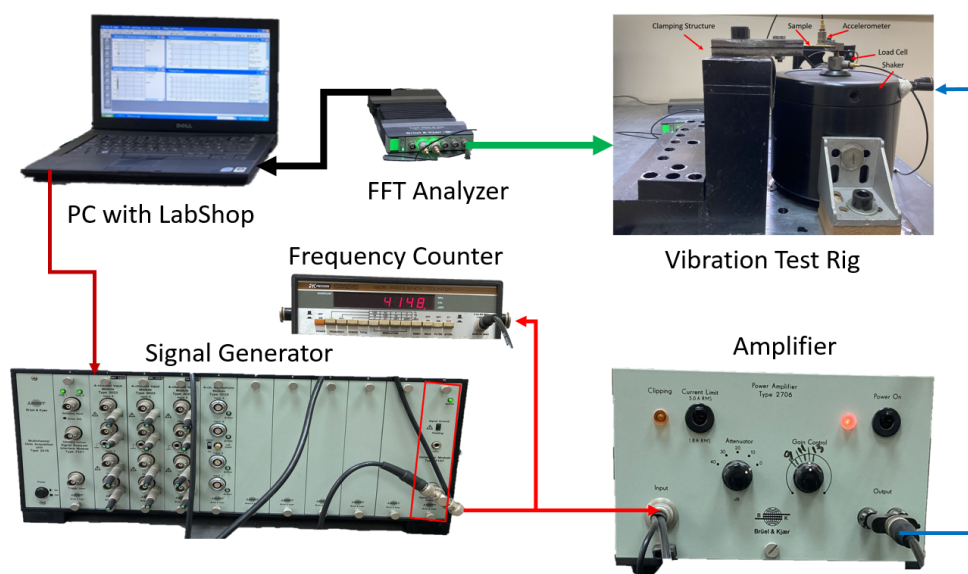
Figure 3.16: Schematic layout of the experimental setup.

continuous sinusoidal signals at 50 Hz frequency rate. The parameters for the signal generator are set by PULSE Labshop V4.0 as shown in Figure 3.17. A digital frequency counter type 1805 (B & K Precision) counts the required number of cycles for the experiment and a power amplifier type 2706 (Brüel & Kjær) amplifies the signals to be fed to the vibration tester type 4809 (Brüel & Kjær). The vibration data was captured using a LAN XI type 3050-A-060 (Brüel & Kjær) hardware

module. The data was then analyzed by PULSE LabShop V13.5.0 (Brüel & Kjær) to determine the vibration response of the transducers i.e., an accelerometer and a load cell.
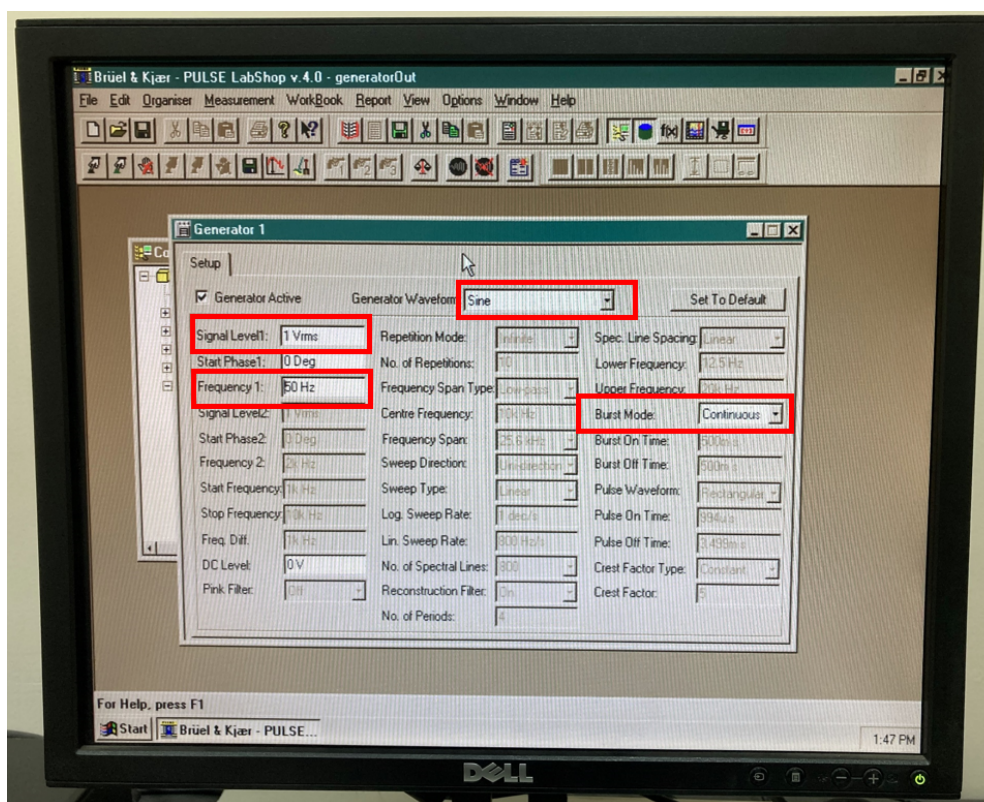
Figure 3.17: Screenshot of the parameters set for signal generator.

3.2.2.1   Vibration Test Rig

Figure 3.18 shows a photograph of the vibration test rig. It comprises of:

- A vibration exciter

- A load cell

- An accelerometer

- A rigid clamping structure

A bench-top vibration exciter type 4809 (Brüel & Kjær) is used in this study. It covers a wide range of frequency $(10 - 20\text{k})$ Hz and a continuous displacement of 8 mm peak-to-peak and can impart 45 N sinusoidal force or up to 60 N with

assisted cooling. A 75 VA Power Amplifier Type 2706 (Brüel & Kjær) is used to drive this vibration exciter. A load cell or force transducer type 8230 (Brüel & Kjær) is mounted above the shaker to recode the applied forces to the specimen. The one side of the specimen is mounted on the rigid structure while the other end is connected to the load cell by means of a small clamping steel structure. An
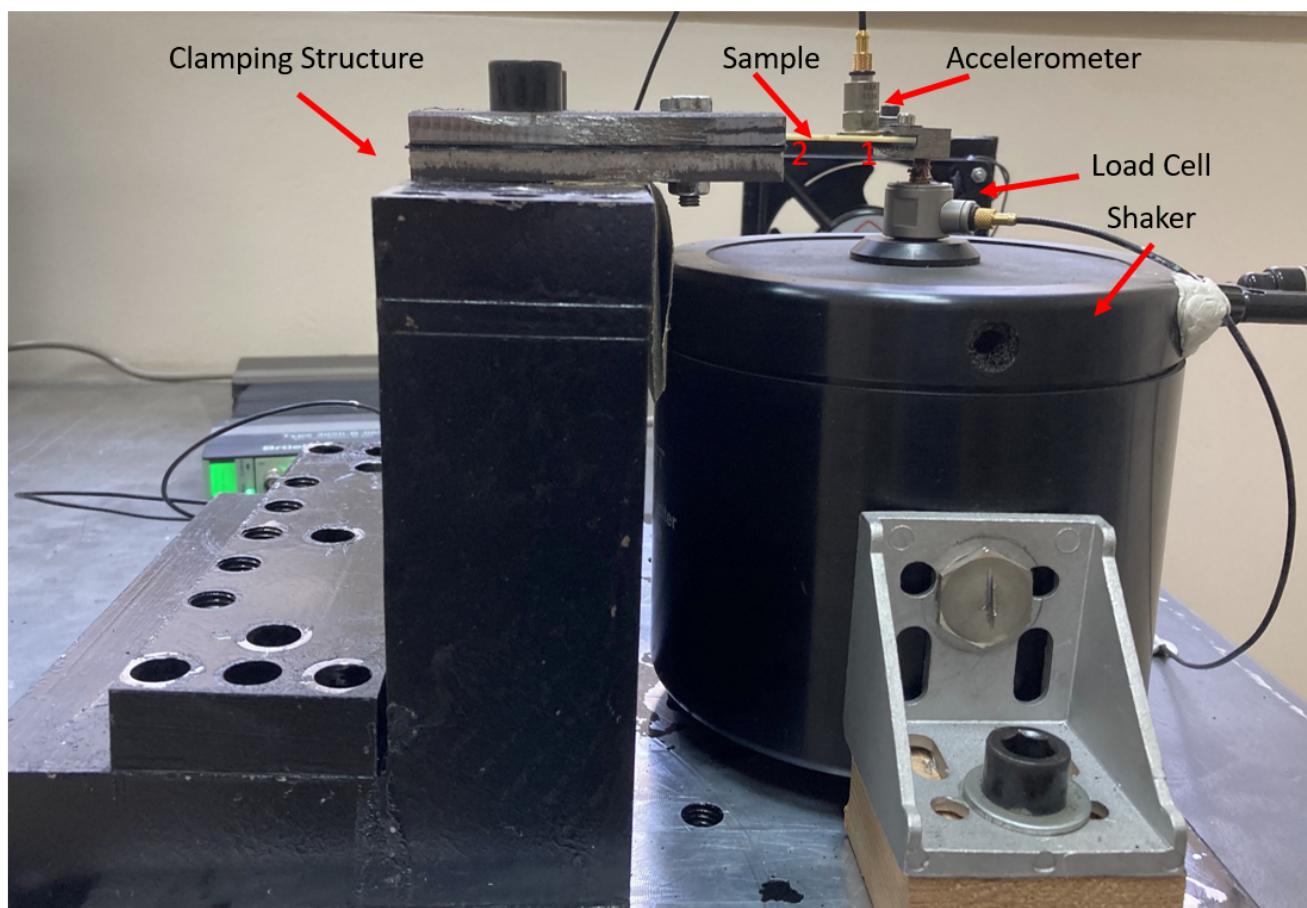
Figure 3.18: Photograph of the vibration test rig. The positions (a) and (b) in red indicate the accelerometer positions.

accelerometer type 4526 (Brüel & Kjær) is used to record amplitude of vibrations at positions (a) and (b). Figure 3.19 shows typical response of the force sensor. An amplitude of force can be seen in the plot of Figure (3.19 (b)). The high amplitude at 50 Hz frequency confirms the shaker input frequency of 50 Hz. The accelerometer response in the frequency domain at positions (a) and (b) can be seen in Figure 3.20. The vibration and stress amplitudes at positions (a) and (b) are also modeled by FEM using ANSYSV19.3 workbench with Mechanical APDL solver using a fixed end (cantilever) as boundary condition as shown in Figure 3.21. A mesh size of 1 mm of the shell element SOLSH190 was used for FEM modeling. The number of nodes and mesh elements were 26895 and 4146 respectively. Both the FEM model (3.21 (a)) and accelerometer plot (3.20 (b)) show less vibration but more stress amplitude

at position 2.
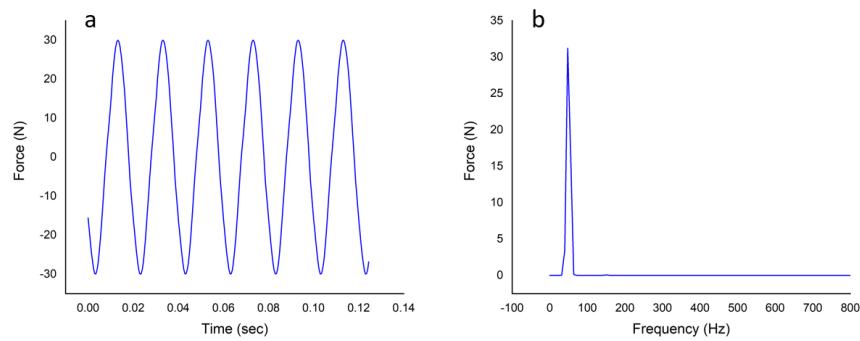
Figure 3.19: Plot of the force sensor (load cell): (a) in the time domain; (b) in the frequency domain.
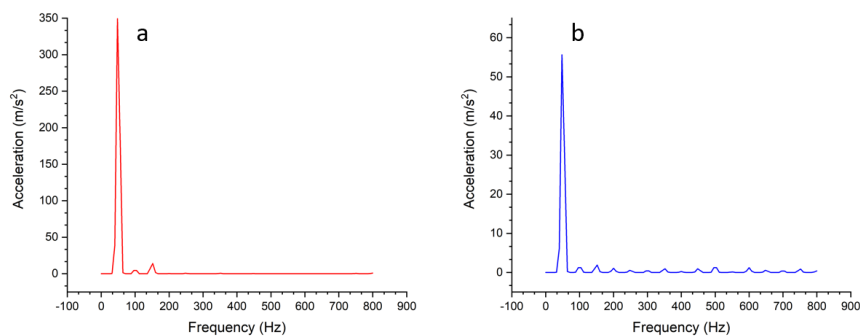
Figure 3.20: Frequency response of the accelerometer: (a) at position (1); (b) at position (2)
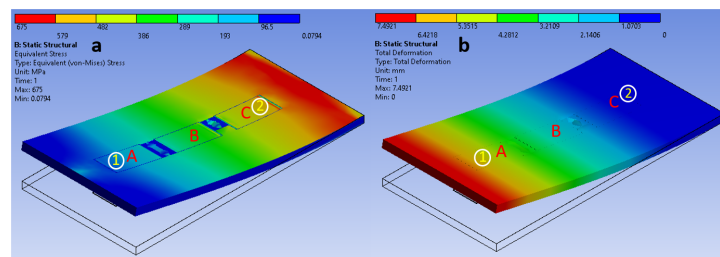
Figure 3.21: Examples of specimen models used for FEM analysis; (a) stress amplitude at positions (1) and (2); (b) deformation at positions (1) and (2).

3.3   Surface Analysis

The surface of the samples was examined by Environmental Scanning Electron Microscopy (ESEM) and contact angle measurements. ESEM images were recorded in a Quanta 600 microscope (FEI Company, Inc.) under high vacuum at 25 kV in the back-scattered mode. The samples were cleaned with a cloth embedded in acetone and dried under a nitrogen stream before analysis and probed at a 10 mm working distance at 50X, 500X and 3000X magnification. The elemental composition was measured at the 3000X magnification using the same instrument in XDS mode.

The contact angles were measured at different locations of the samples as shown in Figure 3.22. The static drop method, using an OCA 15 plus goniometer (Neurtek Instruments) with an image resolution of 752x582 pixels and $\pm$ 0.1^0 accuracy, was used for this test. The drop volume was 10 µL, and measurements were performed in a controlled temperature 24^0C and ambient humidity 55 %.
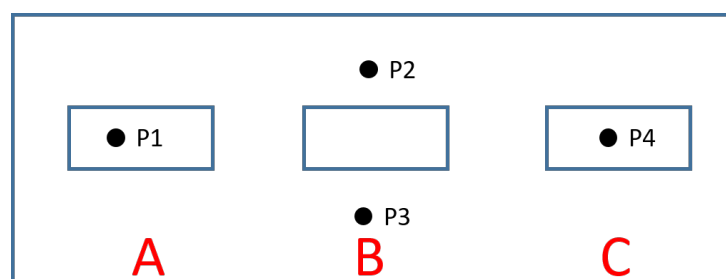
Figure 3.22: Water drop locations for contact angle measurements

Chapter 4

Experimental and Numerical Simulation Study of the Vibration Properties of Thin Copper Films Bonded to FR4 Composite

This chapter[1] gives details of the results for vibration characteristics of thin copper films bounded to FR-4 epoxy laminate using modal analysis. The experimental and FEM results are discussed in details in this chapter.

4.1   Modal Analysis

4.1.1   Frequency spectra and mode shapes

The values of the natural frequencies in terms of auto spectrum analysis were obtained from the PULSE program by applying FRFs, as shown in Figure 4.1. In this waterfall plot of frequency versus amplitude, the first peak represents the values of

---

[1]Part of this chapter has been published in [64]
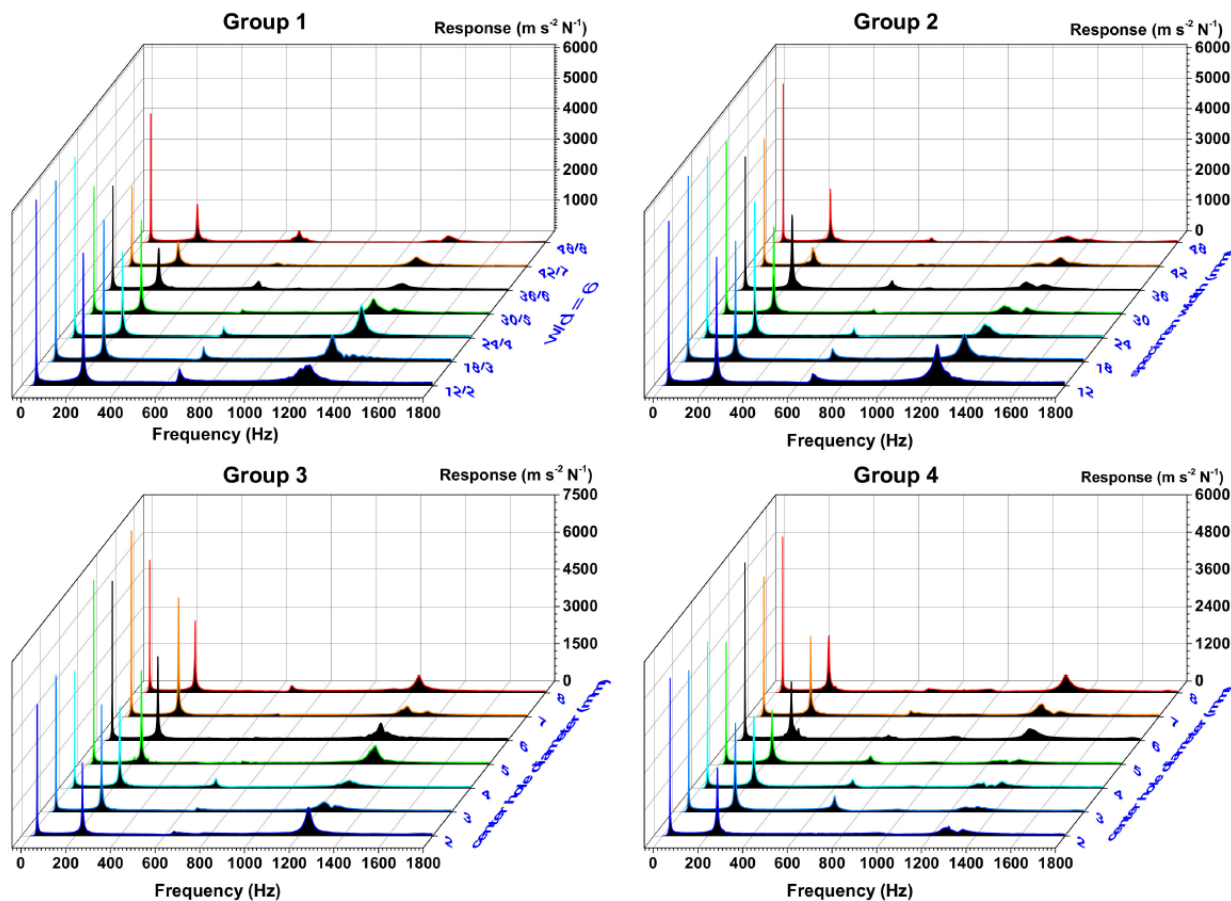
Figure 4.1: Auto spectrum analysis for all groups of samples.

the natural frequencies of the different specimens in each group. At mode 1 (first natural frequency), all of the specimen groups show high amplitudes of vibration. The frequency range of 400 Hz to 1k Hz shows a small resonance in all the samples. The extraction of modal parameters such as natural frequencies and damping ratios from FRF data was done by using the peak amplitude method [65]. The predicted mode shapes were obtained by ANSYS. Figures 4.2 and 4.3 show the results for 24 mm width samples with and without a central 4 mm hole, respectively. Similarly, Figures 4.4 and 4.5 show the results for 24 and 30 mm width samples with 8 mm central holes, respectively.

In general, all samples have similar mode shapes with no obvious influence of the hole. This is expected for exciting vibrations of low amplitudes and samples prepared with the same material. For mode 2, the maximum deflection is observed around the center of the samples. At mode 1 (first natural frequency), all of the specimen groups show high amplitudes of vibration. In all cases, the mode shape around 650 Hz presented the lowest amplitude of all modes. This mode presents an area of very low deflection very close to the position of the accelerometer (20 mm from the
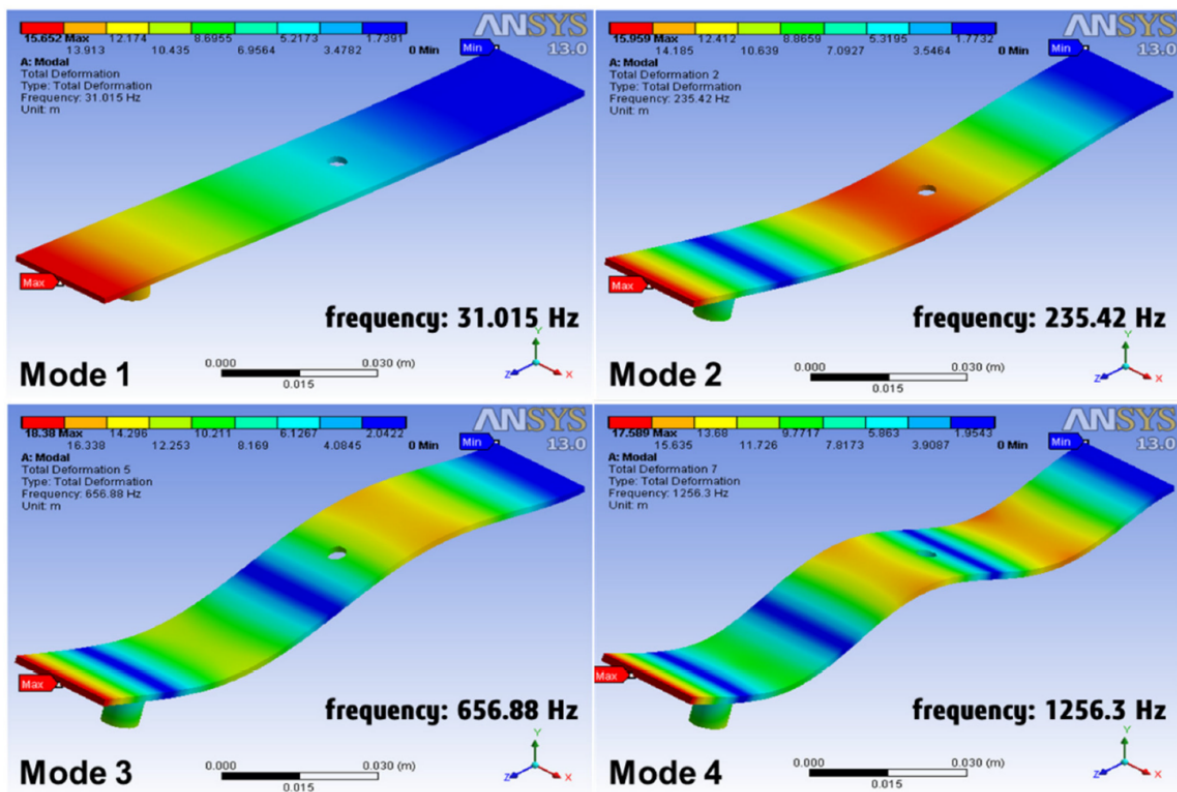
Figure 4.2: Mode shapes for a single specimen (width 24 mm, center hole 4 mm) in Group 1.
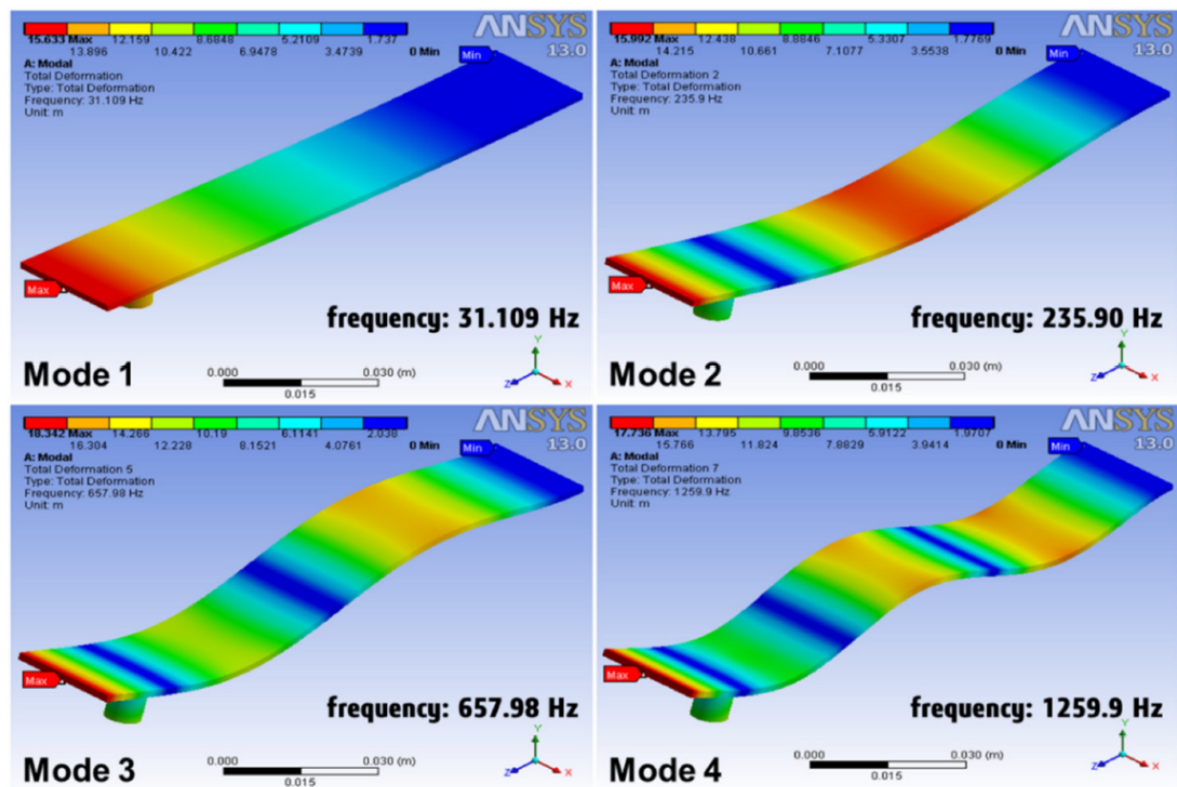
Figure 4.3: Mode shapes for a single specimen (width 24 mm) in Group 2.
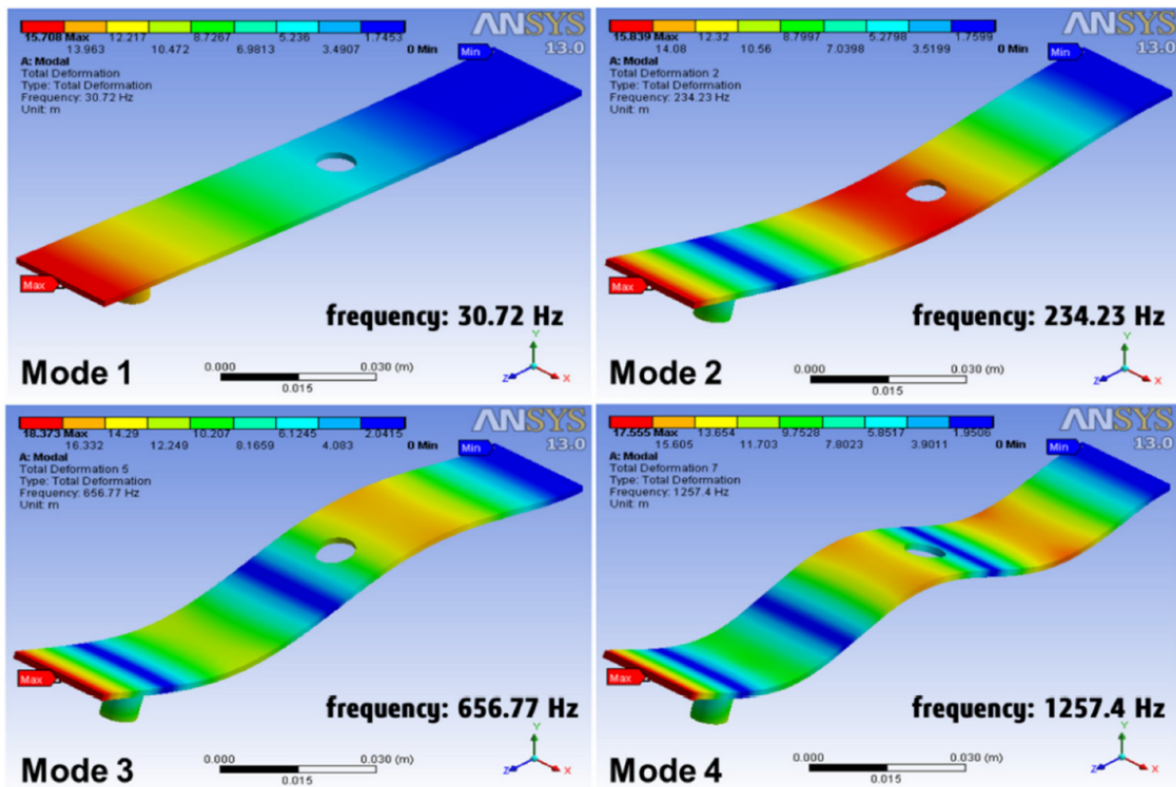
Figure 4.4: Mode shapes for a single specimen (width 24 mm, center hole 8 mm) in Group 3.
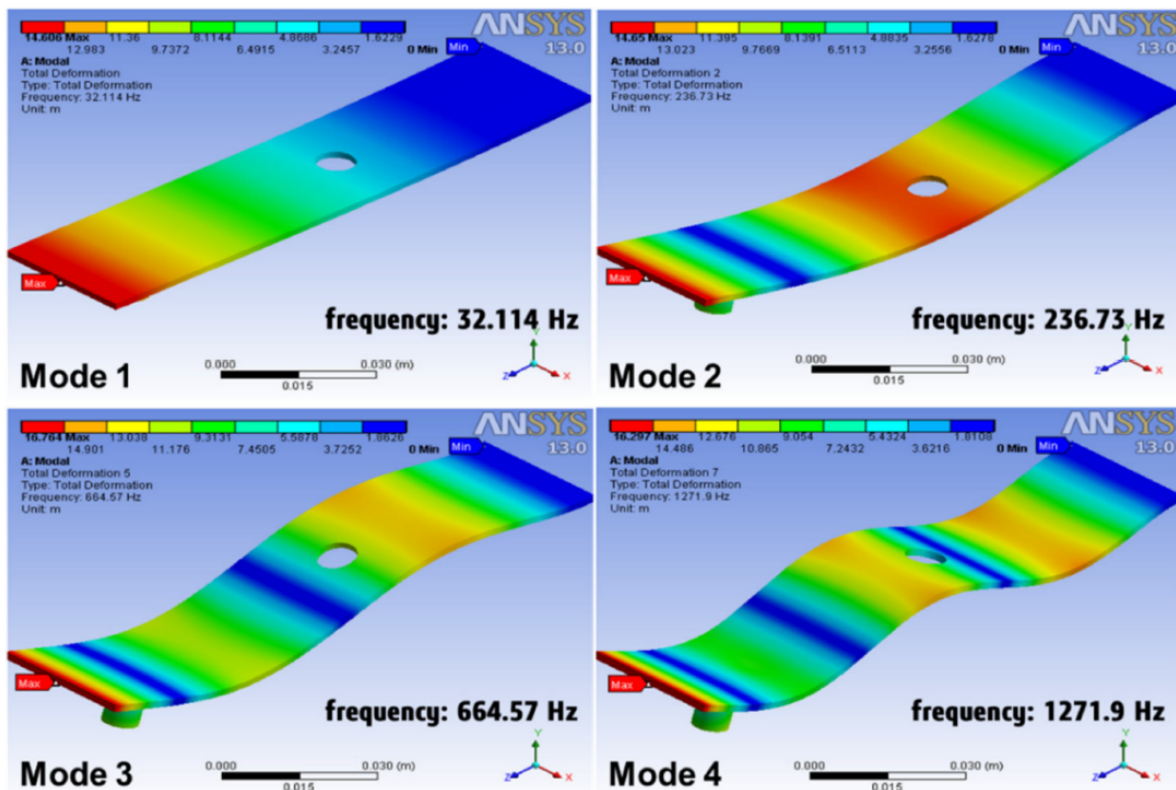
Figure 4.5: Mode shapes for a single specimen (width 30 mm, center hole 8 mm) in Group 4.

free end of the cantilever), which also coincides with one of the impact points. This canceling effect is not present in modes 1 and 2 and is attenuated in mode 4 where deflection is minimal 5 mm below the accelerometer.

4.1.2   Natural frequencies and damping ratios

Figures 4.6 and 4.7 show the variations in the first four natural frequencies and their corresponding damping ratios for all the specimens in the different groups, respectively. The fundamental natural frequency of Group 1 (with central hole) is
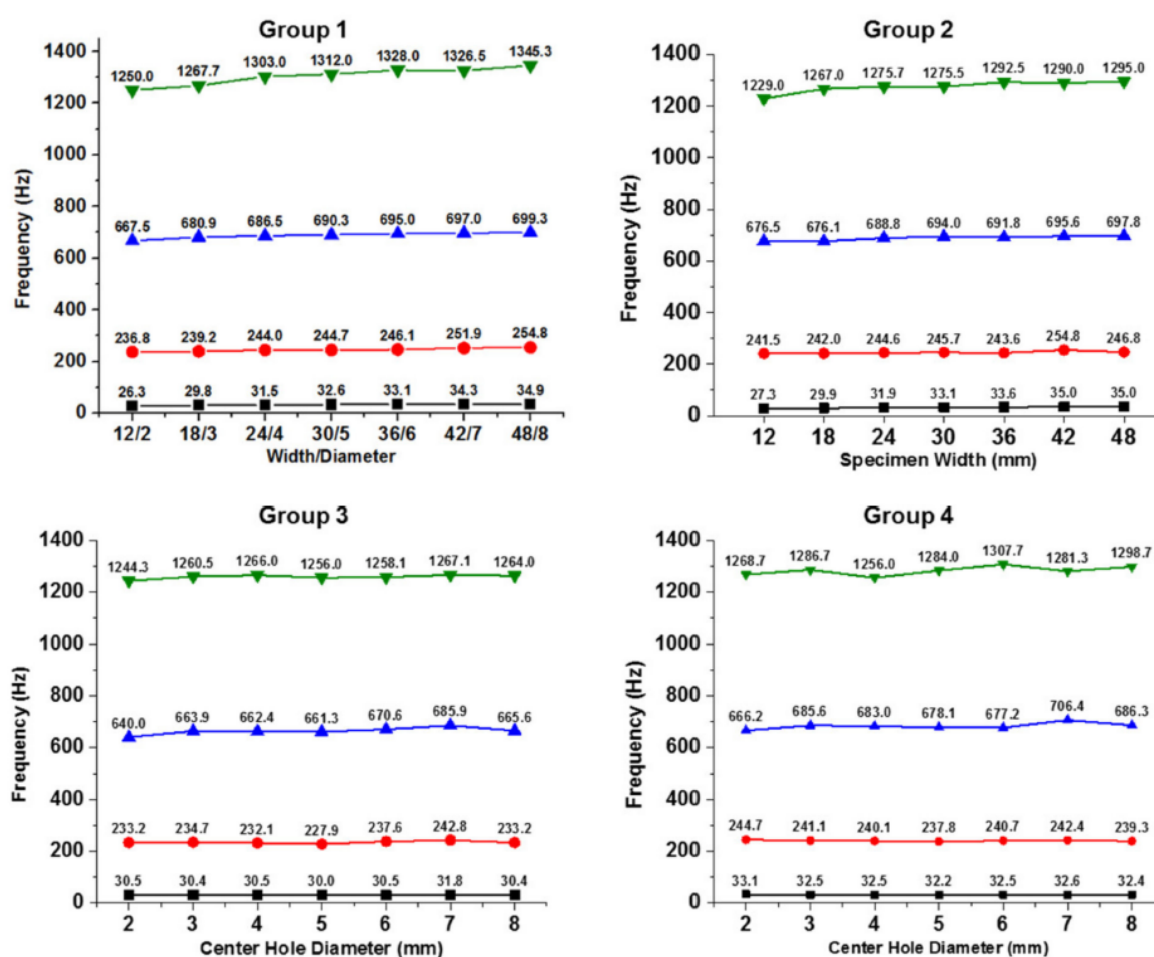
Figure 4.6: Natural frequency plots for all specimen groups and frequency modes.
Mode 1 ■ , mode 2 ●, mode 3 ▲ and mode 4 ▼.

slightly lower than for Group 2 (no central hole) for all the samples, but Group 1 shows a slightly higher damping due to the presence of the center holes in the middle of the specimens. In both groups, a frequency increase is observed as the specimen width also increases. This indicates that the W/D aspect ratio does not play a

significant role and the modal behavior is governed by specimen stiffness and mass in spite of the fact that the size effect reduces nominal strength up to 15 % [19]. Interestingly, the change in center-hole diameter at constant width in Groups 3 and
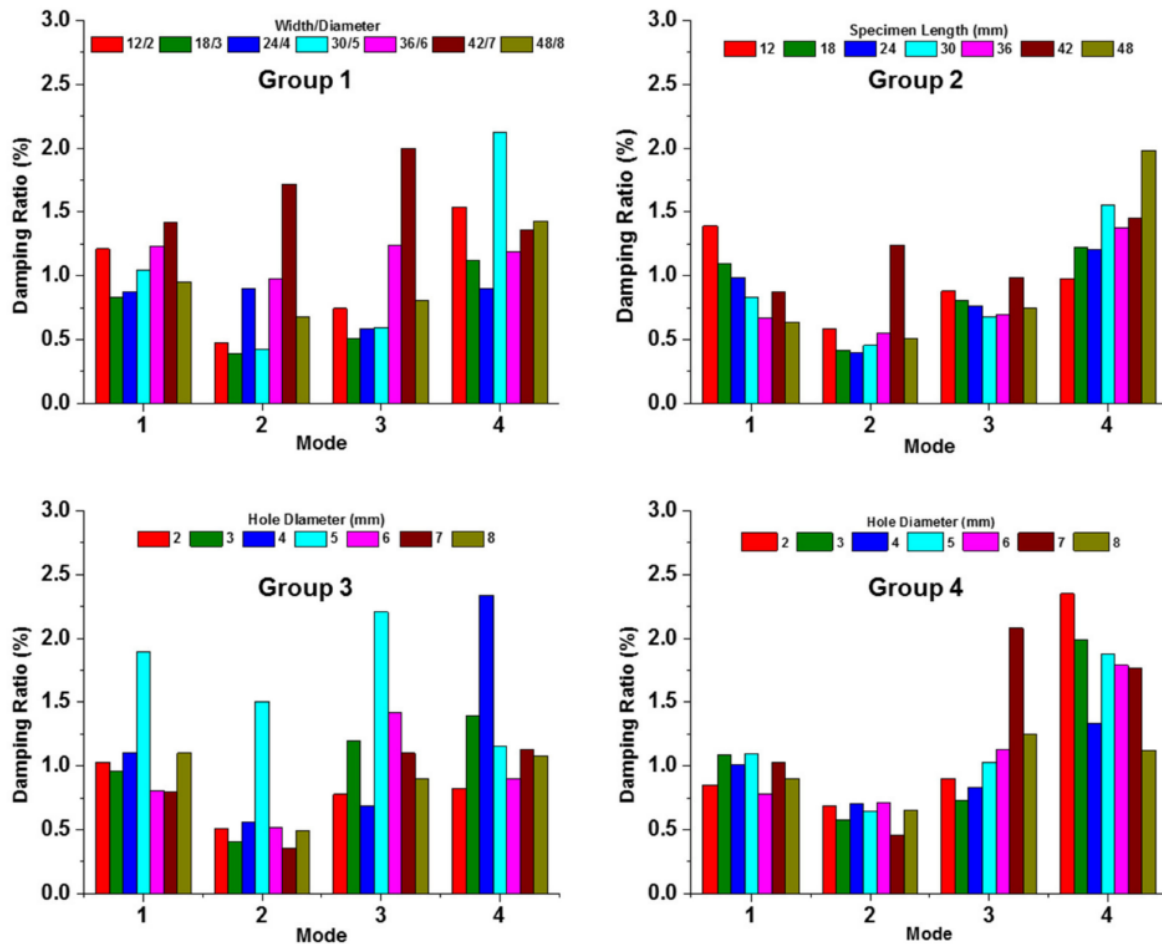
Figure 4.7: Damping ratio plots for all specimen groups and frequency modes.

4 shows a very little difference in frequency for mode 1 in all the specimens. The vibration mode 4 in all the groups show high damping values as compared to other modes because high frequencies exhibit low vibration amplitudes. This behavior can also be seen in the waterfall plot that shows low vibration amplitudes in this mode.

4.1.3 Comparison of results with a theoretical model

For the comparison of extracted experimental natural frequencies, a uniform composite cantilever beam of 24 mm width was first modeled mathematically, and the results were then used for the finite element modeling using ANSYS V13.0. Figure 4.8 shows a comparison of the experimental natural frequencies for all the specimens

with the calculated value by the finite element method. As can be seen, there is a very good correspondence between the values, especially for Groups 3 and 4, while the calculation predicts slightly lower values (between 2 and 4 %) for the high frequency modes of Groups 1 and 2. As an example of validity of the selected model,
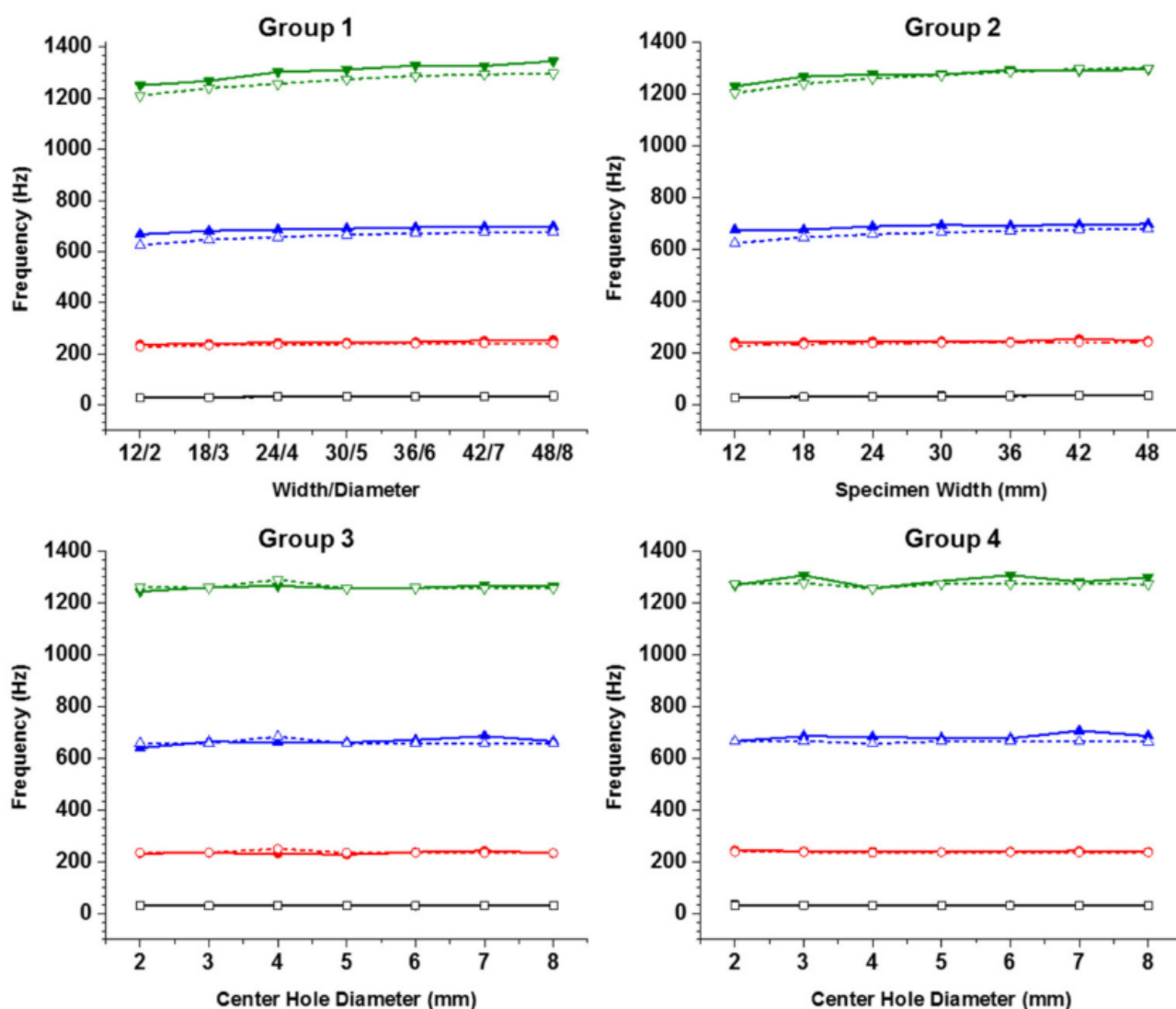
Figure 4.8: Comparison of experimental (closed symbols, solid line) and analytical (open symbols, dotted line) frequencies for all the specimens.

Table 4.1 shows a comparison of the modeled frequency with experimental and FEM results for sample 3 of Groups 1 and 2 and sample 6 of Group 3, i.e. samples 24 mm width with and without central holes. Similarly, Table 4.2 shows the results calculated for a 48 mm cantilever plate and compared with sample 7 of Groups 1 and 2 (48 mm width with and without central hole). The correlated mode pairs (CMPs) were plotted to check the degree of correlation between the two sets of results for a single specimen in each group (sample 3), as shown in Figure 4.9. The two sets

Table 4.1: Comparison of the natural frequency of a uniform composite rectangular cantilever beam (24 mm width) with experimental and FEM results of samples of the same width.

| Mode | Natural Frequency (Hz) | | | | | | |
| | W=24 mm No Hole | | W=24 mm D=4 mm | | W=24 mm D=8 mm | | Model $(Beam)^3$ |
	$Exp.^1$	FEM^2	$Exp.^1$	FEM^2	$Exp.^1$	FEM^2	
1	31.9	31.1	31.5	31.0	30.4	30.7	36.6
2	244.6	235.9	244.0	235.4	233.2	234.2	229.3
3	688.0	658.0	686.5	656.9	665.6	656.7	641.5
4	1275.7	1259.9	1303.0	1256.3	1264.0	1257.4	1254.2

[1] Exp.: experimental; [2] FEM: calculated by ANSYS; [3] Model: calculated for a cantilever beam.

Table 4.2: Comparison of the natural frequency of a uniform composite rectangular cantilever plate (48 mm width) with experimental and FEM results of samples of the same width.

| Mode | Natural Frequency (Hz) | | | | |
| | W=48 mm No Hole | | W=48 mm D=8 mm | | Model $(Plate)^3$ |
	$Exp.^1$	FEM^2	$Exp.^1$	FEM^2	
1	35.0	34.8	34.9	34.6	38.0
2	246.8	241.7	254.8	240.9	238.2
3	697.8	678.6	699.3	677.5	666.4
4	1295.0	1300.4	1345.3	1297.6	1302.9

[1] Exp.: experimental; [2] FEM: calculated by ANSYS; [3] Model: calculated for a cantilever plate.

of data show a high degree of correlation since the points lie near or close to the straight line of slope equal to 1. To assess the difference of the natural frequencies among all possible combinations of experimental and analytical model modes, the predicted and measured natural frequencies were also used to calculate the Natural Frequency Difference (NFD) value [83]. Figure 4.10 shows the 3−dimensional NFD diagram of a single specimen (sample 3) in each group. Small values in the main diagonal positions and large NFD values in non-diagonal positions show that there is high compatibility between the two sets of results, as observed for the samples depicted in Figure 4.10.
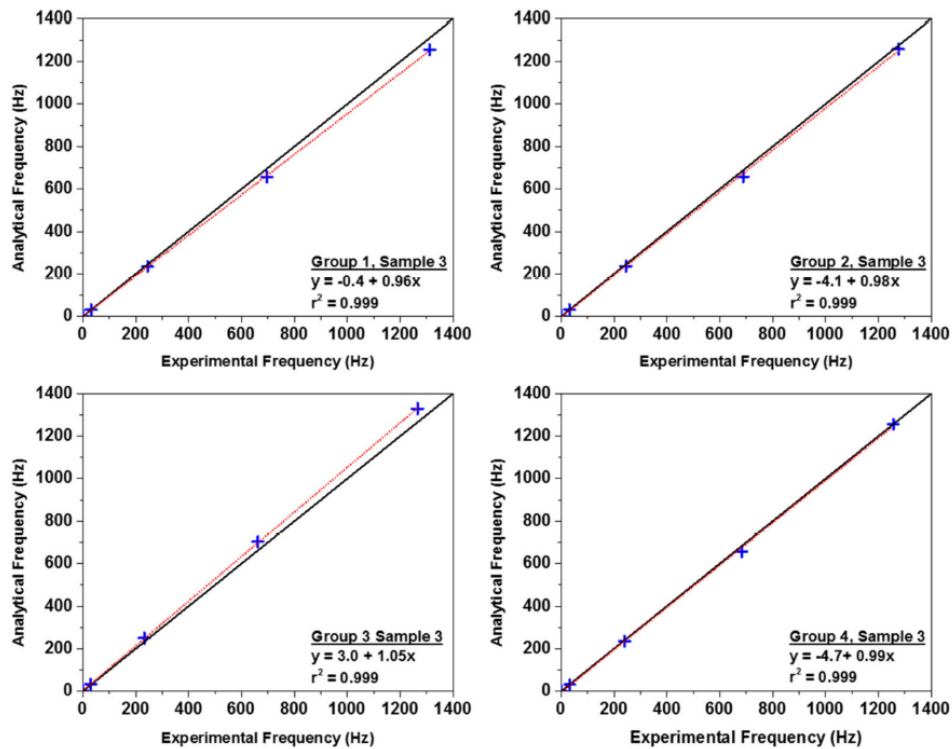
Figure 4.9: Correlated mode pairs for sample 3 of all groups. The black diagonal line represents a slope equal to 1.
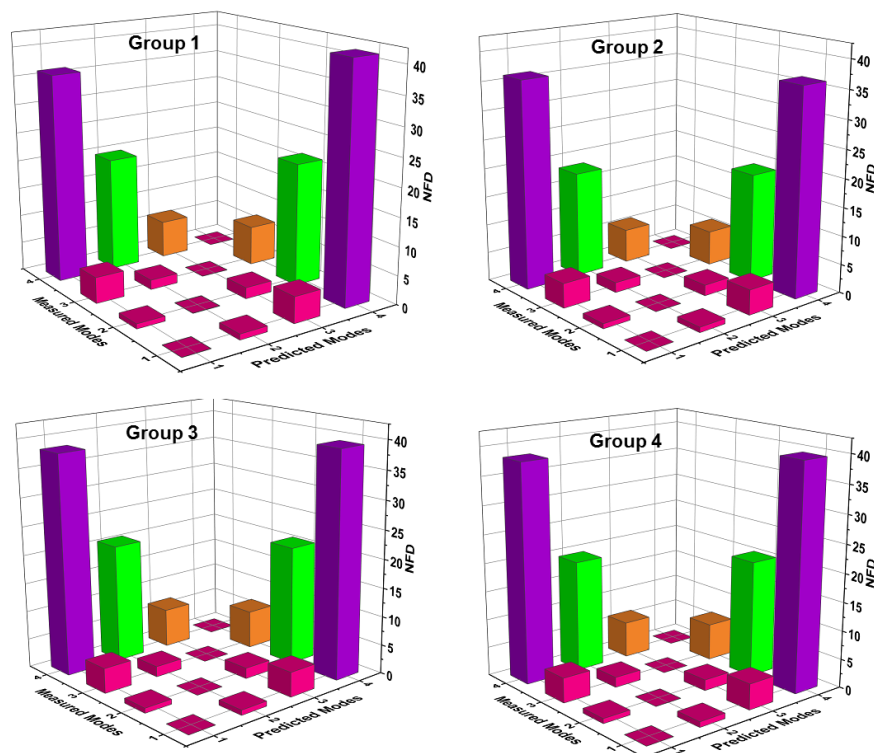

Figure 4.10: Natural frequency difference diagrams for sample 3 of all groups.

4.1.4   Normalized frequency shift calculations

The values of the normalized frequency shift [85] for sample 1 in each group with respect to the rest of the samples of the same group are presented in Figure 4.11. Due to the geometrical variations and high amplitude of vibrations, there is up to 33 % frequency change in Group 1 for mode 1, while the other modes show a small frequency shift between the first and the rest of the samples. A similar behavior of
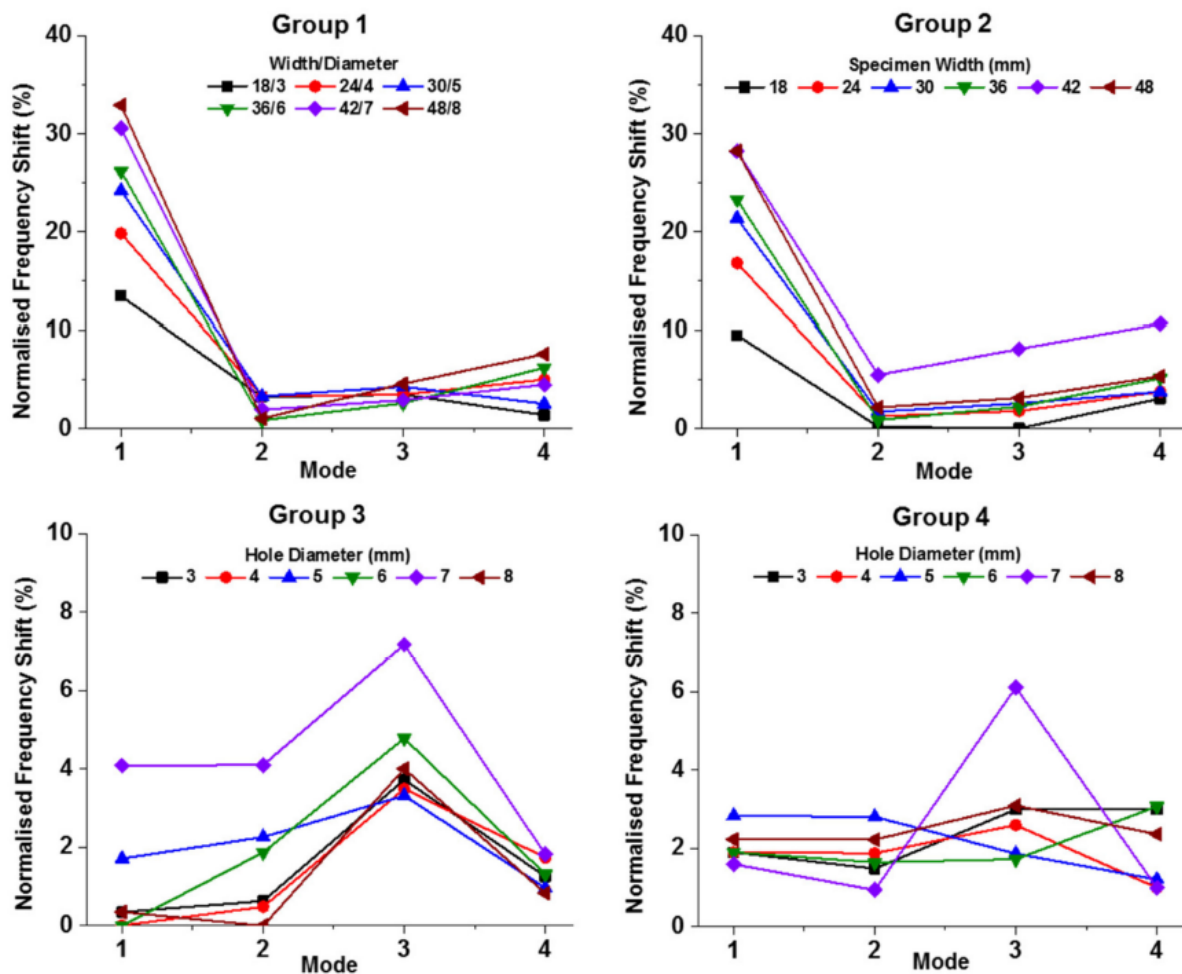
Figure 4.11: Normalized frequency shifts for samples 2-7 of all groups.

frequency change is seen in Group 2, although the maximum frequency shift is less than 30 %. The frequency change between the 2 mm center hole sample and the rest of the samples in groups 3 and 4 is very little as compared to the change due to aspect ratio (width/diameter), as in groups 1 and 2. This further indicates that in groups 3 and 4, sample mass is the dominating factor in the frequency changes.

4.2   Preliminary conclusions

In this chapter, the vibrational characteristics, such as natural frequencies and damping ratios, of thin copper films of thickness 35 μm bounded to FR4 epoxy laminate of 1.5 mm thick were determined experimentally and analytically using a finite element method. Four groups of samples were selected in order to study geometric effects and the presence of a central hole of different diameters. It has been found that the chosen samples are suitable to be used as PCBs that undergo significant frequency changes ranging from 40 Hz to 1k Hz. The natural frequency of all the specimens was found to be less than 40 Hz and the influence of a central hole was not significant to affect the modal properties.

In order to study the possible damage mechanisms that undergo these materials and how they affect their performance, the influence of high cycle vibration fatigue on their electrical properties, with and without thermal variations will be discussed in the following chapter.

Chapter 5

Variation of Electrical Properties under Different Loading Cycles and Temperatures

This chapter describes, the effect of mechanical vibrations on the electrical performance of thin copper films. A custom made four probe head was used to apply current to the outer probes and measure voltage through the inner probes as described before in Figure 1.15. The effect of mechanical cycles and thermal loading on the electrical properties such as resistance (R) Ω, sheet resistance (R_{sh}) Ω/sq, resistivity (ρ) $\Omega \cdot m$, and electrical conductivity (σ) S/m, the reciprocal of resistivity, were determined.

5.1   Validation and Repeatability

In order to validate the device performance, a set of ITO samples, which are: OS-SILA glass substrates coated with a 100 nm layer of Indium Tin Oxide (ITO) [86], were validated using DA4PP. The reference sample was 20x15 mm having sheet resistance (14-16) Ω/sq. The measurement results from the custom made dual axes four−point probe (DA4PP) are then compared to the results obtained from the

commercial four−point probe system (Ossila Four-Point Probe System.) [86]. The results obtained are in good agreement as shown in Figure 5.1. The average sheet resistance value R_{sh} obtained by DA4PP is 14.75 Ω/sq as compared with Ossila reference sample value of 14.36 Ω/sq. The comparison between the theoretical (cal-
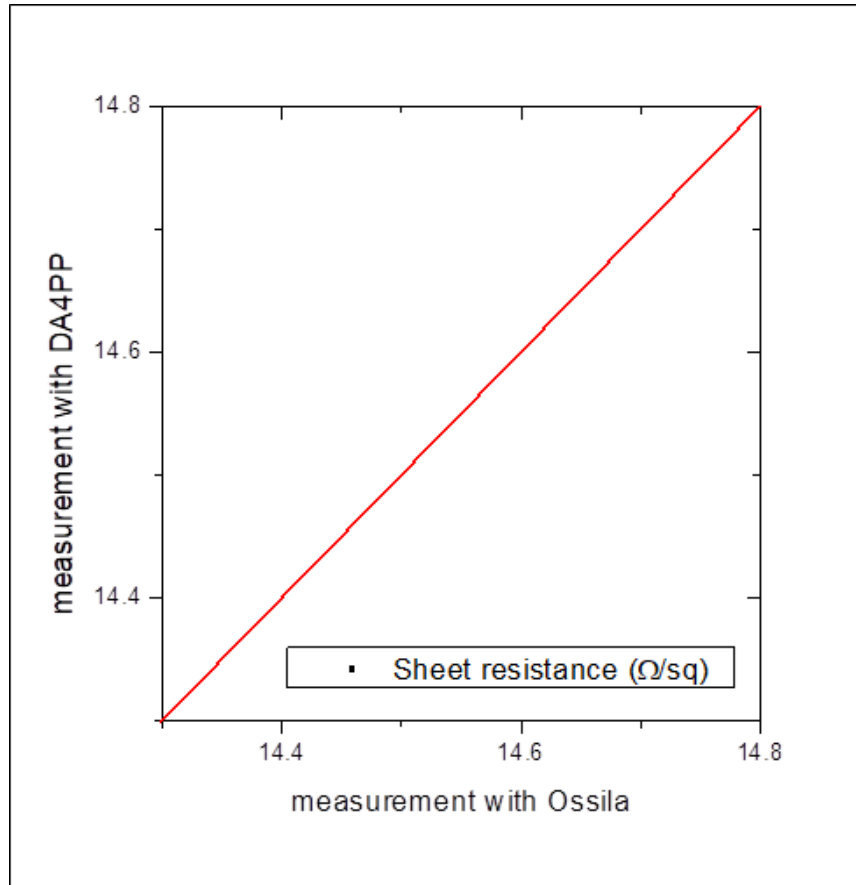
Figure 5.1: Comparison of the Sheet resistance values measured by two devices.

culated) and measured resistance can be seen in Table 5.1. The measurement results show a good correlation at 45^0C with 4.21 % error.The maximum difference of 7.46 % is at 25^0C. Figure 5.2 shows an error plot at different temperatures. The theoretical calculations were performed by using the following equation for resistance with temperature coefficient at 20^0C [87]:

$$R = \rho_{20} \cdot \frac{L}{T \cdot W} \cdot [1 + \alpha\, (T_{20} - T)] \qquad [\Omega]^{1} \qquad (5.1)$$

Where ρ_{20} is the copper resistivity at 20^0C (1.67x$10^{-8}\Omega$·m), L is the length of the copper trace in mm, W is the width of the copper trace in mm, T is the thickness of the copper trace in μm, and α is the Temperature coefficient at 20^0C (3.93x$10^{-3}\Omega/\Omega/C$). The dual axes four point probe (DA4PP) performance is quan-

---

[1]Ohm

Table 5.1: Comparison of the theoretical and experimental resistance values.

Resistance (Ω)						
Temperature (C^0)	Length (mm)	Width (mm)	Thickness (μm)	R_{th}^* (Ω)	$R_{exp}^{\pm}$ (Ω)	Difference %
25				4.638×10^{-4}	4.317×10^{-4}	7.46
35	5	10	18	4.821×10^{-4}	4.559×10^{-4}	5.74
45				5.003×10^{-4}	4.801×10^{-4}	4.21

* R_{th}: theoretical resistance; $\pm$ R_{exp}: experimental resistance.
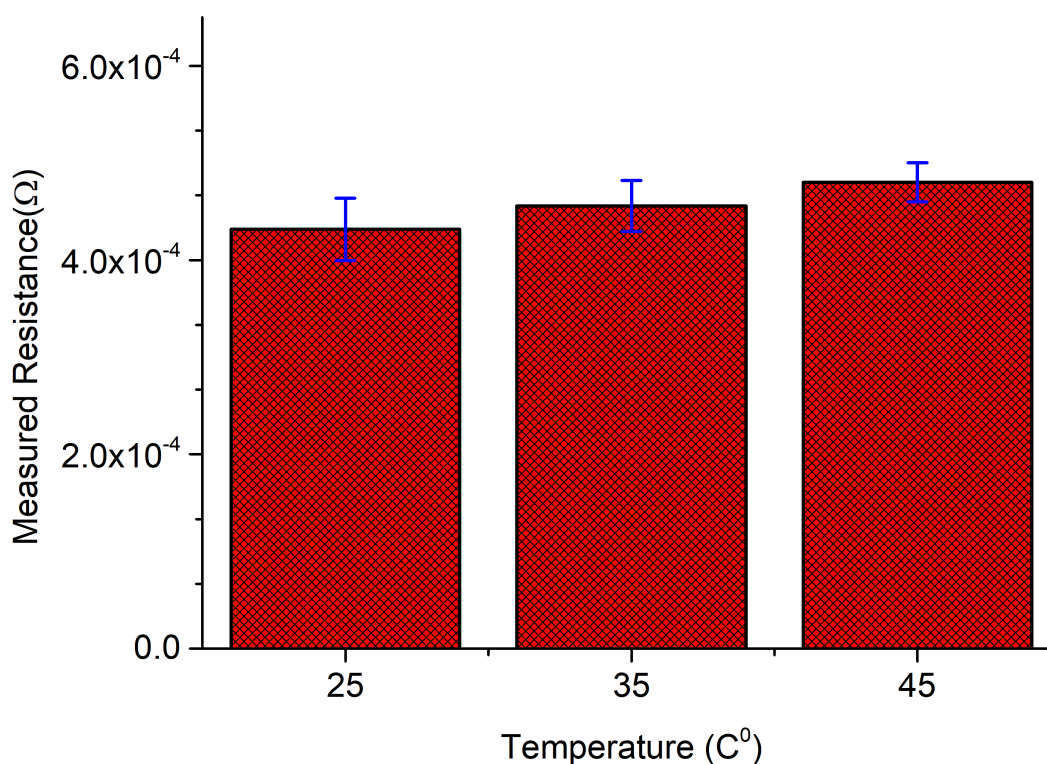
Figure 5.2: Difference plot with measured resistance values.

tified by measuring resistance of different samples at different temperatures and mechanical cycles by finding standard deviation SD and coefficient of variation CV. Tables [5.2 − 5.5] show resistance values of three samples at varying input parameters for three measurement zones. The maximum variation in the data values is in zone B at 800k cycles and 45^0C. The coefficient of variation for this zone is 3.251 %. Interestingly, the similar behavior can be seen in other cases for zone B.

Table 5.2: Resistance variations before cyclic loading at 25^0C.

Resistance (Ω)								
Zone (A)			**Zone** (B)			**Zone** (C)		
Sample **Resistance**	SD^1	CV^2	**Resistance**	SD^1	CV^2	**Resistance**	SD^1	CV^2
(Ω)	(Ω)	%	(Ω)	(Ω)	%	(Ω)	(Ω)	%
1	4.217×10^{-4}			4.233×10^{-3}			4.589×10^{-4}		
2	4.206×10^{-4}	2.440×10^{-6}	0.581	4.151×10^{-4}	3.922×10^{-6}	0.938	4.591×10^{-4}	1.034×10^{-6}	0.225
3	4.161×10^{-4}			4.148×10^{-4}			4.568×10^{-4}		

[1] SD: standard deviation; [2] CV: coefficient of variation.

The results indicate that the custom-made DA4PP probe measures accurately the sample resistance is all regions and can be used to measure the resistance changes after mechanical and thermal loading as will be discussed in the next sections.

Table 5.3: Resistance variations after 800k cycles at 25^0C.

Resistance (Ω)								
Zone (A)			**Zone** (B)			**Zone** (C)		
Sample **Resistance**	SD^1	CV^2	**Resistance**	SD^1	CV^2	**Resistance**	SD^1	CV^2
(Ω)	(Ω)	%	(Ω)	(Ω)	%	(Ω)	(Ω)	%
1	1.905×10^{-3}			1.961×10^{-3}			3.432×10^{-2}		
2	1.903×10^{-3}	1.092×10^{-5}	0.575	1.903×10^{-3}	5.444×10^{-5}	2.869	3.434×10^{-2}	6.001×10^{-5}	0.175
3	1.881×10^{-3}			1.828×10^{-3}			3.420×10^{-2}		

[1] SD: standard deviation; [2] CV: coefficient of variation.

Table 5.4: Resistance variations before cyclic loading at 45^0C.

Sample	Resistance (Ω)	SD[1] (Ω)	CV[2] %	Resistance (Ω)	SD[1] (Ω)	CV[2] %	Resistance (Ω)	SD^1 (Ω)	CV[2] %
	Zone (A)			**Zone** (B)			**Zone** (C)		
1	$4.636\text{x}10^{-4}$			$4.744\text{x}10^{-4}$			$4.653\text{x}10^{-4}$		
2	$4.622\text{x}10^{-4}$	$4.425\text{x}10^{-6}$	0.962	$4.554\text{x}10^{-4}$	$8.504\text{x}10^{-6}$	1.838	$4.519\text{x}10^{-4}$	$5.580\text{x}10^{-6}$	1.218
3	$4.536\text{x}10^{-4}$			$4.575\text{x}10^{-4}$			$4.562\text{x}10^{-4}$		

[1] SD: standard deviation; [2] CV: coefficient of variation.

Table 5.5: Resistance variations after 800k cycles at 45^0C.

Sample	Resistance (Ω)	SD[1] (Ω)	CV[2] %	Resistance (Ω)	SD[1] (Ω)	CV[2] %	Resistance (Ω)	SD^1 (Ω)	CV[2] %
	Zone (A)			**Zone** (B)			**Zone** (C)		
1	$2.091\text{x}10^{-3}$			$2.15308x10^{-3}$			$3.543\text{x}10^{-2}$		
2	$2.109\text{x}10^{-3}$	$1.229\text{x}10^{-5}$	0.583	$2.062\text{x}10^{-3}$	$6.723\text{x}10^{-5}$	3.251	$3.668\text{x}10^{-2}$	$8.294\text{x}10^{-4}$	2.271
3	$2.120\text{x}10^{-3}$			$1.988\text{x}10^{-3}$			$3.74472x10^{-2}$		

[1] SD: standard deviation; [2] CV: coefficient of variation.

5.2 Change in Resistance under Mechanical and Thermal Loading

In general, four point probe method is used to determine sheet resistance of thin metal films, but in fact resistance is the main electrical property which is obtained by using this technique. In four probe, outer probes apply current to the sample and the inner probes measure voltage. The slope of the I-V curve then gives the resistance value for the sample under test. Figures [5.3 - 5.5] show the resistance plots with respect to time at 25^0C, 35^0C and 45^0C respectively. The start of the measurement shows high value of resistance, because contact resistance exists between the probe and sample, a large current must flow through the sample so that the voltage generated between the inner two probes will be large enough to measure accurately [88]. Hence, the resistance values were taken at the end of the measurement.
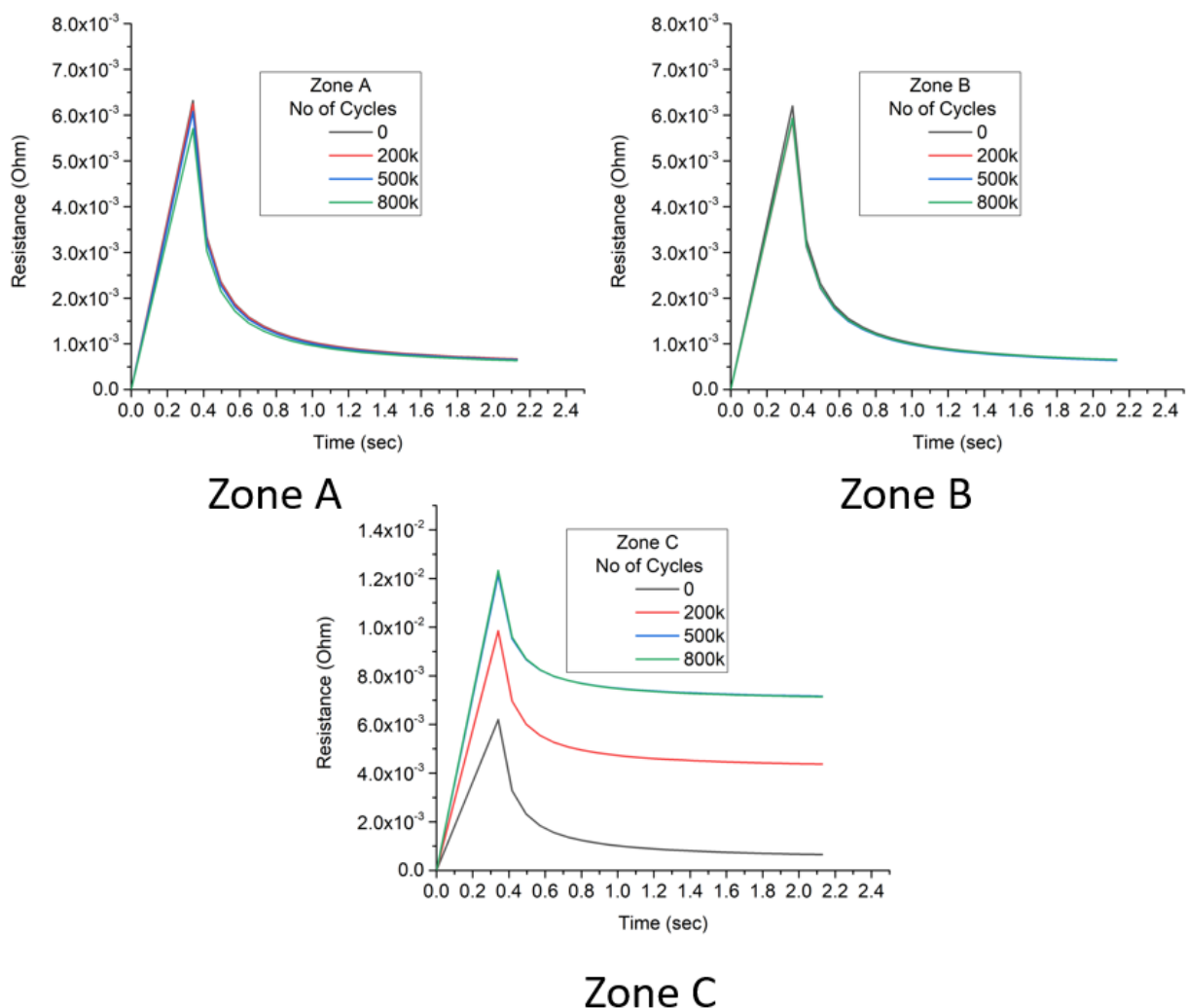
Figure 5.3: Plot of resistance vs time under (0,200k,500k,800k,) cycles at 25^0C.

As per Figure 3.21, the amplitude of stresses is less at zones(A and B) as compared to zone C that's why zone C shows very different behavior under mechanical loadings. The temperature rise shows a very little effect on resistance values for all the three zones but on the other hand resistance shows considerable change due to mechanical loadings. From 0 to 500k cycles, all the plots show a very sharp rise in resistance values and after 500k there is a little change in values as can be seen in Figures [5.3 - 5.5]. All the measurements show stable values at the end of measurement time.
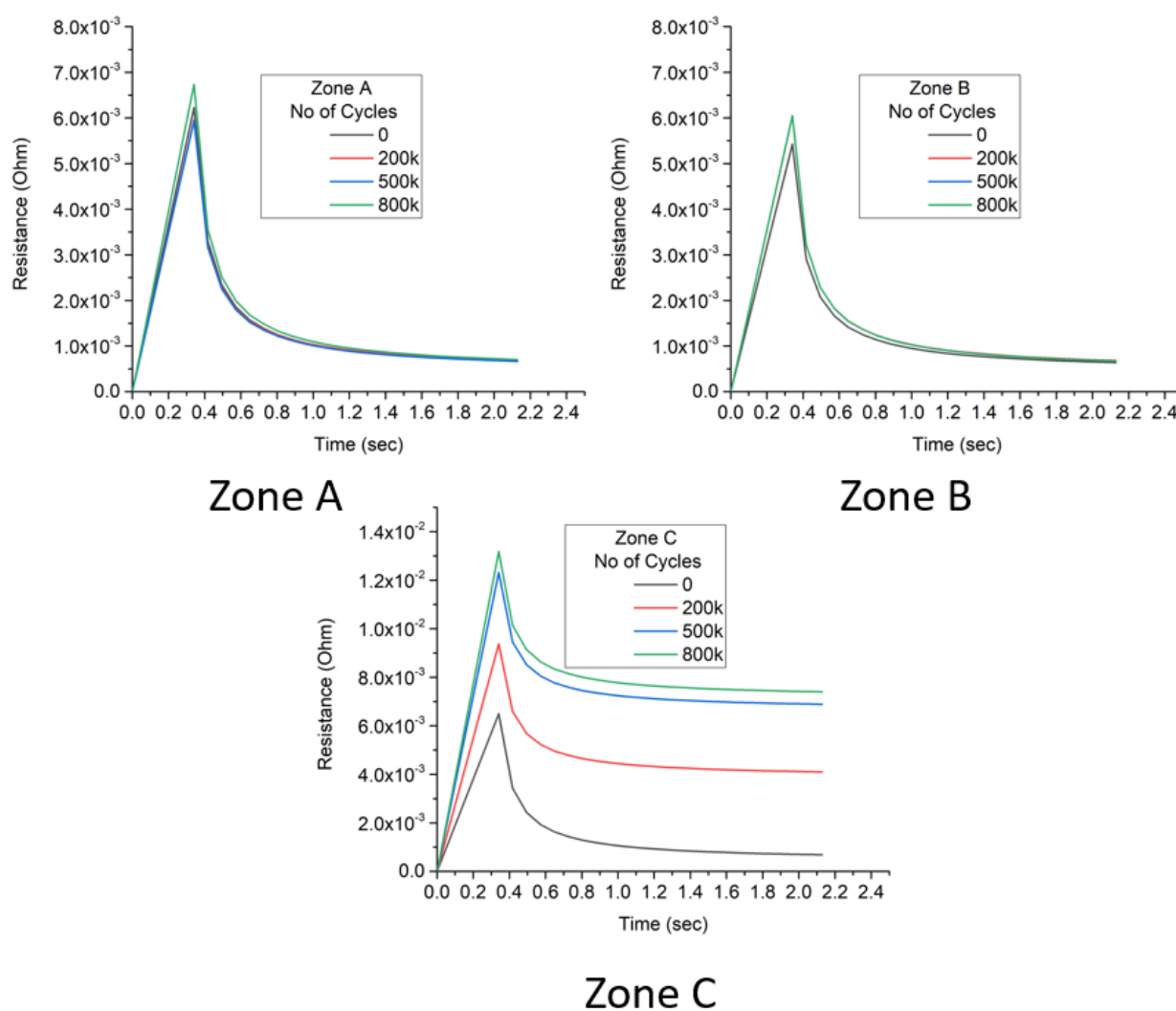
Figure 5.4: Plot of resistance vs time under (0,200k,500k,800k,) cycles at 35^{0}C.
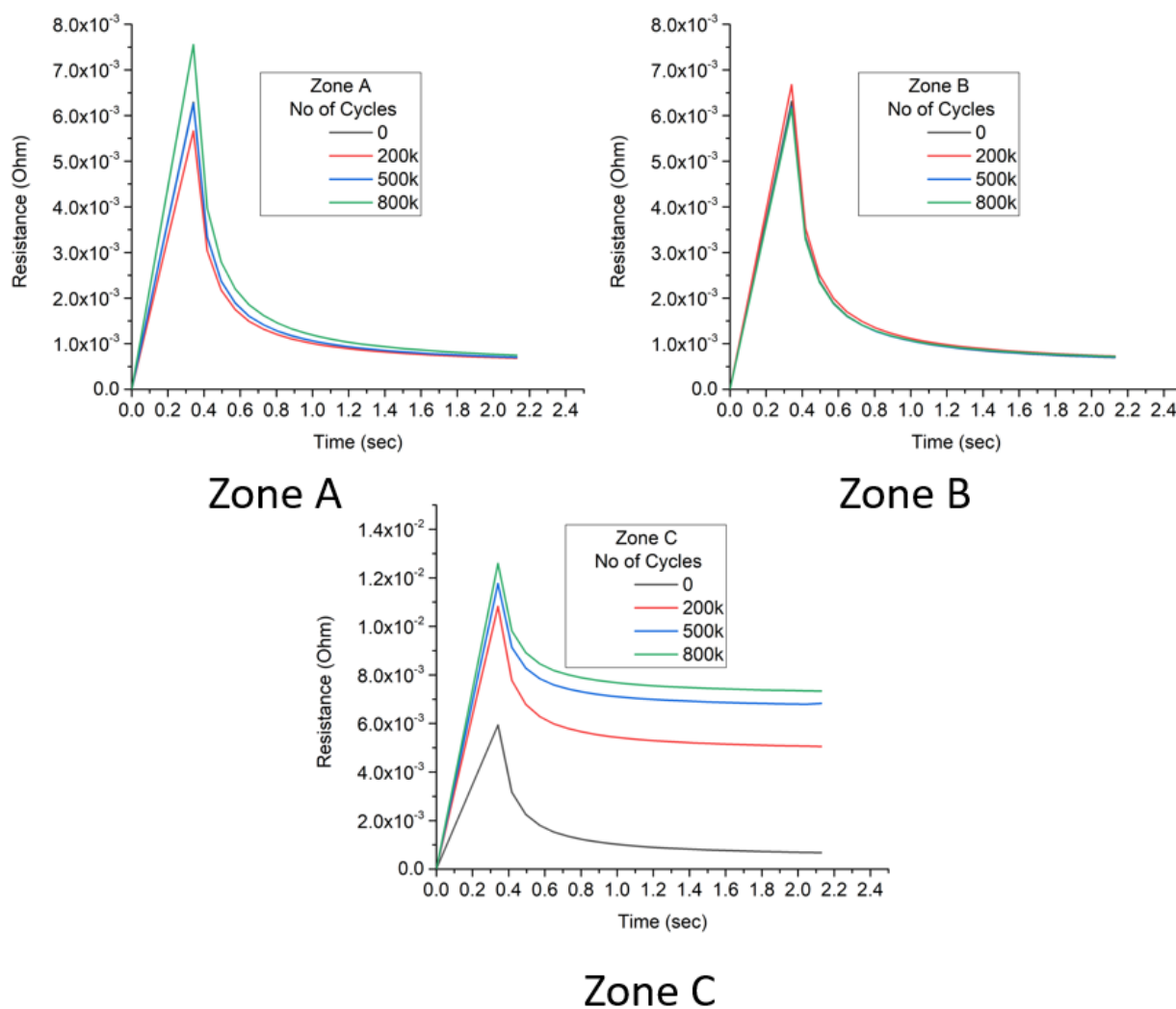
Figure 5.5: Plot of resistance vs time under (0,200k,500k,800k,) cycles at 45^{0}C.

5.2.1   Resistance Variations

Figure 5.6 shows average resistance values obtained from I-V curves. Exponential rise in resistance values can be seen due to mechanical cycles whereas very little change observed due to temperature rise. There is 1657 % rise in resistance values from 0 cycles to 800k cycles at 45^{0}C for zone C whereas this change is very little, around 1.1 % and 1.34 %, for zones A and B respectively.

```
UNIVERSITAT ROVIRA I VIRGILI
Electrical Properties and Surface Characterization of Thin Copper Films Subjected to Mechanical Vibrations
Sufyan Azam
```
Doctoral Thesis   Sufyan Azam
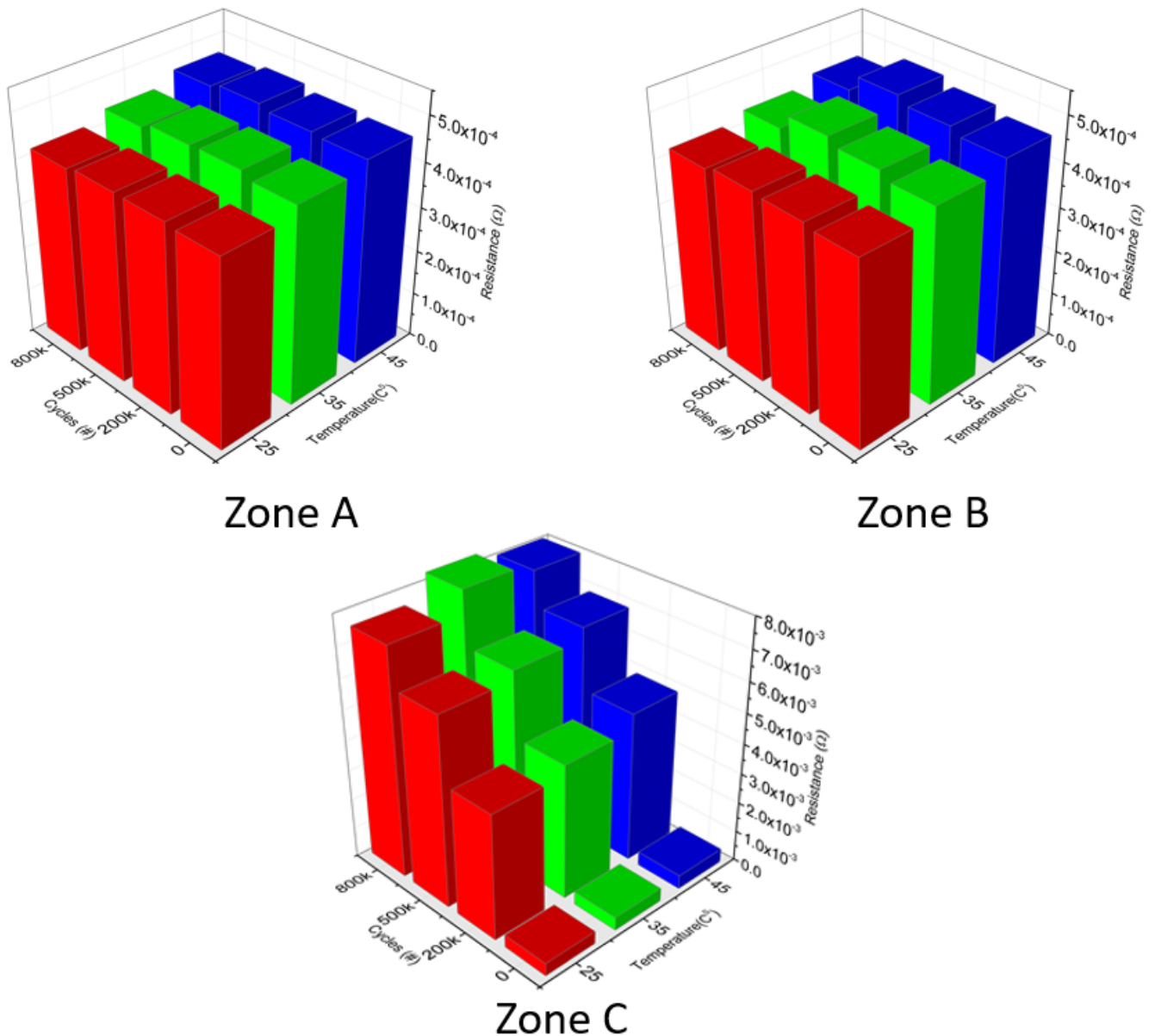
Figure 5.6: 3D bar plot of resistance R

5.3   Changes in other Electrical Properties under Mechanical and Thermal Loading

Average sheet resistance values against mechanical cycles at different temperatures can be seen in Figure 5.7. As opposed to resistance or resistivity, sheet resistance is directly measured using four point probe measurements. The effect of mechanical cycles for zone C can be clearly observed having an exponential rise in sheet resistance values. Before cyclic loading at 25^0C, sheet resistance values for zones A, B and C are 1.34, 1.33 and 1.33 ($m\Omega/sq$) respectively. The same sample when subjected to 800k cycles, the sheet resistance values at 25^0C for the zones A, B
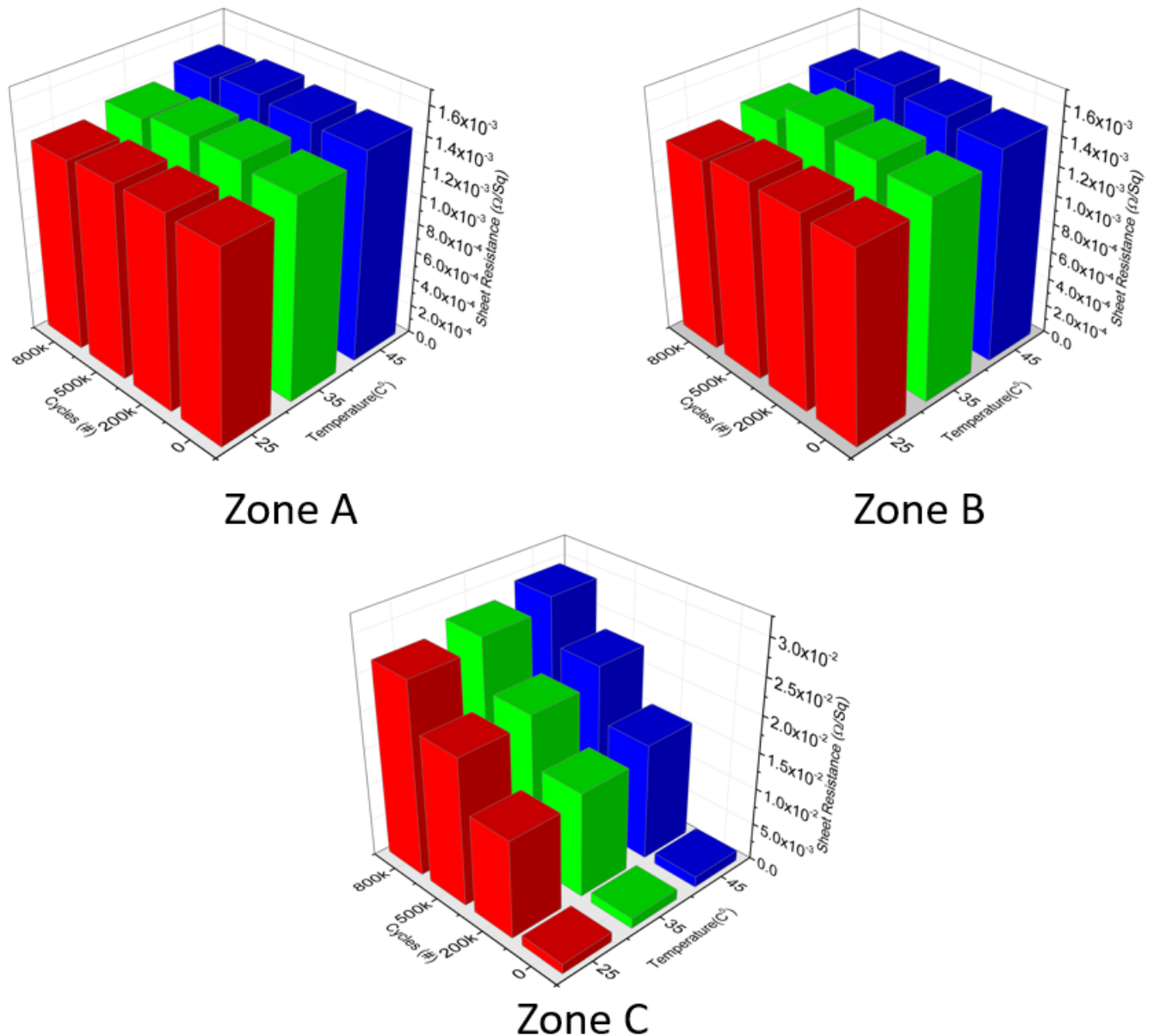
Figure 5.7: 3D bar plot of sheet resistance R_{sh}.

and C are 1.34, 1.33 and 24.19 ($m\Omega/sq$) respectively. This behavior is not seen in case of thermal loadings where 20^0C rise in temperature gives only 1 % rise in sheet resistance values. All the zones behave in similar way under thermal loadings.

The next two electrical properties obtained from the experimental work are resistivity ρ and conductivity σ as shown in Figures [5.8 − 5.9] respectively. Resistivity is the inherent property of the material that quantifies the strength of the material to resist or conduct electric current. As seen in the previous Figures [5.6 − 5.7], the mechanical cycles play an important rule in changing electrical properties of the sample under test; the same applies for resistivity and conductivity. After the sample undergoes 800k cycles, the zone C of the sample becomes more resistive and
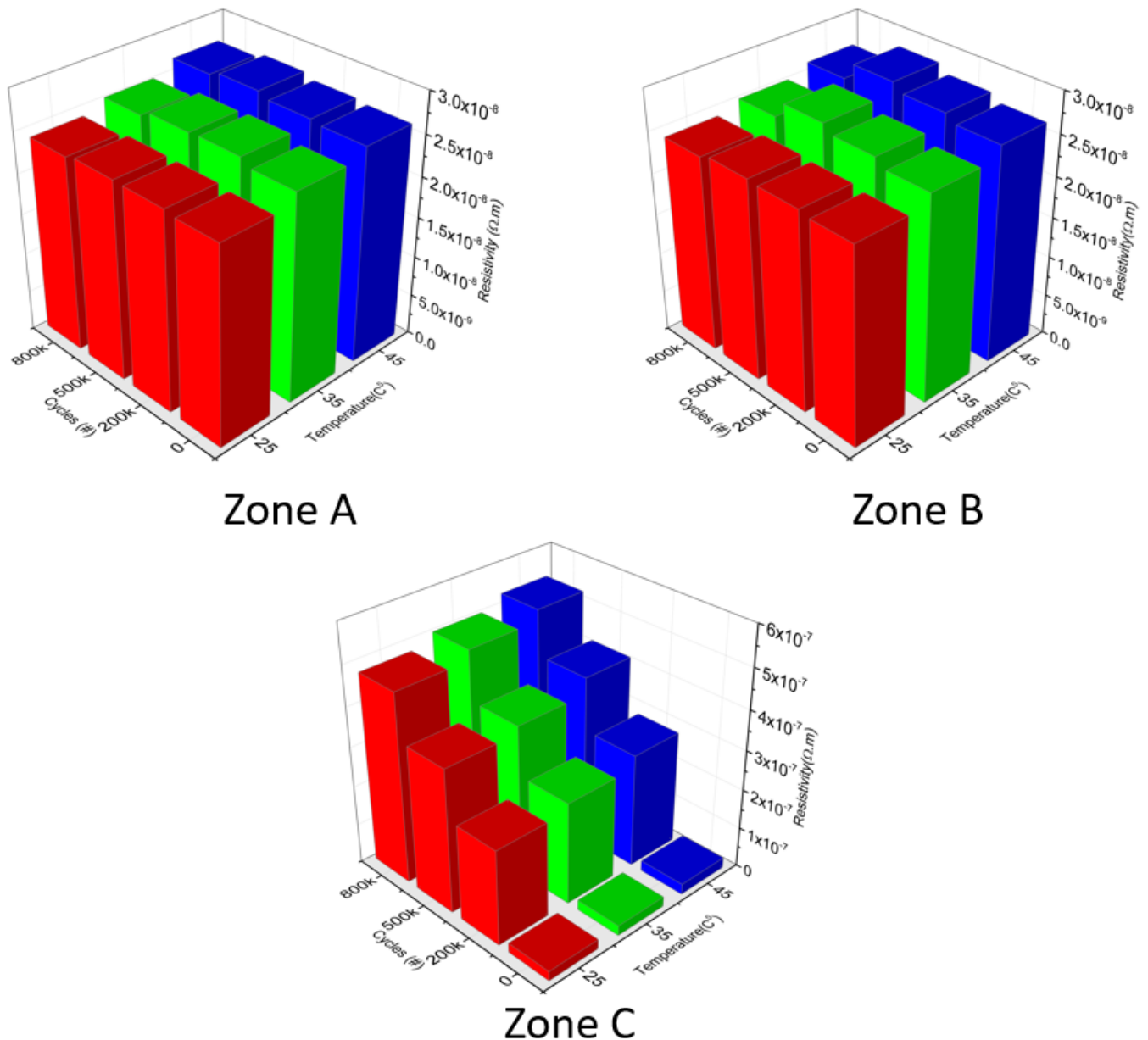
Figure 5.8: 3D bar plot of resistivity ρ.

the value of resistivity changes from $2.40\text{x}10^{-8}$ $(\Omega \cdot m)$ to $4.35\text{x}10^{-7}$ $(\Omega \cdot m)$. On the other hand zones A and B still show almost same values even after nearly a million cycles.

The last electrical property to discuss is conductivity σ.Being reciprocal of the resistivity, it quantifies how smoothly current flows in a conductor. A large value of σ means the material is a very good conductor of electrical current. Figure 5.9 shows the average conductivity values measured for different zones under variable loading cycles and temperatures. Almost 95 % decrease in conductivity, $4.15\text{x}10^{7}$ (S/m) - $2.29\text{x}10^{6}$ (S/m), can be observed after 800k cycles for zone C. A slight change due to temperature variations can also be seen in all the three zones.
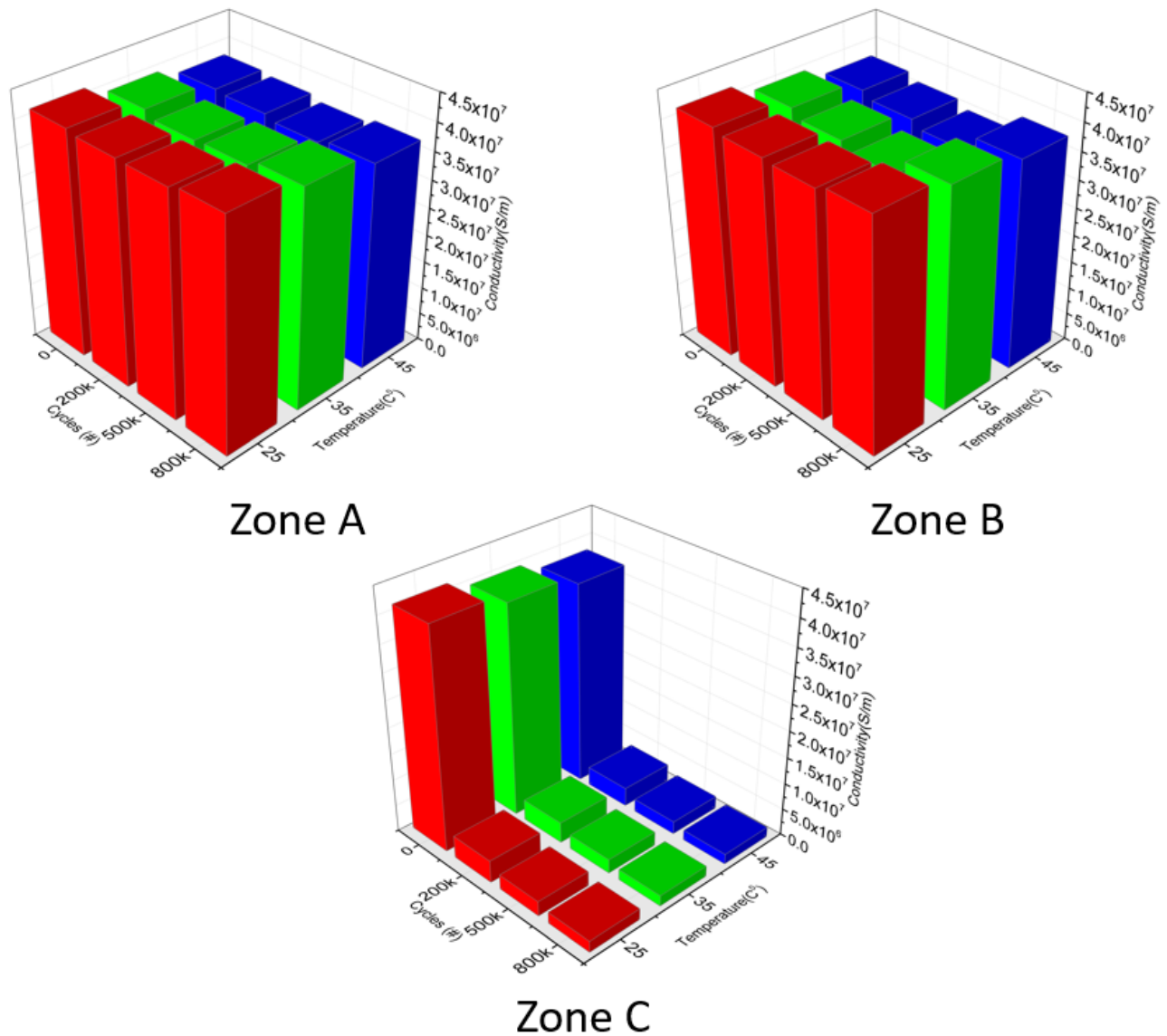
Figure 5.9: 3D bar plot of conductivity σ.

All of the experimental results showed a very different behavior of electrical properties under cyclic loading for the zone C. The accelerometer amplitude, as evidenced in Figures 3.20(b) and 3.21(b), is low at position 2 while a high amplitude of acceleration can be seen at position 1. On the other hand, high stresses have be observed at position 2 of Figure 3.21(a) while a little amplitude of stress can be seen at position 1 of the same Figure 3.21(a). The large variations in electrical properties of the samples, after mechanical cyclic loading near zone C, is due to large amplitude of stresses near this area, numbered as position 2 in Figure 3.21(a).

This large change in electrical properties leads towards surface analysis to better understand the micro structural changes in zone C that propagates electrical changes in the samples.

5.4   Surface Analysis

Vibration stresses produced a noticeable change in surface color of all samples. The typical lustrous reddish brown color of undamaged copper changed to dark brown after vibrations, indicating damage and/or chemical modification (i.e. oxidation) of the surface. For these reasons, the samples were analyzed by ESEM, elemental composition and contact angle measurements.
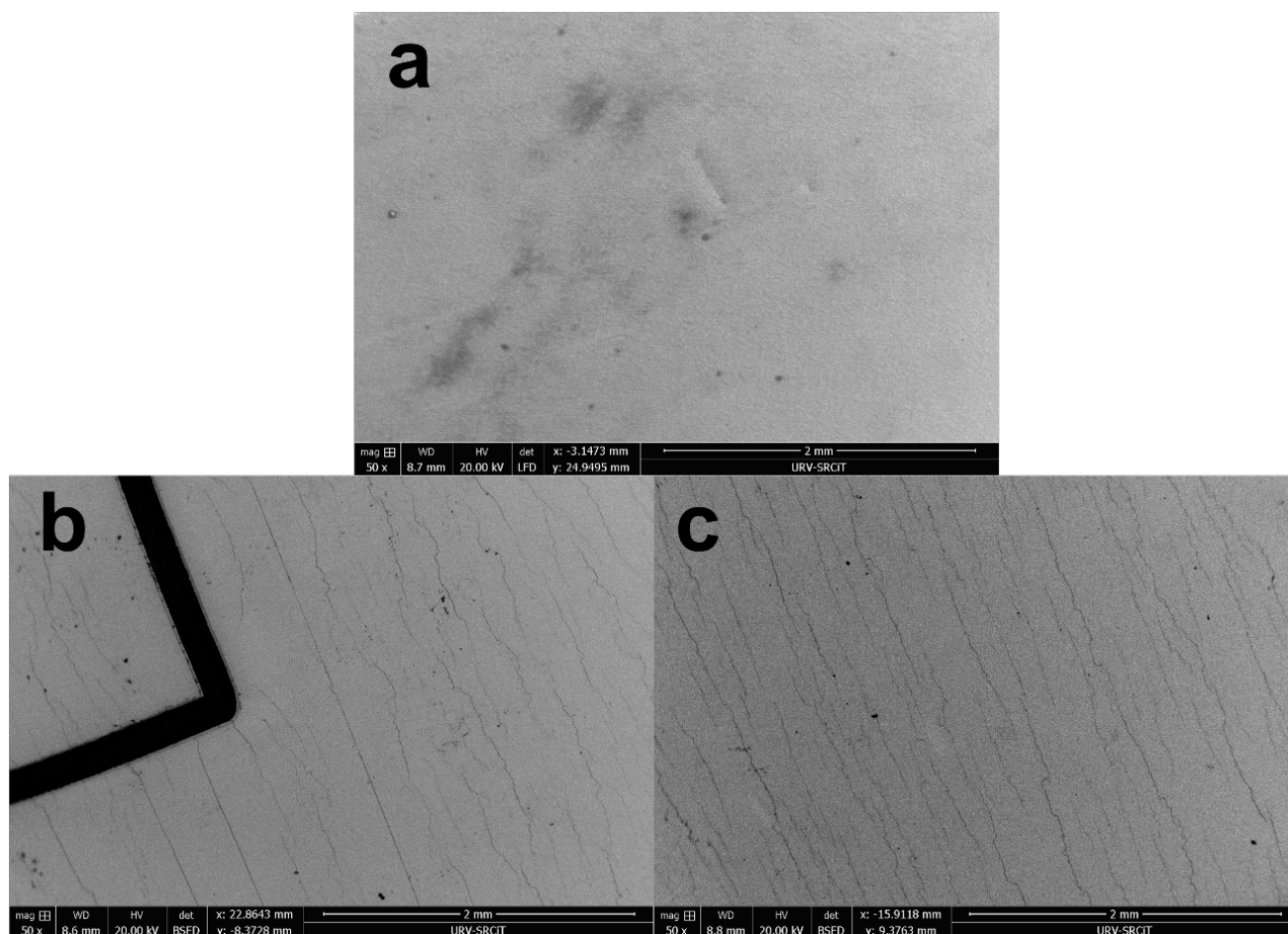
Figure 5.10: ESEM images (back-scattered mode) of samples S0(*a*), S1(*b*) and S3(*c*)
at 50X magnification.

Figures [5.10 − 5.12] show the ESEM pictures of samples S0, S1 and S3 at different magnifications. The morphology of the untreated sample shows a smooth surface without cracks at low magnification Figure 5.10a and the presence of rolling traces on crystalline domains probably due to the mode of fabrication of the samples Figure 5.11a and Figure 5.12a. After 200k and 800k fatigue cycles, the surfaces clearly develop cracks as evidenced in panels b and c of Figures [5.10 − 5.12]. These cracks are perpendicular to the longitudinal axis of the samples and are the result

of the plastic deformation undergone by the samples after vibration stresses. The apparent density of cracks increases with the number of cycles from ∼3 cracks per mm at 200k cycles to ∼8 cracks per mm at 800k cycles, indicating a dependence of the overall damage with the number of cycles. These cracks have ∼1 µm width and are several millimeters long and seem to follow dislocation lines perpendicular to the longitudinal axis Figure 5.13. This type of cracks have been observed in other fatigue studies of copper thin films and is attributed to the presence of dislocations [89, 90] and favored by surface roughness [91].
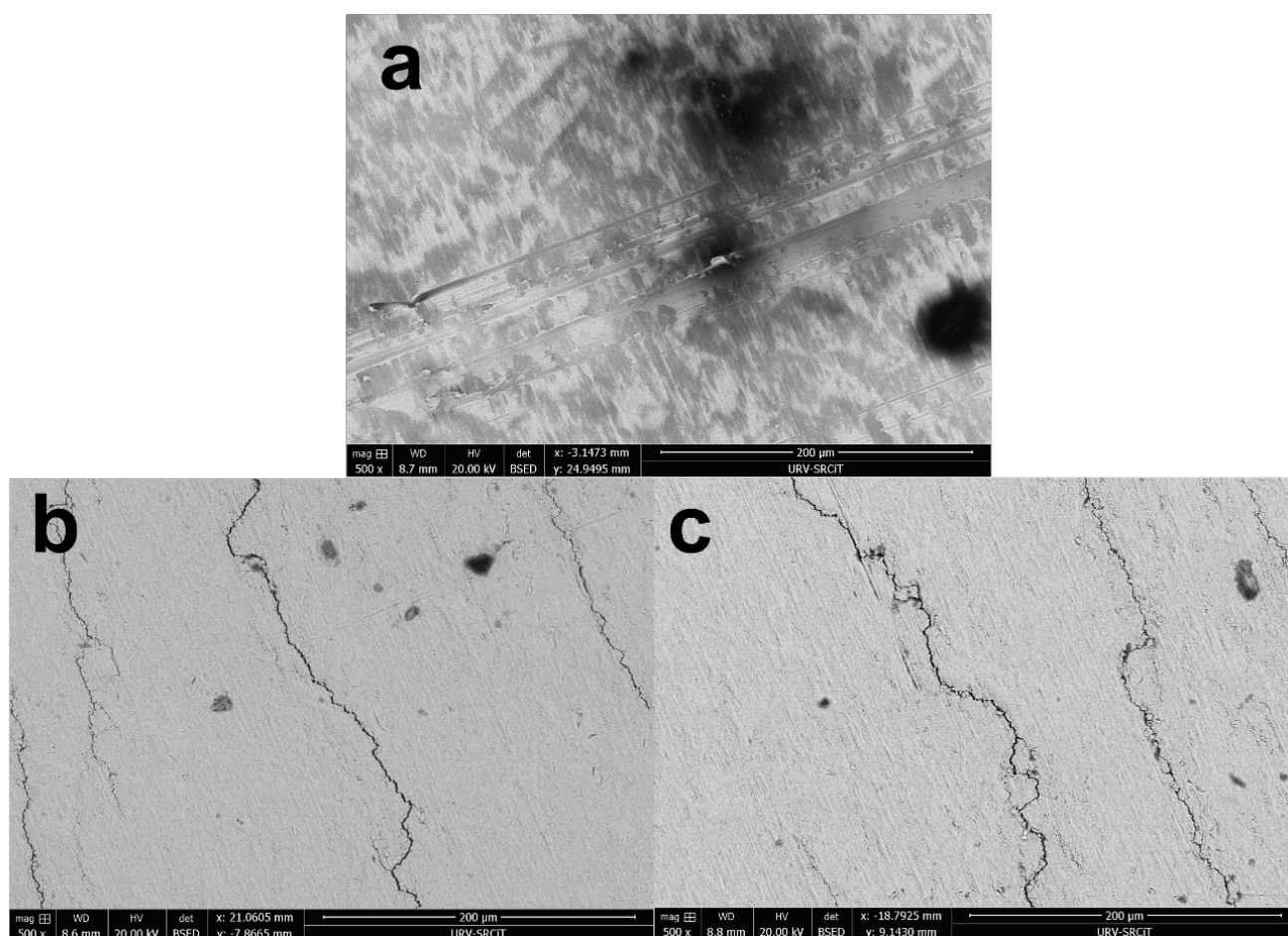
Figure 5.11: ESEM images (back-scattered mode) of samples S0(*a*), S1(*b*) and S3(*c*) at 500X magnification.

Interestingly, the surface composition 100 % copper is not altered even upon a high number of cycles, indicating that the fatigue stress only produces physical damage and not chemical processes such as oxidation as shown in Figure 5.14.
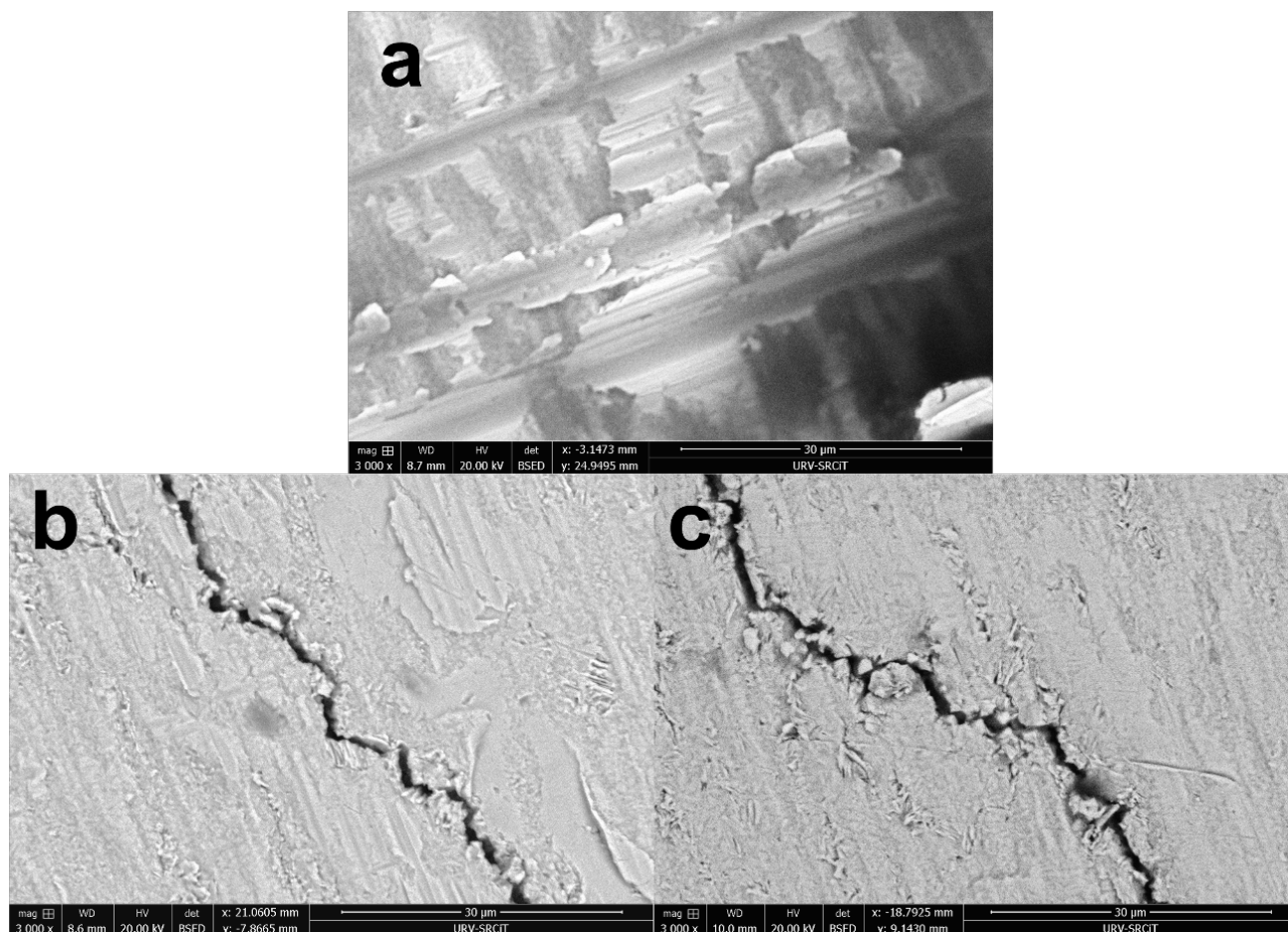
Figure 5.12: ESEM images (back-scattered mode) of samples S0(*a*), S1(*b*) and S3(*c*) at 3000X magnification.
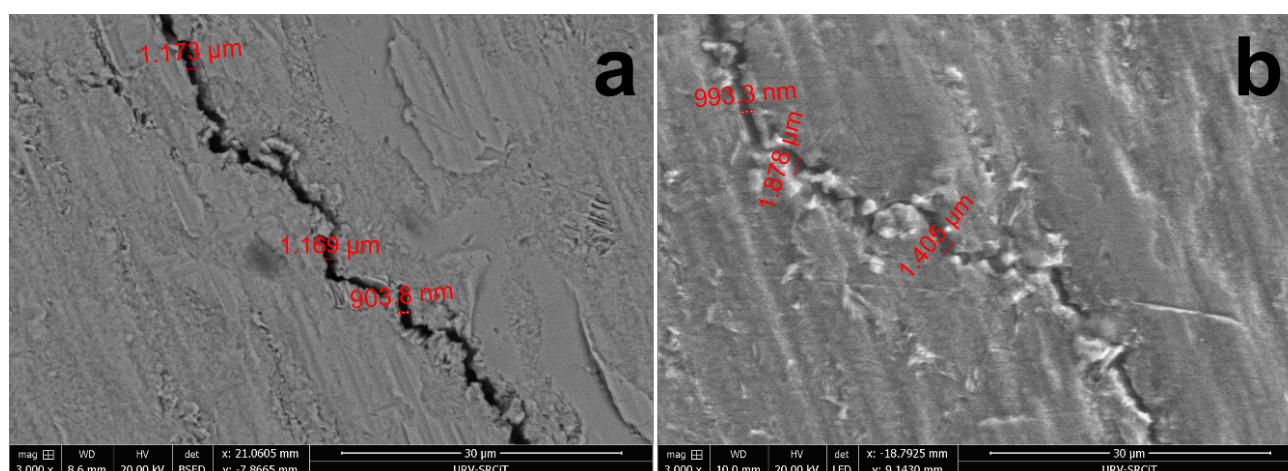
Figure 5.13: ESEM images corresponding to Figures 5.12b and 5.12c respectively, showing crack dimensions (at 3000X magnification).
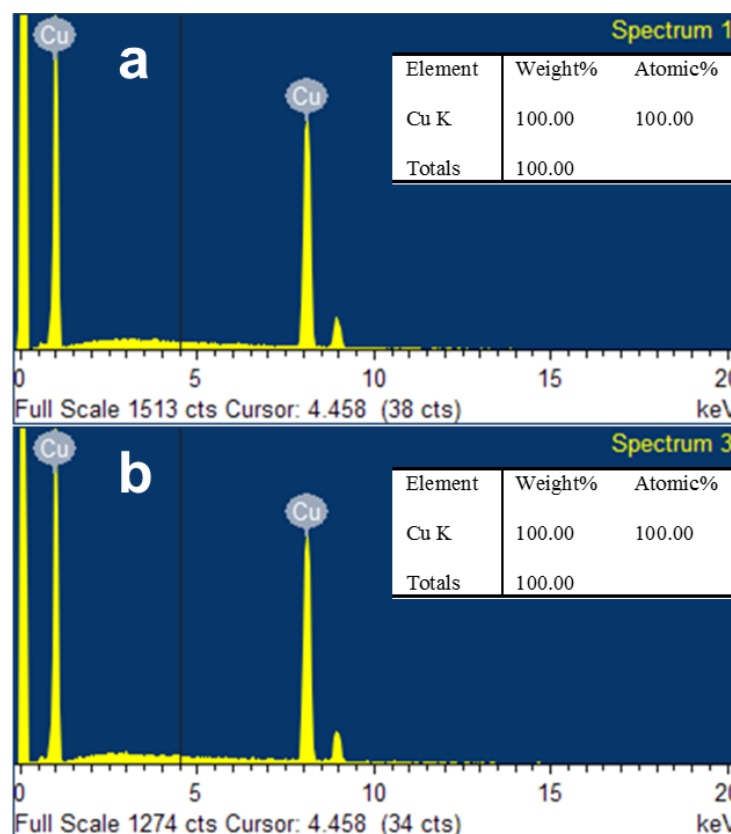
Figure 5.14: Surface elemental composition of samples corresponding to: (*a*) Figure 5.12a (before vibrations), (*b*) Figure 5.12c (after vibrations).

The samples were also analyzed using water droplet contact angle. This technique is useful to assess hydrophilicity/hydrophobicity changes on surfaces and is widely used in adsorption and surface modification studies [92]. Figures 5.15 and 5.16 show the contact angle measurements for samples before and after vibration, respectively. The observed angles for untreated samples ranges from 78 to 95 degrees, similar to what has been observed for pure copper and indicates a hydrophilicity similar to that of aluminum [93]. After vibration damage, the contact angle increases to 117-119 degrees, typical of hydrophobic surface such as PTFE (polytetrafluoroethylene). This marked change in contact angle can be attributed to an increased surface roughness [94] and also to the accumulation of very small air bubbles on the cracks that difficult water contact with the surface.
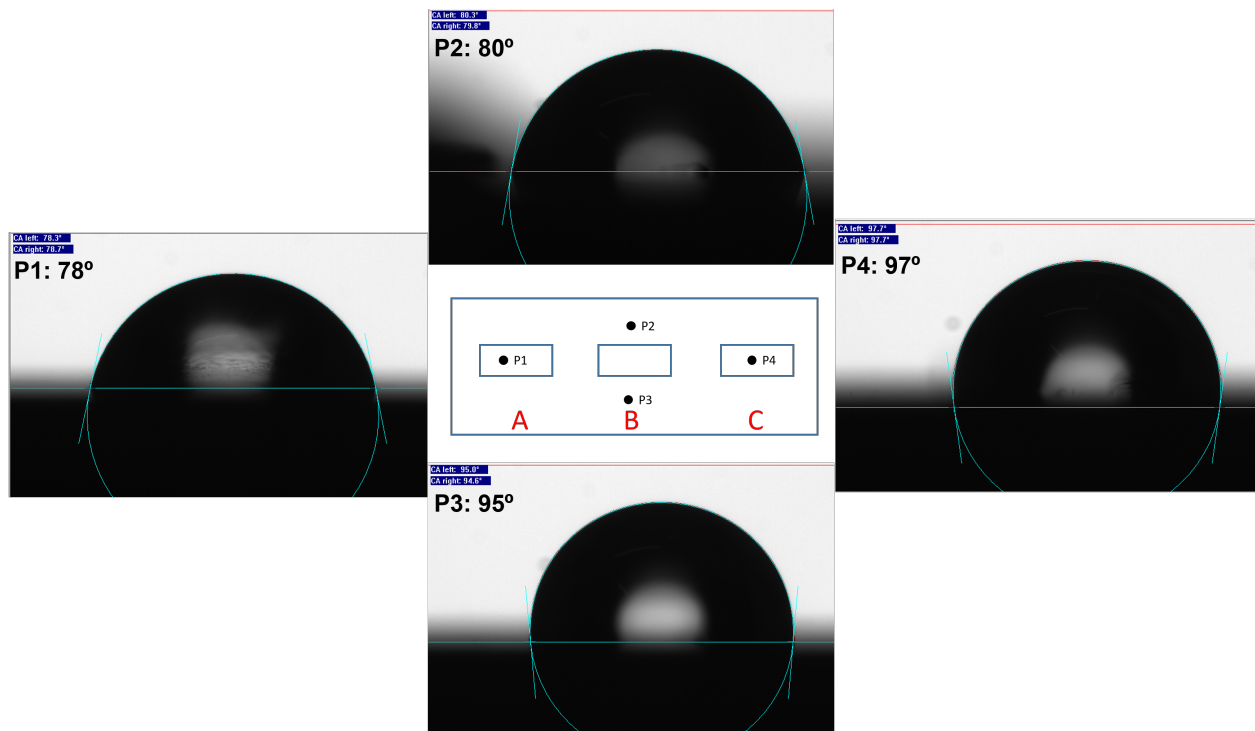
Figure 5.15: Contact angle measurements of sample S0 at different locations.
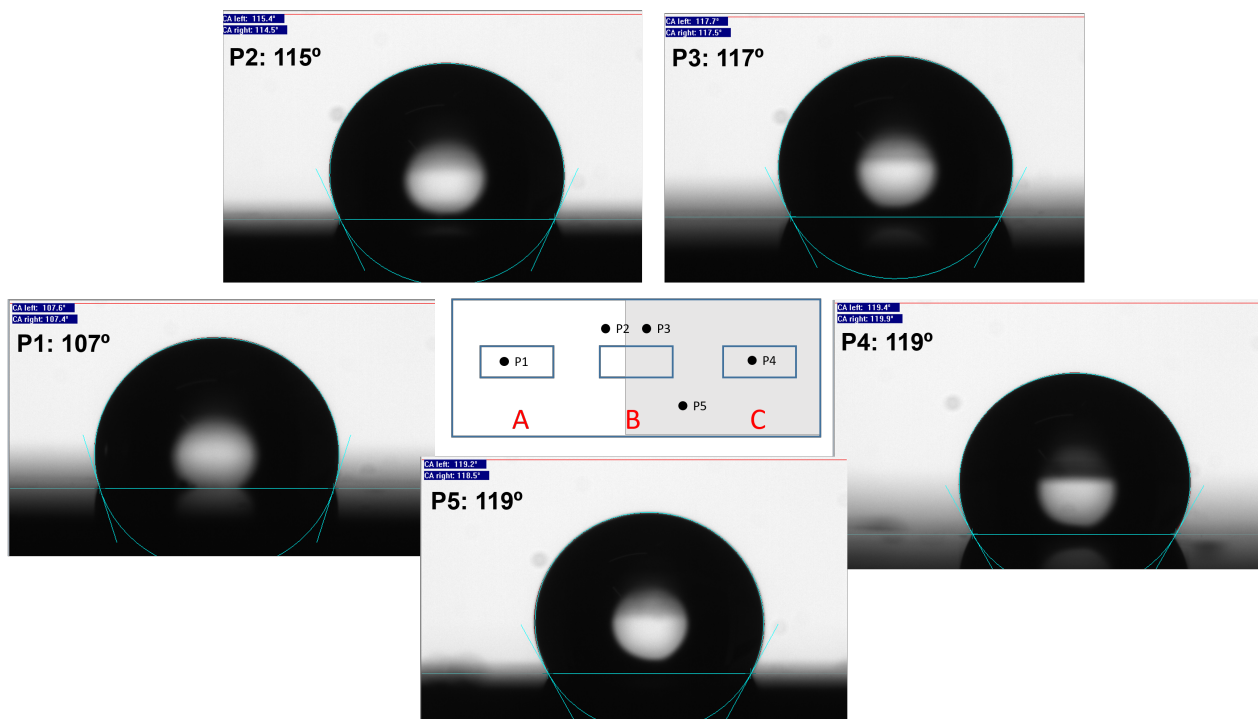
Figure 5.16: Contact angle measurements of sample S3 at different locations. The gray area indicates a higher density of cracks in the sample.

5.5   Preliminary conclusions

In this chapter, the effect of high cycle vibration fatigue and the effect of thermal variations on the electrical properties of thin copper films of thickness 18 μm bounded to FR4 epoxy laminate of 1.5 mm thick were determined experimentally. The specimens were cut to equal dimensions of 50x25 mm having three isolated rectangles, (zone A, zone B, zone C) of 10x5 mm dimensions. The electrical properties of each rectangle were then measured separately using custom made dual axes four−point probe (DA4PP). For the first time, the influence of high cycle vibration fatigue on their electrical properties, with and without thermal variations is determined in this chapter.

It has been evident from the results of the obtained data at zone C that the stresses induced due to mechanical vibrations play an important rule in the electrical properties of PCBs. This is due to the surface damage caused by mechanical vibrations near this zone. Interestingly, at zones A and B no such behavior is noticed. At these zones, the electrical properties of the samples before and after mechanical cycles were almost the same. No cracks were found near these zones whereas the apparent density of cracks, as seen by ESEM at zone C, increased from ∼3 cracks per mm at 200k cycles to ∼8 cracks per mm at 800k cycles. This indicates a dependence of the overall damage with the number of cycles. The surface composition of the samples i.e., 100 % copper, was found to be the same as before cyclic loadings. The hydrophobicity changes on surfaces, due to mechanical cycles, showed rise in contact angle measurements; this change can be attributed to an increased surface roughness [94]. Although the temperature variations showed changes in electrical properties of the specimens but these are very small as compared with mechanical cyclic loadings.

Chapter 6

Conclusion and Future Work

Printed Circuit Boards (PCBs) and Micro-Electrical Mechanical Systems (MEMS) have a great interest in electrical, electronic and mechanical instruments. PCBs consist mainly of thin copper films embedded to composite or metallic substrates. During the function, many mechanical, vibration and thermal loadings arise due to electrical current fluctuations. There are many other important parameters which are crucial for the performance and reliability of these devices. These parameters e.g., stress amplitude, mean stress, downsizing film dimension and crack initiation and propagation still, need more study and investigations. The Proposed research was concerned on the development of high cyclic vibrations and other size parameters in (MEMS) devices in applications. The purpose of the research was, to create a better link to the damage mechanisms of the material itself and to identify the crucial parameters that control material's sensitivity to high frequency vibrations with respect to their effect on electrical performance with and without thermal variations.The research was comprised of two phases.

During the first phase of this study, the vibration characteristics of these materials were studied in details. The cantilever samples made of bare copper bounded to FR4 have been studied to analyze, for the first time, the vibration behavior of specimens with different aspect ratios, with and without central holes of different diameters. Thin copper films of 35 μm thickness bounded to FR4 epoxy laminate of 1.5 mm thickness were studied. The vibrational characteristics, such as natural frequencies and damping ratios, were determined experimentally and analytically using a finite element method for four groups of samples, in order to study the geometric effects and the presence of a central hole of different diameters. It has

been found that these sizes are suitable to be used as electronic circuit boards that undergo significant frequency changes ranging from 40 Hz to 1k Hz. The fundamental resonance frequency of all the specimens was found to be less than 40 Hz and the influence of a central hole was not significant to affect the modal properties.

The second stage of the present research addressed the influence of cyclic vibrations on their electrical properties, with and without thermal variations, in order to study the possible damage mechanisms that these materials undergo and how they affect their performance. The thermal variations showed a very little effect on sheet resistance values for all of the three zones but on the other hand the obtained values showed a considerable change due to mechanical loadings. The effect of mechanical cycles for zone C gave an exponential rise in sheet resistance values. This behavior was not observed in case of thermal loadings where 20^0C rise in temperature gave only 1 % rise in sheet resistance values. After 200k and 800k vibration cycles, the surfaces clearly developed cracks shown by ESEM images. These cracks were the result of the plastic deformation undergone by the samples after vibration stresses. The density of cracks was increased with the number of cycles from ~3 cracks per mm at 200k cycles to ~8 cracks per mm at 800k cycles, indicating a dependence of the overall damage with the number of cycles. The cracks were found to be ~1 µm in width and several millimeters long.

The surface composition analysis indicated that the vibration stress only produced physical damage and not chemical processes such as oxidation. The samples were also analyzed using water droplet contact angle. The observed angles for untreated samples were found to be less than those after mechanical vibrations. This marked change in contact angle can be attributed to an increased surface roughness and also to the accumulation of very small air bubbles on the cracks that difficult water contact with the surface.

This thesis has thus been a contribution to a better understanding of the relationship between damage accumulation and electrical performance of PCB boards and MEMS and may lead to improvements of their fabrication. This makes the results of great practical importance and the developed assay methodology can be extended to other thin films.

Ongoing work is focused on studying the:

- influence of film thickness,

- influence of film material such as gold (A_u), copper (C_u) and aluminum (A_l),

- and influence of amplitude and frequency of vibrations

on the electrical performance of these composites under mechanical and thermal loadings.

List of Figures

```
UNIVERSITAT ROVIRA I VIRGILI
Electrical Properties and Surface Characterization of Thin Copper Films Subjected to Mechanical Vibrations
Sufyan Azam
```
Doctoral Thesis

Sufyan Azam

List of Tables

Bibliography

[01]   Steinberg, D.S. "Vibration Analysis for Electronic Equipment", 3rd ed. Wiley: Hoboken, NJ, USA, 2000. ISBN: 978-0-471-37685-9

[02]   Gharaibeh, M.A; Pitarresi, J.A. "Random vibration fatigue life analysis of electronic packages by analytical solutions and Taguchi method". Microelectron. Reliab. 2019, 102, 113475. http://dx.doi.org/10.1016/j.microrel.2019.113475

[03]   Amy, R.A.; Aglietti, G.S.; Richardson, G. "Reliability Analysis of Electronic Equipment Subjected to Shock and Vibration—A Review". Shock Vibrat. 2009, 16, 45–59. http://dx.doi.org/10.1155/2009/546053

[04]   Jiao, J.; De, X.; Chen, Z.; Zhao, T. "Integrated circuit failure analysis and reliability prediction based on physics of failure". Eng. Fail. Anal. 2019, 104, 714–726. http://dx.doi.org/10.1016/j.engfailanal.2019.05.021

[05]   Ewins, D.J. "Modal Testing: Theory, Practice and Application", 2nd ed.;Wiley: Hoboken, NJ, USA, 2009. ISBN: 978-0-863-80218-8

[06]   Armentani, E.; Caputo, F.; Esposito, L.; Giannella, V.; Citarella, R. "Multibody Simulation for the Vibration Analysis of a Turbocharged Diesel Engine". Appl. Sci. 2018, 8, 1192. http://dx.doi.org/10.3390/app8071192

[07]   Armentani, E.; Giannella, V.; Citarella, R.; Parente, A.; Pirelli, M. "Substructuring of a Petrol Engine: Dynamic Characterization and Experimental Validation". Appl. Sci. 2019, 9, 4969. http://dx.doi.org/10.3390/app9224969

[08]   Bianco, D.; Adamo, F.P.; Barbarino, M.; Vitiello, P.; Bartoccini, D.; Federico, L.; Citarella, R. "Integrated Aero–Vibroacoustics: The Design

Verification Process of Vega-C Launcher". Appl. Sci. 2018, 8, 88. http://dx.doi.org/10.3390/app8010088

[09]   Cifuentes, A.O. "Estimating the dynamic behavior of printed circuit boards". IEEE Trans. Comp. Packag. Manuf. Technol. B 1994, 17, 69–75. http://dx.doi.org/10.1109/96.296433

[10]   Aytekin, B.; Ozguven, H.N. "Vibration Analysis of a Simply Supported PCB with a Component—An Analytical Approach". In Proceedings of the IEEE Proceedings 10th Electronics Packaging Technology Conference, Singapore, 9–12 December 2008; pp. 1178–1183. http://dx.doi.org/10.1109/EPTC.2008.4763589

[11]   Ren, G.; Li, B.; Li, D.; Jiao, Y. "Modal Analysis of the Printed Circuit Board Based on Finite Element Method". In Proceedings of the 2014 International Conference on Computer Science and Electronic Technology, Shenzhen, China, 27–28 December 2014; Atlantis Press: Paris, France, 2014; pp. 150–154. http://dx.doi.org/10.2991/iccset-14.2015.32

[12]   Bhavsar, N.R.; Shinde, H.P.; Bhat, M. "Determination of Mechanical Properties of PCB". Int. J. Mech. Eng. Robot. 2014, 2, 23–27. Available online: http://www.irdindia.in/journal_ijmer/pdf/vol2_iss4/6.pdf (accessed on 5 June 2020).

[13]   Veilleux, E. "Vibration Control of Printed-Circuit Boards in a Dynamic Environment". IEEE Trans. Parts Mater. Packag. 1970, 6, 100–105.]http://dx.doi.org/10.1109/TPMP.1970.1136264

[14]   Veprik, A.M. "Vibration Protection of Critical Components of Electronic Equipment in Harsh Environmental Conditions". J. Sound Vibrat. 2003, 259, 161–175. http://dx.doi.org/10.1006/jsvi.2002.5164

[15]   Prashanth, M.D. "Vibration Analysis of Printed Circuit Boards: Effect of Boundary Condition". AIP Conf. Proc. 2018, 1943, 020018. http://dx.doi.org/10.1063/1.5029594

[16]   Qi, X.; Zhou, B.; Li, G.; Zhang, P.; En, Y. "Effect of fixation method on solder joint vibration fatigue reliability of high density PCB assembly". In Proceedings of the IEEE Proceedings 12th International Conference on

Electronic Packaging Technology and High Density Packaging, Shanghai, China, 8–11 August 2011; pp. 1–4. http://dx.doi.org/10.1109/ICEPT. 2011.6066970

[17]   Rao, V.P.; Singh, A.K.; Ranganath, S. "Vibration Analysis of Printed Circuit Board Plate with Varying Boundary Conditions". Indian J. Sci. Technol. 2016, 9, 1–3. http://dx.doi.org/10.17485/ijst/2016/v9i34/100916

[18]   Hall, W.J.; Williams, P.T. "Separation and recovery of materials from scrap printed circuit boards". Res. Cons. Recycl. 2007, 51, 691–709. http://dx. doi.org/10.1016/j.resconrec.2006.11.010

[19]   Hassan, M.K.; Abdellah, M.Y.; ElAbiadi, T.; Mohamed, A.F.; Azam, S.; Marzouk, W.W. "Essential Work of Fracture and Size Effect in Copper/Glass-Reinforced Epoxy Laminate Composites Used as MEMS Devices". Am. J. Mech. Eng. 2017, 5, 234–238. Available online: http://www. sciepub.com/ajme/abstract/8369 (accessed on 15 June 2020).

[20]   Kraft, O.; Schwaiger, R.; Wellner, P. "Fatigue in thin films: lifetime and damage formation". Materials Science and Engineering: A, 2001. 319–321: p. 919-923. https://doi.org/10.1016/S0921-5093(01)00990-X

[21]   Zhang, G.P.; et al. "Effect of film thickness and grain size on fatigue-induced dislocation structures in Cu thin films". Philosophical Magazine Letters, 2003. 83(8): p. 477-483. https://doi.org/10.1080/ 0950083031000151383

[22]   Mönig, R.; Keller, R.; Volkert, C. "Thermal fatigue testing of thin metal films". Review of Scientific Instruments, 2004. 75(11): p. 4997-5004. https: //doi.org/10.1063/1.1809260

[23]   Zhang, G.P.; et al. "Damage behavior of 200-nm thin copper films under cyclic loading". Journal of Materials Research, 2005. 20(1): p. 201 - 207. https://doi.org/10.1557/JMR.2005.0019

[24]   Zhang, G.P.; et al. "Length-scale-controlled fatigue mechanisms in thin copper films". Acta Materialia, 2006. 54(11): p. 3127-3139. https://dx.doi. org/10.1016/j.actamat.2006.03.013

[25]   Zhang, G.P.; et al. "Fatigue and thermal fatigue damage analysis of thin metal films". Microelectronics Reliability, 2007. 47(12): p. 2007-2013. https://doi.org/10.1016/j.microrel.2007.04.005

[26]   Sun, X.J.; et al. "Thickness dependent fatigue life at micro-crack nucleation for metal thin films on flexible substrates". Journal of Physics D: Applied Physics, 2008. 41(19): p. 195404. https://doi.org/10.1088/0022-3727/41/19/195404

[27]   Wang, D.; Volkert, C.A.; Kraft, O. "Effect of length scale on fatigue life and damage formation in thin Cu films". Materials Science and Engineering: A, 2008. 493(1–2): p. 267-273. https://doi.org/10.1016/j.msea.2007.06.092

[28]   Lee, D.-Y.; Song, J.-H. "Fatigue life and plastic deformation behavior of electro-deposited copper thin film under variable amplitude loading". International Journal of Fatigue, 2012. 38: p. 1-6. https://doi.org/10.1016/j.ijfatigue.2011.10.008

[29]   Hu, T.C.; et al. "Cyclic creep and fatigue testing of nano-crystalline copper thin films". Surface and Coatings Technology, 2013. 215: p. 393-399. https://doi.org/10.1016/j.surfcoat.2012.08.089

[30]   Kim, B.-J.; et al. "Crack nucleation during mechanical fatigue in thin metal films on flexible substrates". Acta Materialia, 2013. 61(9): p. 3473-3481. https://doi.org/10.1016/j.actamat.2013.02.041

[31]   Kraft, O.; et al. "Crack nucleation and propagation during fatigue of thin metal films". in ICF11, Italy 2005. 2013. https://doi.org/10.1016/j.msea.2017.09.079

[32]   Lee, C.-C. "Patterned film effects on the adhesion of Al/TiN barrier using fracture-energy based finite element analysis". Surface and Coatings Technology, 2013. 215: p. 400-406. https://doi.org/10.1016/j.surfcoat.2012.08.088

[33]   Sim, G.-D.; et al. "Effects of stretching and cycling on the fatigue behavior of polymer-supported Ag thin films". Materials Science and Engineering: A, 2013. 575: p. 86-93. https://doi.org/10.1016/j.msea.2013.03.043

[34]   Alam, M.Z.; et al. "Micro-mechanisms of fracture and strengthening in free-standing Pt-aluminide bond coats under tensile loading". Acta Materialia, 2014. 67: p. 278-296. https://doi.org/10.1016/j.actamat.2013.12.033

[35]   Chu, J.P.; et al. "Fabrication and characterizations of thin film metallic glasses: Antibacterial property and durability study for medical application". Thin Solid Films, 2014. 561: p. 102-107. https://doi.org/10.1016/j.tsf.2013.08.111

[36]   Jia, H.; et al. "Thin-film metallic glasses for substrate fatigue-property improvements". Thin Solid Films, 2014. 561: p. 2-27. https://doi.org/10.1016/j.tsf.2013.12.024

[37]   Tsai, P.H.; et al. "Fatigue properties improvement of high-strength aluminum alloy by using a ZrCu-based metallic glass thin film coating". Thin Solid Films, 2014. 561: p. 28-32. https://doi.org/10.1016/j.tsf.2013.06.085

[38]   Wimmer, A.; et al. "Damage evolution during cyclic tension–tension loading of micron-sized Cu lines". Acta Materialia, 2014. 67: p. 297-307. https://doi.org/10.1016/j.actamat.2013.12.006

[39]   Zhang, P.; et al.; "Micro-structural evolution, mechanical properties and deformation mechanisms of nano-crystalline Cu thin films alloyed with Zr". Acta Materialia, 2014. 76: p. 221-237. https://doi.org/10.1016/j.actamat.2014.04.041

[40]   Heinz, W.; Robl, W.; Dehm, G. "Influence of initial micro-structure on thermo-mechanical fatigue behavior of Cu films on substrates". Microelectronic Engineering, 2015. 137: p. 5-10. https://doi.org/10.1016/j.mee.2014.10.024

[41]   Walter, T.; et al. "High cycle fatigue properties of Cu films. Microelectronic Engineering", 2015. 137: p. 64-69. https://doi.org/10.1016/j.mee.2014.12.003

[42]   Zhao, X.; et al. "Fatigue behavior and failure mechanism of basalt FRP composites under long-term cyclic loads". International Journal of Fatigue, 2016. 88: p. 58-67. https://doi.org/10.1016/j.ijfatigue.2016.03.004

[43]   Campbell, F.C. "Introduction to Composite Materials". Structural Composite Materials, Ohio, ASM international, 2010, pp. 1-18. ISBN: 978-1-61503-037-8

[44]   Harris, B. "Engineering Composite Materials". The Institute of Metals, London, 1999. https://doi.org/10.1016/0263-8223(87)90073-0

[45]   Available online: http://www.library.iyte.edu.tr/tezler/master/makinamuh/T000703.pdf (accessed on 6 Sept 2018)

[46]   Igor, K. "Structure Integrity Analysis", chapter 9. Composites. Kindle ed., 2013, ASIN: B00BWY0ZDK

[47]   Tuakta, C. "Use of fiber Reinforced Polymer Composite in Bridge Structures", Massachusetts Institute of Technology, 2005. Available online: https://citeseerx.ist.psu.edu/viewdoc/download?doi=10.1.1.626.3393&rep=rep1&type=pdf (accessed on 15 Sept 2018)

[48]   Martin, A. Masuelli. "Introduction of Fiber-Reinforced Polymers - Polymers and Composites: Concepts, Properties and Processes". IntechOpen, 2013. https://doi.org/10.5772/54629

[49]   James, K. Wessel. "Handbook of Advanced Materials Enabling New Designs". John Wiley & Sons, Inc., 2004. ISBN: 978-0-471-46517-1

[50]   Autar, K. Kaw. "Mechanics of Composite Materials". 2nd ed, CRC Press, 2005. ISBN: 978-0-849-31343-1

[51]   Pandey, P.C. "Lecture of Composite Materials". Dept. of Civil Eng., IISc Bangalore. Available online: http://doer.col.org/handle/123456789/3948 (accessed on 15 Sept 2018)

[52]   Available online: http://www.sci.uokufa.edu.iq/ar/teaching/alihr/lect.3.pdf (accessed on 12 Oct 2018)

[53]   Lehman, R.L.; et., al. "Mechanical Engineering Handbook". 2 ed, Frank Kreith Boca Raton: CRC Press LLC, NY, USA, 2005. ISBN: 978-1-62870-482-2

[54]   Tsai, S. W. "Composite Design, 4th edn. Think Compo-sites". Dayton, OH, 1988. ASIN : B018OEDEXI

[55]   Jones, Robert M. "Mechanics of composite materials". 2 ed, Taylor & Francis, London, 1999. ISBN: 1-56032-712-X

[56]   Soden, P. D.; Hinton, M. J.; Kaddour, A. S. "Lamina properties, lay-up configurations and loading conditions for a range of fibre-reinforced composite laminates". Composites Science and Technology, Volume 58, Issue 7, 1998, Pages 1011-1022. https://doi.org/10.1016/S0266-3538(98)00078-5

[57]   Us Dept Of Defense. "Polymer matrix Composites Materials Usage, Design, and Analysis Composite Materials". Handbook vol 3. CRC Press, 2000. ISBN: 978-1-566-76970-9

[58]   Miracle, B.; Donaldson, D. B.; George, F."ASM handbook". ASM International: Materials Park, OH, USA, 2001. ISBN: 978-0-87170-703-1

[59]   Carl Zweben, "Composite Materials and Mechanical Design, Mechanical Engineer's Handbook". 2nd ed., Myer Kutz, Ed., John Wiley & Sons, Inc., New York, 1998.

[60]   Ewins, D.J. "Modal Testing: Theory, Practice and Application". 2nd ed, Wiley: Hoboken, NJ, USA, 2009. ISBN: 978-0-863-80218-8

[61]   Armentani, E.; Caputo, F.; Esposito, L.; Giannella, V.; Citarella, R. "Multibody Simulation for the Vibration Analysis of a Turbocharged Diesel Engine". Appl. Sci. 2018, 8, 1192. http://dx.doi.org/10.3390/app8071192

[62]   Armentani, E.; Giannella, V.; Citarella, R.; Parente, A.; Pirelli, M. "Substructuring of a Petrol Engine: Dynamic Characterization and Experimental Validation". Appl. Sci. 2019, 9, 4969. http://dx.doi.org/10.3390/app9224969

[63]   Bianco, D.; Adamo, F.P.; Barbarino, M.; Vitiello, P.; Bartoccini, D.; Federico, L.; Citarella, R. "Integrated Aero–Vibroacoustics: The Design Verification Process of Vega-C Launcher". Appl. Sci. 2018, 8, 88. http://dx.doi.org/10.3390/app8010088

[64]   Azam, Sufyan A.; Fragoso, Alex. 2020. "Experimental and Numerical Simulation Study of the Vibration Properties of Thin Copper Films Bonded to FR4 Composite". Appl. Sci. 10, no. 15: 5197. https://doi.org/10.3390/app10155197

[65]   Maia, N.M.M.; Silva, J.M.M. "Theoretical and Experimental Modal Analysis". 1st ed, Wiley: Hoboken, NJ, USA, 1997. ISBN: 978-0-863-80208-9

[66]   Sze, S.M. "Physics of Semiconductor Devices". 3rd ed, John Wiley & Sons: Hoboken, NJ, USA, 2006. ISBN: 978-0-471-14323-9

[67]   Wenner, F. "A Method of Measuring Earth Resistivity". Bulletin of the Bureau of Standards 12, 469–478, 1915. Available online: https://nvlpubs.nist.gov/nistpubs/bulletin/12/nbsbulletinv12n4p469_A2b.pdf (accessed on 8 June 2020)

[68]   Valdes, L. B. "Resistivity Measurements on Germanium for Transistors," in Proceedings of the IRE, vol. 42, no. 2, 420-427, Feb. 195. https://doi.org/10.1109/JRPROC.1954.274680

[69]   Dieter, K. Schroder. "Semiconductor Material and Device Characterization", 3rd ed, Wiley-IEEE Press: Hoboken, NJ, USA, 2006, 2-35. ISBN: 978-0-471-73906-7

[70]   Van der Pauw, L. J. "A method of measuring specific resistivity and Hall effect of discs of arbitrary shape". Philips Res. Rept., 13, 1-9, 1958. https://doi.org/10.1142/9789814503464_0017

[71]   Van der Pauw, L. J. "A method of measuring the resistivity and Hall coefficient on lamellae of arbitrary shape". Philips Tech. Rev., 20,220-224, 1958. Available online: http://electron.mit.edu/~gsteele/vanderpauw/vanderpauw.pdf (accessed on 15 June 2020)

[72]   Ronald Chwang; Smith, B. J.; Crowell, C. R. "Contact size effects on the van der Pauw method for resistivity and Hall coefficient measurement". Solid-State Electronics, Vol. 17, Issue 12, 1974, 1217-1227. https://doi.org/10.1016/0038-1101(74)90001-X

[73]   Sun, Y.; Shi, J.; Meng, Q. "Measurement of sheet resistance of cross microareas using a modified van der Pauw method". Semiconductor Science and Technology, 1996. 11(5): p. 805-811. https://iopscience.iop.org/article/10.1088/0268-1242/11/5/025

[74]   Maluf, N.; Williams, K. "Introduction to Microelectromechanical Systems Engineering". 2nd ed, Artech House: Boston, US, 2004. ISBN: 978-1-580-53590-8

[75]   Partnership, P.F. "An Introduction to MEMS". 1st ed, Prime Faraday Partnership: Loughborough, UK, 2002. ISBN: 978-1-844-02007-2

[76]   Allen, J.J. "Micro Electro Mechanical System Design". CRC Press: Boca Raton, FL, US, 2005. ISBN: 978-0-8247-5824-0

[77]   Gardner, J.W.; Varadan, V. K.; Awadel karim, O. O. "Microsensors, MEMS, and Smart Devices". Wiley: Hoboken, NJ, USA, 2001. ISBN: 978-0-471-86109-6

[78]   Slocum, A.H. "Precision machine design: macromachine design philosophy and its applicability to the design of micromachines". Proceedings IEEE Micro Electro Mechanical Systems, Travemunde, Germany, 1992, p. 37-42, https://doi.org/10.1109/MEMSYS.1992.187687

[79]   Sandia National Laboratories, SUMMiT Technologies. Available online: https://www.sandia.gov/mesa/mems/ (accessed on 15 Nov 2017)

[80]   Maia, N.M.M.; Silva, J.M.M. "Theoretical and Experimental Modal Analysis", 1st ed, Wiley: Hoboken, NJ, USA, 1997, p. 217. ISBN: 978-0-863-80208-9

[81]   Guojun, H.; Yong, G.K.; Jing-en, L.; Chin, L.W.; Baraton, X. "Thermoelastic properties of printed circuit boards: Effect of copper trace". In Proceedings of the IEEE Proceedings 2009 European Microelectronics and Packaging Conference, Rimini, Italy, 15–18 June 2009; p. 1–6. Available online: https://ieeexplore.ieee.org/document/5272860 (accessed on 18 June 2020).

[82]   Hassan, M.K.; Abdellah, M.Y.; Mohamed, A.F.; ElAbiadi, T.; Azam, S.; Marzouk, W.W. "Fracture Toughness of Copper/Glass-Reinforced Epoxy Laminate Composites". Am. J. Mater. Eng. Technol. 2018, 6, p. 1–7. Available online: http://pubs.sciepub.com/materials/6/1/1/ (accessed on 15 June 2020).

[83]   Zare, H. G; Maleki, A.; Rahaghi, M. I.; Lashgari, M. "Vibration modelling and structural modification of combine harvester thresher using operational modal analysis and finite element method". Struct. Monit. Maint. 2019, 6, p. 33-46. https://doi.org/10.12989/smm.2019.6.1.033

[84]   Michael, D. Kelzenberg. "I-V Software (c)". 2015. Available online: http://www.kelzenberg.net/software/IV (accessed on 05 Aug 2019).

[85]   Negru, I.; Gillich, G. R.; Praisach, Z. I.; Tufoi, M.; Gillich, N. "Natural frequency changes due to damage in composite beams". J. Phys: Conf. Series 2015, p. 628. http://dx.doi.org/10.1088/1742-6596/628/1/012091

[86]   Available online: https://tinyurl.com/y6xttjwl (accessed on 15 July 2019).

[87]   Available online: https://tinyurl.com/yxbcfthk (accessed on 18 Aug 2020).

[88]   Smits, F.M. "Measurement of sheet resistivities with the four-point probe". Bell Syst. Techn. J. 1958, 37, 711–718. http://dx.doi.org/10.1002/j.1538-7305.1958.tb03883.x

[89]   M. Judelewicz, H.U. Künzi, N. Merk, B. Ilschner, "Microstructural development during fatigue of copper foils 20–100 ?m thick", Materials Science and Engineering: A, Vol 186, 1994, p. 135-142. https://doi.org/10.1016/0921-5093(94)90312-3

[90]   Shiraiwa, Takayuki; Enoki, Manabu. "Fatigue Crack Behavior of Thin Copper Sheet and Its Application for Smart Stress-memory Patch". Strength, Fracture and Complexity, vol. 7, no. 2, 2011, p. 205-214. https://doi.org/10.3233/SFC-2011-0139

[91]   Meng, B.; Fu, M. W. "Size effect on deformation behavior and ductile fracture in microforming of pure copper sheets considering free surface roughening", Materials & Design, Vol 83, 2015, P. 400-412. https://doi.org/10.1016/j.matdes.2015.06.067

[92]   Law, Kock-Yee; Zhao, Hong. "Surface Wetting Characterization, Contact Angle, and Fundamentals", Springer, 2015. ISBN: 978-3-319-25214-8

[93]   Asier Martinez-Urrutia; Peru Fernandez de Arroiabe; Miguel Ramirez;
        Manex Martinez-Agirre; M. Mounir Bou-Ali. "Contact angle measurement
        for LiBr aqueous solutions on different surface materials used in absorption
        systems", International Journal of Refrigeration, Vol 95, 2018, p. 182-188.
        https://doi.org/10.1016/j.ijrefrig.2018.05.041

[94]   Gadre; Kaustubh, S.; Alford, T. L. "Contact angle measurements for ad-
        hesion energy evaluation of silver and copper films on parylene-n and SiO2
        substrates", Journal of Applied Physics, Vol 93, 2002, p. 919-923. https:
        //doi.org/10.1063/1.1530362

UNIVERSITAT ROVIRA I VIRGILI
Electrical Properties and Surface Characterization of Thin Copper Films Subjected to Mechanical Vibrations
Sufyan Azam

UNIVERSITAT
ROVIRA i VIRGILI